CHAPTER I.

1 INTRODUCTION

1.1 Background

Soil compaction by heavy agricultural equipment is among the most important soil degradation agents on many farms around the world. The movement of heavy farm machinery and livestock progressively contributes to soil compaction on farms. Apart from soil compaction being caused by mechanically applied forces, drying and shrinkage can also cause it.

Wheel induced soil compaction arising from field traffic with heavy wagons, tankers and harvesting equipment is well documented by Tessier and Lague (1991). Schwab, Burmester and Raper (2002) reported that in conservation tillage systems, yields might not be sustainable due to ill effects of soil compaction. Therefore even in such systems, a deep tillage has to be used to ameliorate compacted soil profiles, even though the sub-soiling process may disturb some of the valuable surface residue, hence reducing the benefits of conservation tillage.

The following changes may take place in the soil mechanical properties as the soil becomes more compact:

- Increase in soil strength leading to a proportionate increase in its ability to resist penetration by both roots and tillage tools.
- Increase in bulk density leading to a reduction in pore sizes hence decreasing the hydraulic conductivity.

The intensity of these changes depends on the soil type. However, in all soil types the increase in strength not only translates into a considerable increase in energy input for tillage, but usually impedes the growth of plant roots, particularly at low moisture levels. Since for proper crop growth, the soil must have adequate void spaces to hold

enough water-air mixture, the reduction of soil pore sizes depraves crops of water and nutrients. However, McKyes (1989) reported an optimum compaction of sandy loam soil at a particular climate when the best corn yields were achieved. Thus there is a moisture level and density for a particular soil type at which crop yields can be maximized.

In an effort to rehabilitate compacted fields, the use of subsoilers to break and shatter subsoil layers has increased considerably in the recent past (Harrison, 1988). In most cases, the interest in deep tilling is directed towards increasing water infiltration rate, hence facilitating root growth. An increased water infiltration rate reduces run-off, which is one of the major causes of soil erosion and loss of moisture, normally resulting in reduction of crop yields, especially in areas subjected to severe droughts. In the early 1950s, research results indicated a significant cotton yield increase as a result of subsoiling (Smith and Williford, 1988). Alegre, Cassel and Bandy (1986) also attributed improved maize and soybean yields to sub-soiling. However for whatever the benefits might be, sub-soiling is a high-energy demanding operation and it needs to be carried out after thorough consideration of all available management options.

Due to increased traffic of heavy farm equipment on commercial farms in South Africa, incidences of soil compaction problems are becoming quite common on these farms. In an effort to avert the adverse effects of this problem on crop yields, some commercial farmers in South Africa are deep tilling once every few years with conventional subsoilers. In some maize producing areas, farmers are increasingly using two subsoilers in a tandem configuration, probably to overcome the problems of tilling below the critical depth for a single subsoiler. It is this increased use in a tandem configuration that has necessitated investigating how the implement interacts with the soil to facilitate better decisions and qualitative field operations.

According to Chi and Kushwaha (1990), a substantial amount of energy is used to manipulate soil during tillage and planting, accounting for almost fifty percent of the total energy consumed in crop production systems. Large amounts of energy are consumed because of the required high draft forces. These excessive draft forces result

in frictional and wear losses of the soil engaging tools. Draft forces are mainly influenced by physical and mechanical properties of soil, tillage tool geometry, operating depth and speed.

Harrison (1990) reported that draft forces for tillage implements, increase at a rate greater than a proportionate increase in tilling depth, thus limiting deep tilling because it becomes more difficult to recover the operating costs. This problem is aggravated by unstable prices of petroleum products on the international market, normally resulting in high-energy costs on the farm. It is therefore essential to design highly efficient tillage tools, which will require less energy to provide a satisfactory soil environment for both seed emergence and crop growth. The design of effective and efficient tillage tools starts with the analysis of soil failure, so that the forces and the energy requirements of the implements can be easily predicted. Therefore one of the major contributions towards achieving this vital goal is through accurate prediction of forces and specific draft of various tillage tools, coupled with a very clear understanding of the soil failure process.

1.2 Construction of subsoilers and mode of operation.

Subsoilers are operated at a greater depth than the other conventional tillage implements, to break up the hard subsoil layers which result from compaction by traffic of farm equipment and tillage operations at the same shallow depth each season. They therefore have heavy shanks that can be operated at depths ranging between 450 to 750 mm or deeper (Srivastava, Goering and Rohrbach, 1996).

As shown in figure 1.1, a typical subsoiler is made up of a shank and a foot with a share. The foot and the share do all the work of cutting the soil and lifting it over its entire width. According to McKyes (1985), the foot acts as though it was a flat blade extending all the way to the soil surface at an angle equal to its rake angle (α).

To improve the tillage effectiveness and efficiency of subsoilers, wings or blades are often added to the foot (Trousse and Humbert, 1959) thus increasing the critical depth.

At the same time, variations of the conventional subsoiler aimed at reducing their drawbar power requirements, have been developed over the years. Some of the interventions in subsoiler designs include straight or bent-legged, triplex and parabolic shaped shanks (Harrison, 1990).

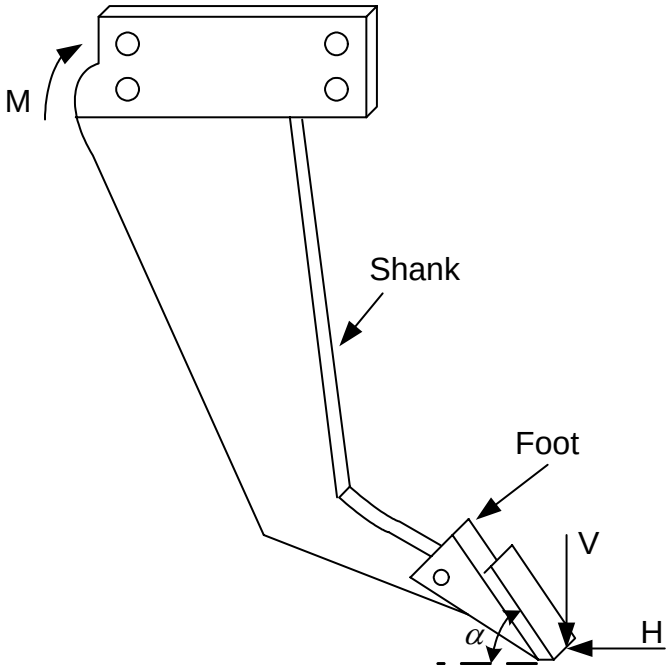

Figure 1.1. A Typical subsoiler and its force system.

In this study, straight shanks with narrow blades, but without wings were used. In most cases, straight shanks are angled with a slight rearward incline to reduce draft forces. Soil disturbance from straight shanks is symmetric with equal amounts of soil being disturbed on either side of the shank. The force system in such a tillage process, where soil failure is symmetrical, consists of two mutually perpendicular force components, a horizontal (H) and a vertical (V) force, and a moment (M) in the plane of these two forces. The lateral forces and lateral moments are zero in this kind of symmetrical soil failure.

CHAPTER II

2 LITERATURE REVIEW.

2.1 Soil compaction.

Soil compaction refers to the increase in density of a soil as a result of applied loads or pressure. The soil density increase is a function of both compactive effort and the soil water content. According to Baver, Walter and Wilford (1972), the force required to compact a soil to a given density decreases exponentially with the soil water content. Further more, soil compaction is also influenced by the size of the soil particles and the organic matter content. Soil types characterized by smaller particles are more susceptible to compaction. In addition, the following parameters also influence the ability of the soil to withstand mechanical loading:

- The grain size distribution.
- The amount of clay minerals.
- The structure and its strength.
- The bulk density, pore size distribution and continuity.

If wheel-induced soil stresses exceed soil strength, and the soil condition is such that the soil becomes stronger by compaction, soil will deform and compact until a new state of soil strength has been reached which is able to counteract the wheel-induced stress field (Koolen, Lerink, Kurstjens, Van de Akker and Arts, 1992). According to Hartge (1988), the least possible compaction within a whole soil profile can be assumed to be the one that is in equilibrium with the weight of the soil overlying it. This means that compaction and thus bulk density must increase with increasing depth below the soil surface. It follows therefore that even in virgin soils a compaction state prevails in subsoil layers. It will therefore be preferable to measure soil characteristics as influenced by depth and apply the values when testing the proposed force model.

Larson and Gupta (1980) measured changes of the pore water-pressures during soil compression. They observed that the point of minimum pore water-pressure corresponds to the maximum stress that can be applied without serious damage to the aggregate structure of the soil.

Reduced root development due to soil compaction, can affect the efficiency of the use of water and nutrients, thus forcing farmers to use more irrigation water and fertilizers. This may enhance negative environmental impacts of agriculture.

The stress-strain relationship in soil compaction was reported by Stafford (1981) to be time-dependant. Horn and Hartge (1990) demonstrated that soil strength resulting from compaction due to a given load, was dependant on the duration of loading. This means that since tractors and other harvesting machinery move relatively fast, soil compaction is worsened by their repeated re-compaction year after year and also the ploughing with mouldboard ploughs at the same depth each season, applying a load to the same soil at the furrow bottom, thus extending the period the load is applied. The plough bottoms also have a smearing effect on the soil at the ploughing depth.

The most effective way to reduce soil compaction is to reduce the compactive forces or load and control soil water content at the time of loading. Farmers do have flexibility to reduce axle loads but not controlling the soil water content at the time of field operations, as they are forced to plough and plant direct after the rains to complete planting before it gets too dry.

Controlled traffic, a concept in which wheel traffic is restricted to permanent traffic lanes, is therefore considered to be a viable management system. Since there is close relationship between tillage and traffic systems, practicing no-till cropping regime can reduce or reverse the effects of soil compaction induced by farm machinery.

In cropping systems, where advanced mechanization forms a significant part of the production technique, the following approaches are being practiced in an attempt to reduce soil compaction effects:

- Reduction in ground contact pressure by the use of wider tires, dual, triple or cage wheels (Dickson, Campell and Henshall, 1983).
- Reduction in the number of passes and combined implements such as a cultivator-drill combination.
- Use of lightweight materials such as aluminum or plastic, in the construction of some farm equipment (Dann, 1983).
- Use of new technology, e.g., low-volume spraying and stripper-header for the harvesting of cereals (Price, 1989).

The first two techniques are applied in the maize growing regions with fine sandy soils. Also the no-till cropping system, as well as stubble mulch tillage is used with positive results.

Johnson, Voorhees, Nelson and Randall (1990) observed no soybean yield reduction due to surface and subsurface compaction while maize yields were consistently reduced. This was in agreement with Tardieu (1988) who had earlier reported that different crops and even different varieties show different sensitivity to soil compaction. Cowpea, for example, is capable of rooting well at a level of compactness that inhibits more sensitive crops like maize. He therefore concluded that crop rotation could alleviate moderate levels of soil compaction.

Crop rotation is applied at a limited scale and in maize growing regions. Alternative mechanical ways to combat compaction will be necessary probably by sub-soiling.

Voorhees (1983) studied the relative effectiveness of tillage, freezing and thawing in ameliorating a compacted soil. He found that sub-soiling with a chisel plough or a conventional subsoiler to be more effective in reducing the bulk density of the wheel-tracked soil than natural methods. Sub-soiling even for higher clay contents, will thus be advantageous, although not to the same extent as for fine sandy soils. The only land available within reach, traveling with the large tractor and tillage dynamometer, is a loam clay soil. It was therefore decided to test the model on this soil type.

It is clear from the above literature that maize is very sensitive to soil compaction. Related problems are therefore expected in areas where it is grown in fine-grained soils, such as the sandy soils in the Free State of South Africa. Leaching of clay particles is also experienced on the fine sands, which results in a layer of restricted permeability lower in the profile. Thus, some farmers practice sub-soiling with subsoilers in tandem to break up this impermeable layer and also combat soil compaction.

Although maximum soil break up is achieved when soils are very dry with minimum damage by the sub-soiling tractor, energy consumption is too high. The larger clods must also be pulverised in the follow up tillage operation. This forces farmers to subsoil when the soil water content is closer to field capacity, even though the break up is not as effective as in drier conditions.

In order to have the soil water content during tests within reasonable limits, it was decided to irrigate the fields during winter (dry season) and collect data after a few days as the soil dried. More data will be generated than necessary, but only specific data within specified limits can be used to test the model.

.

2.2 Theory of soil-failure in passive tillage.

Implements used in passive tillage for the formation of soil tilth, act by loading the soil until cleavage patterns develop. As soon as a force is applied to the tillage implement, the stress in the soil increases in a zone extending forward from the surface of the soil-engaging element (O'Callaghan and Farrelly, 1964). When a critical intensity of stress is reached, rupture forms in the soil due to failure. This is in agreement with Coulomb's failure theory, which states that failure in a material occurs when the maximum shear stress on any plane reaches some critical value equal to the shear strength of that particular material. (Gere and Timoshenko, 1999). Further more at failure, agricultural soils obey the Mohr-Coulomb failure criterion. This criterion states that the shear strength of soil increases linearly with increasing normal stress and it fails when the Mohr circle touches an envelope described by:

$$\tau_s = c_c + \sigma_n \tan\phi \quad \text{.....2.1.}$$

Where:

τ_s = Maximum soil shear stress at failure (kPa).

c_c = Soil cohesion coefficient (kPa).

σ_n = Normal stress exerted on the rupture plane (kPa).

ϕ = Internal soil friction angle (degrees).

When the soil fails, the shape of the developed rupture plane is influenced by the geometry of the tillage tool and the soil shear strength parameters. (Chi and Kushwaha, 1990). The force required to form the initial rupture within the soil normally approximates the average draft force requirement of a tool.

From equation 2.1, it is clear that Coulomb noted two mechanical processes which determine the soil shear strength namely cohesion and friction. The soil cohesive parameter of the shear resistance is due to direct rupture of two parts of soil body and therefore it depends upon the strength of the in situ bonds. Hence it is constant regardless of the normal pressure acting on the soil body. On the other hand, the shear strength associated with friction, results from the sliding of soil over soil and it is therefore proportional to the normal stress exerted on the rupture plane.

During tillage, soil failure does not only occur in a shear mode along an internal rupture plane in the soil but also at the boundary between the soil and the tool. At the boundary between soil and another material such as steel or teflon, the shear strength is normally less than the internal soil strength. This is due to the fact that the value of interface adhesion is usually less than the soil cohesion since the degree of interface roughness ranges between zero and the value of the internal soil friction angle. This therefore necessitates the use of other parameters in equation 1 thus this equation is transformed into:

$$\tau_t = c_a + \sigma_n \tan\delta \quad \text{.....2.2.}$$

Where:

τ_t = Maximum frictional stress at soil-tool interface (kPa).

c_a = Adhesion coefficient (kPa).

δ = Interface friction angle (degrees).

While equation 2.1 describes the stresses interacting on a failure plane within the soil body, equation 2.2 describes the stresses interacting on a soil-tool interface. However, these two failure criteria are static since they do not account for the effects of travel speed. Many researchers therefore studied the properties of soil strength further.

Glancey and Upadhyaya (1996) reported that the soil shear strength consists of static as well as a dynamic component. This observation was based on the fact that soil shear strength was found to be strain rate dependent. With this approach, a general expression for maximum soil shear stress at failure under the influence of a tillage tool was represented by:

$$\tau_s = \tau_0 + \tau_1 v \quad \text{.....2.3.}$$

Where:

τ_s = Maximum soil shear stress at failure (kPa).

τ_0 = Soil property related to the static component of shear strength (kPa).

τ_1 = Soil property related to the dynamic component, proportional to operating speed (kPas m^{-1}).

v = Operating speed (ms^{-1}).

After studying tillage tool draft force requirements, Stafford (1979) observed that draft force under dynamic conditions, also consists of a static draft force component as well as a dynamic one. He proposed the draft force as:

$$F_d = F_s + f(v) \quad \text{.....2.4.}$$

Where:

F_d = Draft force under dynamic conditions (N).

F_s = Static draft force component (N).

f(v) = Function containing a soil inertial term (N).

Stafford (1979) and Flenniken, Hefner and Weber (1977) independently concluded that the effects of strain rate on shear strength accounted for most of the increase in draft force of a tillage tool with speed. Further more, the tool operating characteristics, soil properties and tool geometry are known to influence the draft force requirements of a tillage tool.

In Stafford's comprehensive study of the rigid tine performance, two different modes of soil failure were identified: rigid-brittle which occurs at a soil water content below the plastic limit and flow failure occurring when it is above the plastic limit. Earlier Elijah and Weber (1971), after observing the soil failure patterns, identified four distinct types of failure: shear-plane, flow, bending and tensile. They noted two parameters affecting these failure types as blade travel speed and rake angle, even though their effects were never quantified. At the same time, Olson (1984) reported that the nature of soil failure caused by narrow tines changed from the period of creation of the shear planes to continuous flow as tool travel speed increased.

Dransfield, Willat and Willis (1992) studied the effect of cultivation speed on soil flow patterns. Their results indicated that when a soil-cutting blade moves at a relatively high velocity, the cut soil slices are thrown sideways without falling back into the created furrow. Since deep tilling implements are normally operated at low speeds, due to their high draft force requirement at high speeds, the cut soil slices by subsoilers are bound to fall back into the opened furrow. In case of subsoilers in tandem therefore, the soil slices cut by the front subsoiler are likely to surcharge the soil to be disturbed by the rear deeper working subsoiler, especially at a wider longitudinal spacing.

Stafford (1981) studied the effect of rake angles on types of soil failure. The reported results indicated that in loose soils, between 45^0 and 90^0 rake-angle tines caused brittle

failure. This indicates that rakes angles for subsoilers in tandem, should be equal to ensure the same type of soil failure caused by each subsoiler.

2.2.1 Effects of tillage tool-operating width.

When the tillage tool is considerably wider than it is deep (a ratio of about ten to one), the behavior of the soil-failure is two-dimensional (McKyes, 1989). The slope of the soil-rupture plane at the bottom of the tool is governed by the interface and soil internal friction angles. However, the mode of soil-failure by a narrow tillage tool is a three-dimensional process consisting of a soil-zone failing in front of the tool as well as at its sides. O'Callaghan and Farrelly (1964) reported a change in soil-failure as the working depth/tool-width ratio was increased and postulated a critical depth which separated the distinct soil-failure modes. The critical depth is identified by the following two failure mechanisms:

- An upper soil failure zone, corresponding to the depth less than the critical depth, where the displaced soil has forward, sideways and upward components termed the crescent failure.

- A lower failure zone, corresponding to the depth below the critical depth, where displaced soil has components both in the direction of travel and sideways termed the lateral or transverse failure.

Spoor and Godwin (1978) studied the performance of conventional tined subsoilers with and without different types of wings, in terms of draft force and soil area disturbance. The addition of wings increased the total soil disturbance area, draft force requirements and useful working depth. While the draft force requirement increased by 30%, the disturbed soil area is doubled, leading to a significant improvement in tillage effectiveness and efficiency.

The ratio of the tool-width to its working depth was found to influence the location of critical depth. At the same time, the position of the critical depth influences the

maximum useful working depth of a tine. The practical disadvantage of working below the critical depth is that the draft force increases while soil disturbance is often reduced and soil compaction occurs. In the same study, it was reported that for effective soil loosening, crescent failure should occur. Furthermore, for a shallow working depth (i.e. above the critical depth), soil failure pattern was similar for different tine shapes but differ at a greater depth below the critical depth. This soil failure pattern was found repeatedly over a wide range of soil water content and density values, as well as soil classes.

2.3 Power requirements for soil engaging tools.

It has always been the aspiration of agricultural engineers to develop high performance tillage tools with low energy requirements. Van den Berg (1968) reported that the performance of a tillage tool is measured in terms of draft force per unit-cut area or input energy per unit-disturbed volume. Furthermore, he noted that it is dependant on three factors i.e., the initial soil condition, shape and manner of tool movement. A number of researchers therefore have investigated the power/energy requirements of different designs of subsoilers.

Garner and Wolf (1981) measured the power requirement during sub-soiling coastal plain soils. They measured draft force, tractor wheel slip, fuel consumption, engine and travel speeds. They reported that the draft force values were in agreement with the lower portion of those published in the ASAE standard (ASAE, 1990). The draft force per unit cut-area, wheel slip and fuel consumption increased with increasing operating depth. In their earlier research, they concluded that draft force per unit cut-area increased linearly with an increase in depth.

In an effort to reduce sub-soiling power requirements, Araya (1985) injected a fluid from the tip of a subsoiler to loosen the soil structure in front of the tool and also lubricate the tool-soil interface. After taking into account of the power required for injecting the fluid, a total saving in energy per unit volume of 30% was recorded. Smith and Williford (1988) evaluated the power requirements of conventional, triplex and parabolic subsoilers. Their results indicated a parabolic subsoiler to require at least 10 to

16% less draft force per unit area tilled than a conventional or triplex subsoiler. The triplex draft force requirement was slightly higher than for the conventional subsoiler. They therefore concluded that the shape of tines for subsoilers has a significant influence on the power requirements of the implement. To ensure uniform influence of both subsoilers on power requirements during the field experiments, subsoilers of the same shape were used.

Owen (1988) studied the relationship of travel speed to draft forces and soil disturbance during sub-soiling. He reported a significant correlation between draft force and the square of travel speed. This was in agreement with Gill and Van den Berg (1967). At the same time, he reported no significant correlation between travel speed and soil disturbance.

Dransfield (1964) using rake angles ranging between 60^0 and 90^0, reported that the vertical and horizontal force components decreased and increased respectively with an increase in rake angle. This was in agreement with earlier research by Payne (1959).

Kushwaha and Zhang (1998) observed that since the tillage process is dynamic, soil-tool response i.e. draft force, tool wear and final soil condition, is dependant on speed and time. Earlier Goryachkin (1929) had expressed the plough draft force as a function of its operating speed. However since his expression includes a speed effect coefficient that has to be determined from tests, it could not be readily used to predict the draft force. Sohne (1956) assumed that the soil failure profile was a wedge and proposed an equation to determine the component of the inertial force for the soil failure wedge. This equation was adopted in the proposed mathematical model to account for the acceleration effects.

2.4 Development of soil-failure profile models.

A number of researchers have employed an analytical approach based on limit equilibrium analysis, to develop soil failure models, which have significantly contributed to the understanding of soil-tool interaction.

In the recent past, models based on the numerical approach employing the finite element method (FEM), have been developed. These models based on FEM have generated a substantial amount of knowledge towards the understanding of the soil cutting process by various tillage tools. Both these approaches are considered below.

2.4.1 Analytical approach.

There is a considerable amount of literature on the subject of soil failure under the action of simple tillage tools. Many researchers have developed models based on limit equilibrium analysis as an analytical approach to describe soil failure and also evaluate the performance of various tillage tools in terms of soil forces and areas tilled. These models were derived from Terzaghi's (1943) passive earth pressure theory with the assumption of a preliminary soil failure pattern. In this theory, a two-dimensional soil-failure zone was assumed to exist ahead of a wide soil-cutting blade. This zone consisted of a Rankine passive zone and a complex shear zone bounded by part of a logarithmic spiral curve. The resulting soil-force on the blade was calculated by assuming static equilibrium along the boundary

Payne (1956) adapted the Coulomb theory of soil failure to conduct research studies that described the soil forces. The comprehensive results reported from his studies were improved on by Osman (1964) who, by means of dimensional analysis, introduced such factors as soil properties, rake angle and tool-surface roughness in Payne's force expression.

Reece (1965) employed both Terzaghi's (1943) logarithmic spiral method and Osman's soil force expression to develop a mathematical soil force model popularly known as Reece's earthmoving equation. This model included gravitation, cohesion, adhesion and surcharge components of the soil reaction per unit width of the interface. However, this model neglected the effects of inertia forces therefore it only applied to all forms of soil failure at very low speeds and holds good for interfaces inclined to the vertical. By applying the theory of plasticity, Hettiaratchi and Reece (1974) transformed Reece's earthmoving equation into a three-dimensional soil failure model.

O'Callaghan and Farrelly (1964) proposed a model that included a critical depth. They reported that soil-failure in the upper failure zone above the critical depth, could be adequately described by the two-dimensional logarithmic spiral method. The lower portion has failure surfaces described by Prandtl's rupture analysis. The effects of the side crescent wings in the upper portion plus those due to soil adhesion and interface friction are not included in this model. It therefore tends to under predict the tool draft force requirements (Grisso and Perumpral, 1985). Godwin and Spoor (1977) proposed a soil failure model with which the location of the critical depth can be determined. They further showed that the total draft force required to move an implement operating deeper than its critical depth, is a summation of the draft force required to fail soil above the critical depth with that required to fail soil below the critical depth.

The method used by the above models to determine the total force on a tillage tool is rather complicated. It was simplified though by McKyes and Ali (1977). Their model modified the soil failure ahead of a tool into a center failure wedge and two circular side crescents, and a plane failure surface at the bottom of the failed soil wedge that made it easier to solve the limit equilibrium equations. In this model they incorporated an integration method, which evaluated the total force required to fail the side crescents as developed by Godwin (1974). To simplify the integration process, the failure boundary on the surface is assumed to be circular.

In the 1980s and 1990s, investigators such as Perumpral, Grisso and Desai (1983) continued to conduct very important research studies, which significantly contributed towards better understanding of soil-tool interface mechanics. However, the proposed models were simplifying the soil failure ahead of a tool by assuming that the forward travel speed was sufficiently small that its effects could be neglected or that the draft force does not vary with operating speed. A number of researchers were reporting soil strength to be a function of deformation rate. For example Gill and Van den Berg (1967) had reported that the draft force requirement of a moldboard plough increases approximately with the square of travel speed. This can be explained by the fact that as the tool speed is increased, higher confining pressures are required to cause shear due to increased soil shear strength. At the same time, the present trend is towards using wider

tillage tools and/or increasing operating speeds so that a larger area is tilled. This necessitated the development of dynamic soil failure models.

Based on Hettiarratchi and Reece's static models, Stafford (1979, 1984) proposed dynamic models for both two and three-dimensional soil failure cases by introducing acceleration effects into these models. Following Perumpral's earlier research, Swick and Perumpral (1988) proposed a three-dimensional dynamic soil failure model. The proposed soil failure zone is similar to the McKyes-Ali (1977) static model and the force equation is derived in the same way except an acceleration force is included to account for the travel speed effect. They also modified the equation for determining the maximum width of the side circular wedge. Since this model accounts for acceleration force effects, it adequately predicted the forces encountered by a narrow tine. However it was found to over predict the soil-failure rapture radius. This was attributed to replacing the actual curved soil-failure plain with a straight one.

Zeng and Yao (1990, 1997) also developed a dynamic soil-cutting model. This one was obtained from the relation between soil shear strength and shear strain rate, and the relation between soil-metal friction and sliding speed. To be able to determine the position of the shear failure boundary, this model requires prior knowledge of the failure shear strain.

2.4.2 Numerical approach.

The numerical methods, especially the finite element method (FEM) have been used to analyze the soil cutting process by various tillage tools. Since FEM adopts matrix plus the similarity of elements used, made it quite convenient for computer programming. At the same time, the continuous increase of computer speed and memory during the recent years has enabled FEM to become a powerful tool for the numerical solution of a wide range of engineering problems. Some researchers have therefore made use of this tool to study the behavior of various tillage implements in soil. These researchers include Chi and Kushwaha (1990, 1998) and Kushwaha and Shen (1998) among others.

Unlike the limit equilibrium procedure, FEM is used without a preliminary assumption of soil failure pattern and it is flexible in simulating the tillage operation with different tool shapes. The proposed soil-cutting models based on FEM, provide a progressive failure zone. They can also calculate displacement, velocity, acceleration and stress distribution on the tool surface. Therefore finite element analysis of the tillage process overcomes some of the shortcomings in analytical analysis.

2.5 Conclusions from the reviewed literature.

Soil shear strength and draft force requirements of a tillage tool are functions of soil deformation rate. It follows therefore that during the execution of the field tests, operating speed had to be kept constant so that a uniform speed influence on the collected data is maintained.
Soil water content has been reported to be an influential factor of the soil characteristics and draft force requirements of the tillage tools thus influencing the size of the soil cross-section area tilled. At the same time, it affects the soil-failure type. It was therefore aimed at maintaining a minimal variation in soil water content during the field tests.

The rake angle, geometry of the tool and operating speed have been proven to influence both the soil-failure types and rupture planes. To have the same type of soil-failure and rupture planes, the rake angles and the geometry of the blades for the front and rear subsoilers were the same.

The reviewed literature has shown that the draft force requirements of a tillage tool increased when operated below its critical depth. It was therefore hypothesized that when the two subsoilers are operated above their critical depth, energy utilization would be optimized. This was achieved by operating the front subsoiler above its critical depth. In combination of the two subsoilers, the critical depth of the rear subsoiler was not reached.

The soil rupture angle β could be determined by either McKyes-Ali (1977) model or Ji Zhang-Kushwaha (1995) model. Both of these models are based on the general earth pressure model proposed by Reece (1965). While the McKyes-Ali model is based on minimizing only the gravitational term of the earth pressure model, Ji Zhang-Kushwaha derived their model by minimizing all the parameters. McKyes-Ali model was chosen since it was considered to be simpler to use as only one parameter had to be minimized. Further more, there was no major difference between the results reported by Ji Zhang and Kushwaha (1995), and McKyes-Ali's model.

For predicting the force requirements of the front subsoiler, the model proposed by Swick and Perumpral (1988) was used. This choice was based on the fact that it is a three-dimensional model and capable of accounting for the acceleration effects. It was reported to have adequately predicted the forces encountered by a narrow tine.

This model divides the soil-failed wedge into a center and a side circular wedge on each side of the tillage tool.

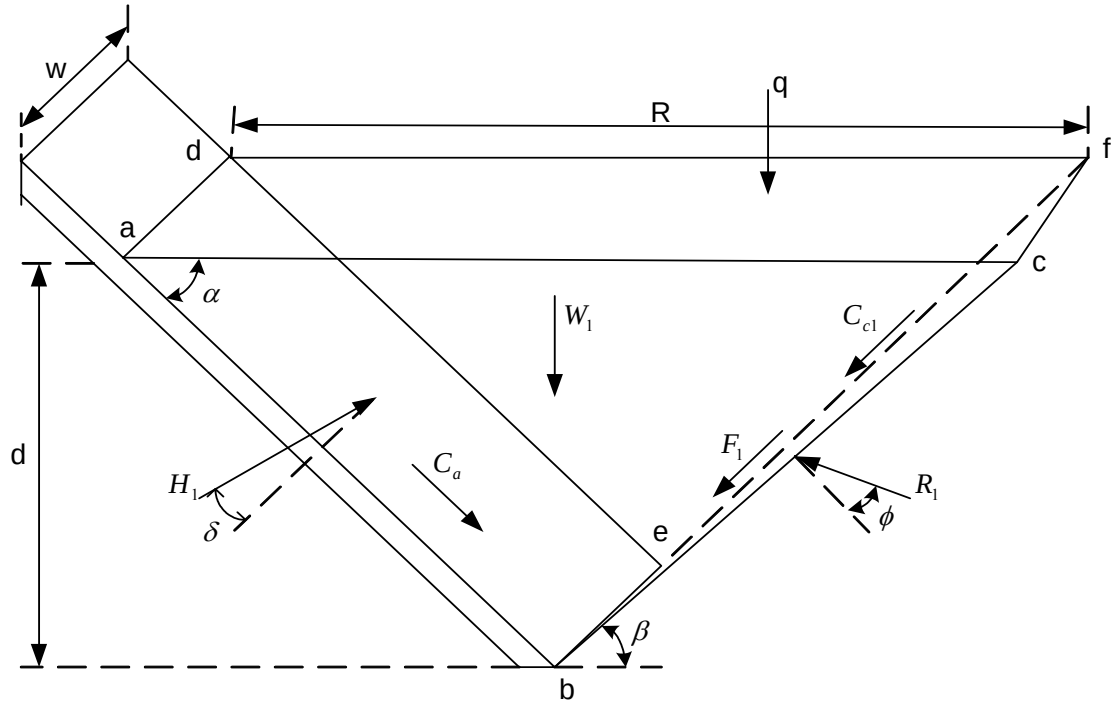

Figure 2.1: The idealized failed center wedge.

Where:

W_1 = Weight of soil in the center wedge (N).

C_a = Adhesion force (N).

C_{c1}= Cohesion force at the rupture plane of the center wedge (N).

F_1 = Acceleration force (N).

R_1 = Reaction force at the rupture plane (N).

R = Rupture radius (m).

q = Surcharge pressure (N/m^2).

α = Rake angle (degrees).

δ = Interface friction angle (degrees).

β = Angle between the rupture plane and the horizontal soil surface (degrees).

ϕ = Soil internal friction angle (degrees)

The draft force to fail the center portion of the failure wedge (figure 2.1) was designated as H_1 and it was expressed as follows:

$$H_1 = \left[(W_1 + Q_1)\sin(\phi + \beta) - C_a \cos(\alpha + \phi + \beta) + (C_1 + F_1)\cos(\phi)\right] / \left[\sin(\alpha + \phi + \beta + \delta)\right] \quad \text{.....2.5.}$$

Where:

Q_1 = Surcharge force acting on the center wedge (N).

The vertical force due to the center portion of the failure wedge was designated as V_1 and it was expressed as follows:

$$V_1 = \{Q_1 + W_1 + (C_1 + F_1)[\sin\beta + \cot(\beta+\phi)\cos\beta] - C_a[\sin\alpha + \cot(\beta+\phi)\cos\alpha]\} / [1 + \cot(\beta+\phi)\tan(\alpha+\delta)] \quad \text{.....2.6.}$$

Based on figure 2.2, the draft force to fail the side circular wedge was designated as H_2 and it is the integral of the horizontal component of dh_2. It was expressed as follows:

$$H_2 = \left[(W_2 + Q_2)\sin(\beta+\phi)\sin\theta + F_2\cos\phi(\theta/2 + \sin(2\theta/4) + C_2\cos\phi\sin\theta\right]/$$
$$\left[\sin(\alpha+\phi+\beta+\delta\right] \quad \text{.....2.7.}$$

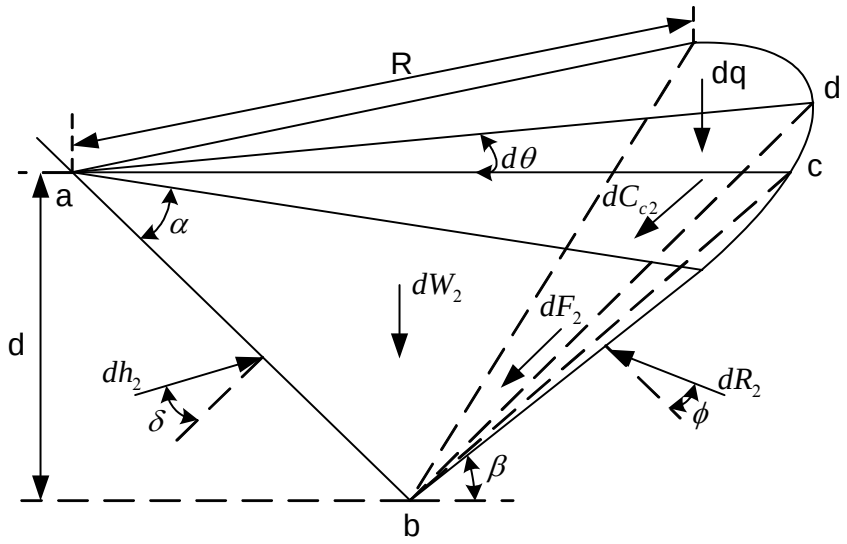

Figure 2.2: The idealized failed side-circular wedge.

The vertical force due to the side circular wedge was designated as V_2 and it was obtained by integrating of the vertical component of dh_2. It was expressed as follows:

$V_2=\{Q_2+W_2+(C_2+F_2)[\sin\beta+\cot(\beta+\phi)\cos\beta]\}/[1+\cot(\beta+\phi)\tan(\alpha+\delta)]$……...2.7.

Where:

C_{c2} = Cohesion force at the rupture plane of the side circular wedge (N).

F_2 = Acceleration force (N).

Q_2 = Surcharge acting on the side circular wedge (N).

W_2 = Weight of soil in the side circular wedge (N).

ϕ = Internal soil-failure angle (degrees).

The total draft force to fail the center and the two side circular wedges was expressed as:

$H = H_1 + 2H_2$ ……..……2.8.

The vertical force due to the center and the two side circular wedges was expressed as:

$V = V_1 + 2V_2$ ……2.9.

2.6 Justification for conducting this study.

An extensive literature survey conducted has revealed that even though a lot of knowledge has been generated on the subject of soil interaction with simple inclined tools, no such exhaustive knowledge concerning subsoilers in a tandem configuration has been found. No single report has been found addressing a mathematical model for predicting the maximum cross-section area disturbed or force requirements of subsoilers in tandem.

Bearing in mind that for whatever benefits might be, sub-soiling is a high energy demanding operation, no literature was found indicating the location of the front subsoiler relative to the rear subsoiler at which energy utilization is optimum. These grey areas call for more comprehensive investigation of how two subsoilers in tandem interact with the soil.

2.7 Hypotheses.

The reviewed literature has led to the following hypotheses:

- ***The existing analytical mathematical models for a single tine, can predict both the vertical and horizontal force components acting on the front subsoiler in a tandem configuration as well as the tilled cross-section area.***

- ***Based on the existing analytical models, a model to predict the force components acting on the rear subsoiler, as well as the maximum tilled cross-section, can be derived from the basic principles.***

- ***The front subsoiler, for two subsoilers in tandem, has both an optimum depth and longitudinal spacing relative to the position of the rear deeper working subsoiler, at which energy utilization is optimized.***

2.8 Objectives.

In order to verify the above hypotheses, the following are the specific objectives of this study:

- ***To ascertain if any of the existing mathematical models for a single tine adequately predicts vertical and draft force requirements for the front subsoiler in a tandem configuration.***

- ***To develop a mathematical model that predicts the vertical and draft force requirements of the rear subsoiler and tilled profile section at a typical spacing.***

- ***To establish the relative position of the front subsoiler under which energy utilization is optimized.***

2.9 Chosen procedure and justification.

Limit equilibrium analysis is the chosen procedure as opposed to a numerical approach employing the finite element method (FEM). This choice is based on the fact that the constitutive relationship of a material is a prerequisite for the use of FEM, (Bathe, 1996). This relationship is not fully understood for agricultural soils (Shen and Kushwaha, 1998). Zhang and Kushwaha (1998) therefore concluded that a widely accepted constitutive relation for agricultural soils is not yet available.

In most cases, agricultural soils are unsaturated, exhibiting an unsteady and more complex behaviour than saturated soils. Further more, the existing soil constitutive relationship-models are more geared towards geotechnical engineering applications, hence they pay little or no attention to soil response after its failure. For Agricultural Engineers, soil failure is the primary objective of any tillage process.

CHAPTER III

3 DEVELOPMENT OF THE MATHEMATICAL FORCE MODEL FOR THE REAR SUBSOILER.

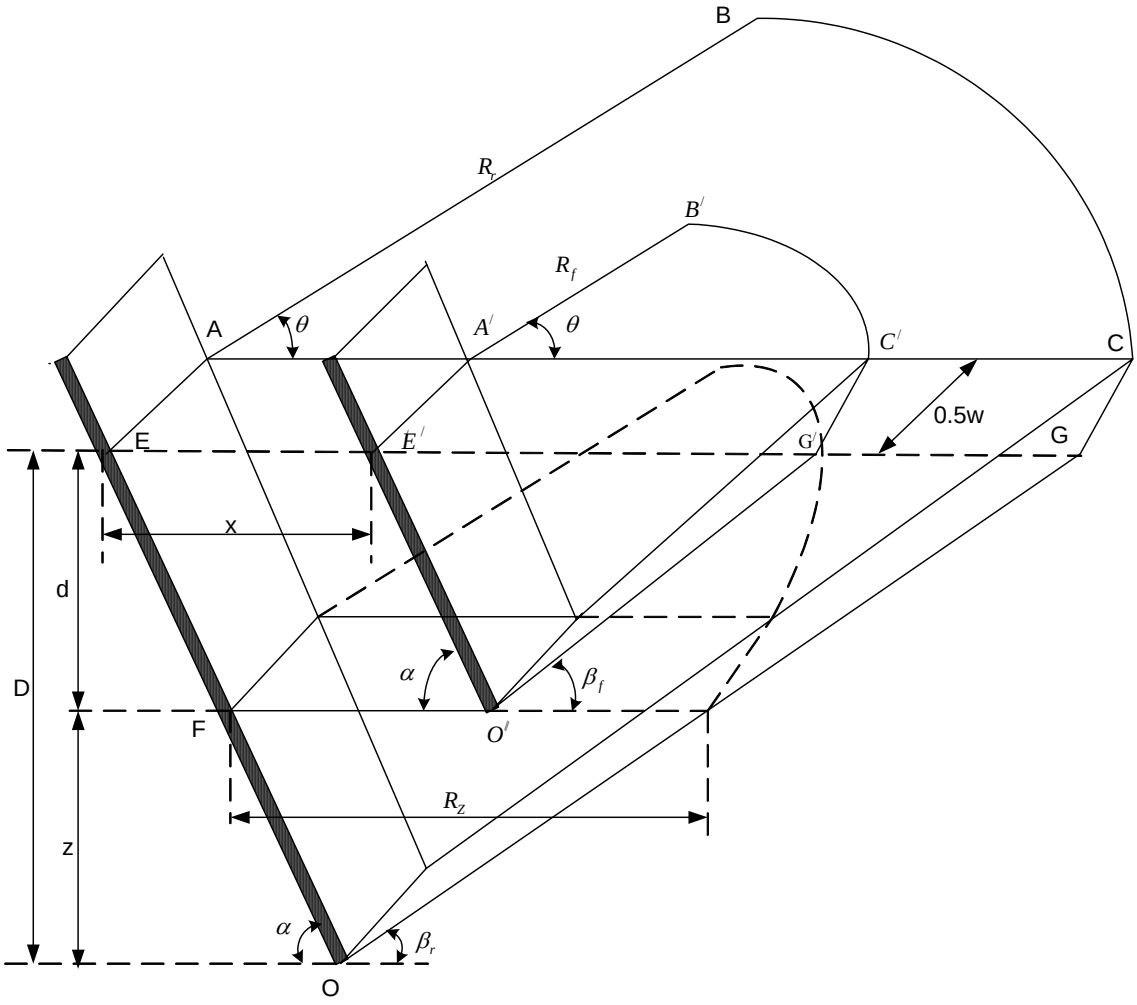

Figure 3.1: Three-dimensional half section of a soil-wedge failed by two subsoilers in tandem.

Where:

x – The projected spacing between the two subsoilers (m).

d - The operating depth of the front subsoiler (m).

D - The operating depth of the rear subsoiler (m).

R_f - The rupture radius of the front subsoiler (m).

R_r - The rupture radius of the rear subsoiler (m).

R_z - The rupture radius of the rear subsoiler at depth, d (m).

w – The tool width (m) = 0.08 m.

z - The effective operating depth of the rear subsoiler in undisturbed soil (m).

α - The rake angle (degrees) = 37^0.

β_f - the angle between the rupture plane of the front subsoiler and the horizontal soil surface (degrees).

β_r - the angle between the rupture plane of the rear subsoiler and the horizontal soil surface (degrees).

θ - Horizontal included angle of the failed circular side-wedge (degrees).

Appendix A presents the procedure followed to determine β_f and β_r for the centre failure wedge. Based on the soil characteristics at the experimental site, their difference ranged between 2^0 and 5^0 for the subsoiler spacing considered in this study. A difference of 5^0 in β, translated into a 3% difference of the predicted draft force. This difference was regarded as negligible and therefore the two angles were assumed to be equal so that equations for calculating the forces acting on the subsoilers could be simplified. Thus $\beta_f = \beta_r = \beta$.

This soil failure-wedge (fig. 3.1) is made up of two distinctive sub-wedges. Namely, the soil failure wedge in front of each tool, called the center soil-failure wedge and the circular soil failure-wedge at each side of the two subsoilers.

3.1 Center soil-failure wedge.

From the geometry of the center soil failure-wedge in figure 3.1.1, the rupture radii are determined as follows:

$$R_r = D (\cot \alpha + \cot \beta).$$

$$R_f = d (\cot \alpha + \cot \beta).$$

$$R_z = z (\cot \alpha + \cot \beta).$$

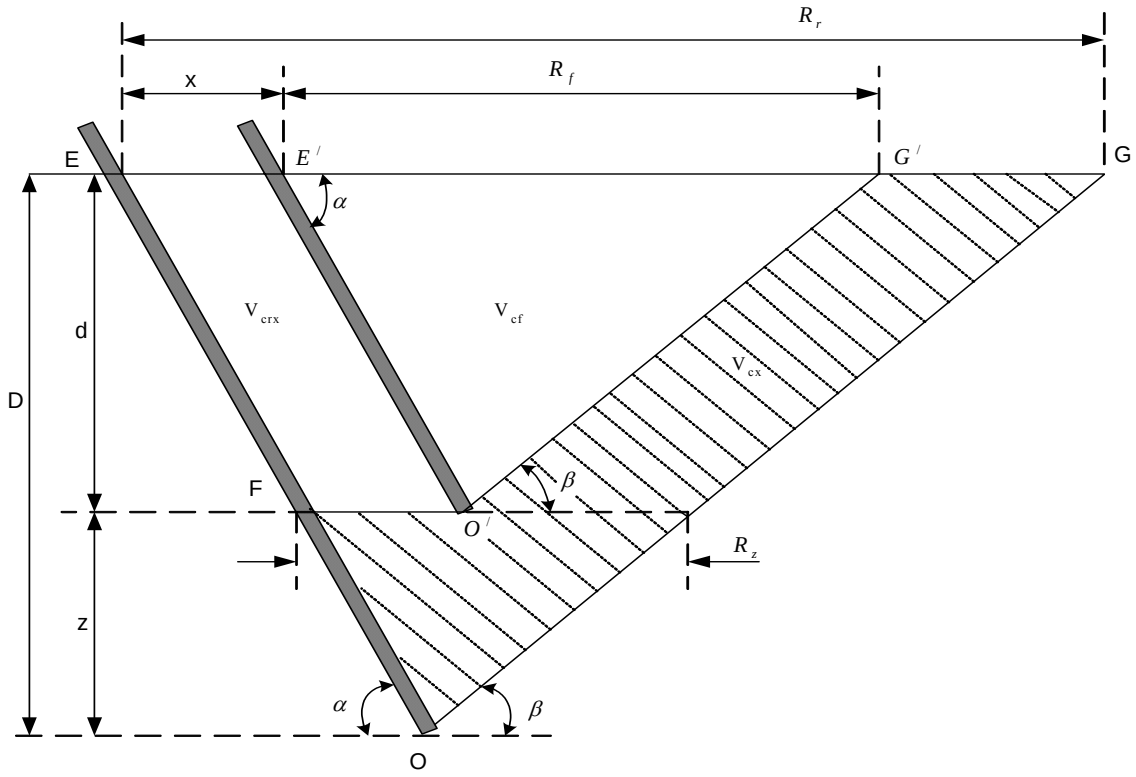

Figure 3.1.1: The center soil-failure wedge.

3.1.1 Soil volume disturbed by the rear subsoiler.

To be able to calculate the load on the shear and frictional surfaces, soil volumes tilled have to be determined. The soil volume (V_{cx}) disturbed, in the center-failure wedge by the rear subsoiler and the total soil volume (V_{ct}) disturbed by both subsoilers, vary with subsoiler spacing (x) as follows:

i). *The spacing, x ranges between 0 and R_z ($0 <= x < R_z$).*

From figure 3.1.1:

$V_{cx} = V_{cr} - (V_{cf} + V_{crx})$ .....3.1.

Where:

V_{cf} = disturbed soil by the front subsoiler ($O^/E^/G^/$).

V_{crx} = disturbed soil between the subsoilers ($FEE^/O^/$).

V_{cr} = the soil volume disturbed by the rear subsoiler in the absence of the front subsoiler, (EOG).

$V_{cr} = 0.5\ D\ w\ R_r$ ……..……..……..…….3.2.

$V_{cf} = 0.5\ d\ w\ R_f$…… ……..……..…….3.3.

$V_{crx} = w\ d\ x$…… ……..……..…….3.4.

Substituting equations 3.2, 3.3 and 3.4 into equation 3.1 and simplifying, gives the soil volume, V_{cx} disturbed by the rear subsoiler in this range as follows:

$$V_{cx} = \frac{1}{2} w\left[DR_r - d\left(R_f + 2x\right)\right] \quad \text{.....3.5.}$$

The total soil volume, V_{ct} disturbed by the two subsoilers in this region, is determined as follows:

$V_{ct} = V_{cr} = 0.5\ D\ w\ R_r$……..…….3.6.

ii). The spacing, x equal or greater than R_z ($x => R_z$).

Within this range, the disturbed soil volume between the subsoilers, V_{crx} is at maximum. Thus:

$V_{crx(max)} = w\ d\ R_z$…… ..…….3.7.

Substituting equations 3.2, 3.3 and 3.7 into equation 3.1 and simplifying, gives the volume of soil failed by the rear subsoiler. Thus:

$$V_{cx} = \frac{1}{2} w\left[DR_r - d\left(R_f + 2R_z\right)\right] \quad \text{.....3.8.}$$

When $x > R_z$, equation 3.8 is still remains valid but simplifies to $V_{cx} = 0.5zR_z$.

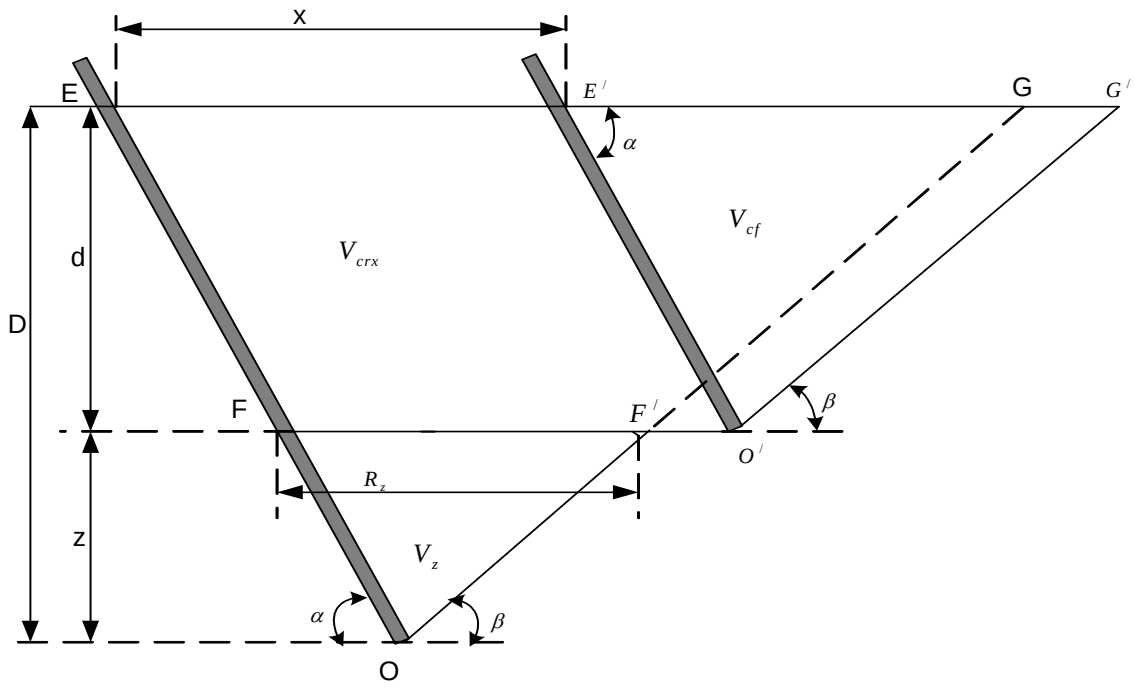

Figure 3.1.2: The center soil-failure wedge at a spacing, x > R_z.

From figure 3.1.2, the total soil volume, V_{ct} disturbed by both subsoilers can be expressed as follows:

$V_{ct} = V_{crx} + V_{cf} + V_z$ ..... 3.9.

$V_{crx} = d\ w\ x$ ..... 3.10.

$V_z = 0.5\ z\ w\ R_z$ ..... 3.11.

Substituting equations 3.3, 3.10 and 3.11 into equation 3.9 and simplifying, gives:

$$V_{ct} = \frac{dw}{2}\left(2x + R_f + \frac{z}{d}R_z\right) \quad \text{.....3.12.}$$

3.1.2 Forces acting on the rear subsoiler.

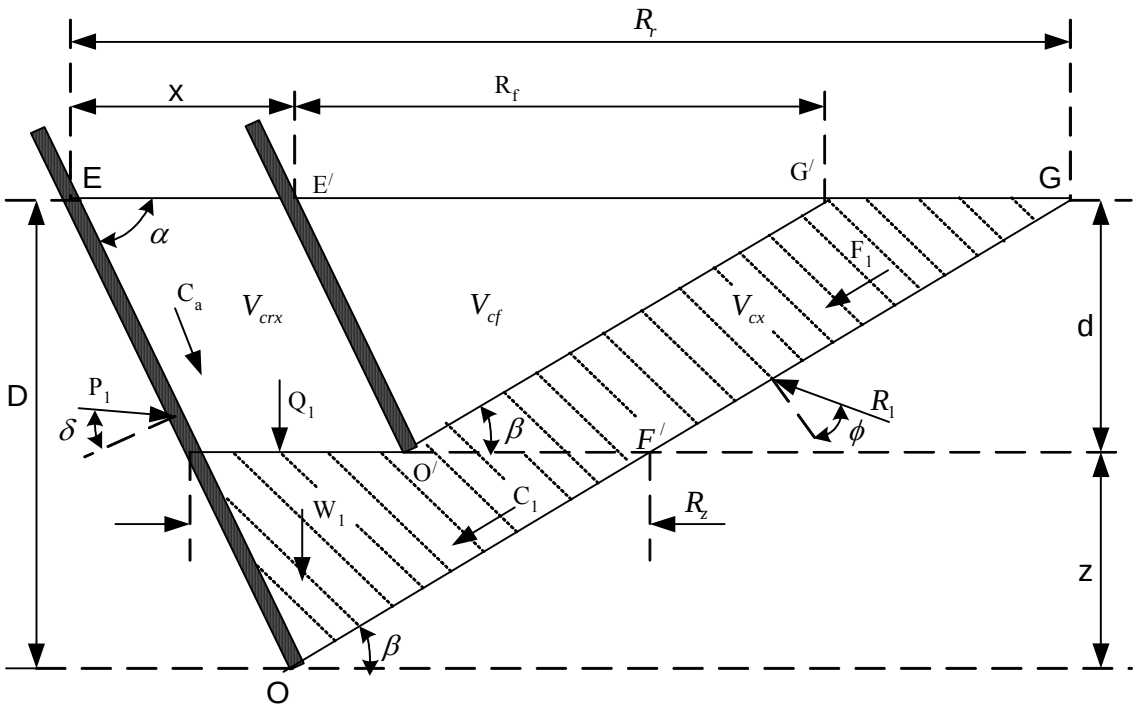

Figure 3.1.3: Forces acting on the rear subsoiler center soil-failure wedge.

Figure 3.1.3 presents the following forces acting on the rear subsoiler due to the failed center-wedge:

C_a – adhesion force at the soil/steel interface (N).

C_1 – cohesion force at the soil rapture plane (N).

F_1 – acceleration force (N).

R_1 – Soil reaction at the rupture plane (N).

Q_1 – surcharge force due to disturbed soil between the subsoilers (N).

W_1 – weight of soil disturbed by the rear subsoiler (N).

3.1.2.1 Weight of the disturbed soil by the rear subsoiler.

i). The spacing, x ranges between 0 and R_z (0 <= x < R_z).

The volume of soil disturbed by the rear subsoiler V_{cx} in this region, is given by equation 3.5 and its weight W_1 (fig. 3.1.3) is determined by the following expression:

$$W_1 = \frac{1}{2}\gamma w\left[DR_r - d\left(R_f + 2x\right)\right] \quad \text{.....3.13.}$$

Where γ = Undisturbed soil unit weight (Nm^{-3}).

ii). The spacing, x equal or greater than R_z (x=>R_z).

At this spacing, equation 3.8 gives the volume of soil disturbed by the rear subsoiler and its weight, W_1 is expressed as follows:

$$W_1 = \frac{1}{2}\gamma w\left[DR_r - d\left(R_f + 2R_z\right)\right] \quad \text{.....3.14.}$$

3.1.2.2 Cohesion force at the rapture surface for the rear subsoiler.

i). The spacing, x ranges between 0 and R_z (0 <= x < R_z).

In this region, the rapture plane for the rear subsoiler is equal to OG in figure 3.1.3. The cohesion force, C_1 can therefore be expressed as follows:

$$C_1 = \frac{c_c w}{\sin\beta} D \quad \text{.....3.15.}$$

ii). The spacing, x equal or greater than R_z (x=>R_z).

At this spacing, the rupture plane for the rear subsoiler is equal to $OF^{/}$ in figure 3.1.3. Therefore the cohesion force, C_1 is expressed as follows:

$$C_1 = \frac{c_c w}{\sin\beta} z \quad \text{.....3.16.}$$

3.1.2.3 Surcharge force due to the soil failed by the FSS.

i). The spacing, x ranges between 0 and R_z (0 <= x < R_z).

In this range, soil volumes V_{cf} is carried by the front subsoiler. The soil volume V_{crx} between the subsoilers, therefore exerts surcharge force on the rear subsoiler. Based on equation 3.4, the surcharge force Q_1 is expressed as:

$$Q_1 = \gamma dwx \quad \text{.....3.17.}$$

i). The spacing, x equal or greater than R_z ($x => R_z$).

Under this range, the surcharge force, Q_1 is due to soil volume $V_{crx(max)}$ defined by equations 3.7. It is therefore expressed as follows:

$$Q_1 = \gamma dwR_z \quad \text{.....3.18.}$$

3.1.2.4 Acceleration force.

i). The spacing, x ranges between 0 and R_z ($0 <= x < R_z$).

At this spacing, the front subsoiler is close to the rear subsoiler, therefore the front subsoiler is assumed to accelerate both V_{crx} and $V_{cf.}$ Hence the rear subsoiler accelerates V_z (fig. 3.1.2) and exerts an acceleration force, F_1 which is determined by the following Sohne's equation (1956):

$$F_1 = \frac{\gamma}{g} zwv^2 \frac{\sin\alpha}{\sin(\alpha+\beta)} \quad \text{.....3.19.}$$

Where:

v = tool speed (m/s).

g = gravitational constant (9.81m/s^2)

γ = soil unit-weight (kN/m^3).

ii). The spacing, x equal or greater than R_z ($x => R_z$).

Due to large spacing in this range, the soil volume V_{crx} settles behind the front subsoiler before it is re-accelerated by the rear subsoiler. Thus the acceleration force, F_1 exerted by the rear subsoiler is expressed as below:

$$F_1 = \frac{\gamma}{g} Dwv^2 \frac{\sin\alpha}{\sin(\alpha+\beta)} \quad \text{.....3.20.}$$

3.1.2.5 Adhesion force at the steel-soil interface.

Since the front subsoiler fails the soil up to the depth d, this failed soil layer exerts an insignificant mount of adhesion force to the rear subsoiler. Therefore the adhesion force, C_a for all x-values is due to the interface plane equivalent to the effective operating depth, z. It is expressed as follows:

$$C_a = \frac{wc_a}{\sin\alpha} z \quad \text{.....3.21.}$$

Where:

c_a = interface adhesion coefficient (N/m^2) .

3.1.3 Determination of the disturbed soil-volume and forces.

Referring to figure 3.1.3:

Summation of forces acting on the center failure-wedge in the horizontal plane.

$P_1 \sin(\alpha+\delta) = R_1 \sin(\beta+\phi) + C_1 \cos\beta + F_1 \cos\beta + C_a \cos\alpha.$

$R_1 = \{P_1 \sin(\alpha+\delta) - [C_a \cos\alpha + (C_1 + F_1)\cos\beta]/ \sin(\beta+\phi)$……..……..……3.22.

Summation of forces in vertical plane.

$P_1 \cos(\alpha+\delta) + R_1 \cos(\beta+\phi) = Q_1 + W_1 + (C_1 + F_1)\sin\beta - C_a \sin\alpha$…… ..……3.23.

Substituting equation 3.22 into 3.23 and solve for P_1.

$P_1 = \{Q_1 + W_1 + (C_1 + F_1)[\sin\beta + \cot(\beta+\phi)\cos\beta] - C_a[\sin\alpha + \cot(\beta+\phi)\cos\alpha]\}/ [\cos(\alpha+\delta) + \cot(\beta+\phi)\sin(\alpha+\delta)]$.

The horizontal force, H_1 in the direction of travel is determined:

$H_1 = P_1 \sin(\alpha+\delta)$.

$H_1 = \{Q_1 + W_1 + (C_1 + F_1)[\sin\beta + \cot(\beta+\phi)\cos\beta] - Ca[\sin\alpha + \cot(\beta+\phi)\cos\alpha]\}/ [\cot(\alpha+\delta) + \cot(\beta+\phi)]$.....3.24.

The vertical component:

$V_1 = P_1 \cos(\alpha+\delta)$.

$V_1 = \{Q_1 + W_1 + (C_1 + F_1)[\sin\beta + \cot(\beta+\phi)\cos\beta] - C_a[\sin\alpha + \cot(\beta+\phi)\cos\alpha]\}/$

$[1 + \cot(\beta+\phi)\tan(\alpha+\delta)]$ .....3.25.

The total soil volume, V_{t1} disturbed by the two subsoiler in the center wedge, is expressed as below:

$V_{t1} = V_{st}$ .....3.26.

3.2 Side soil-failure wedge.

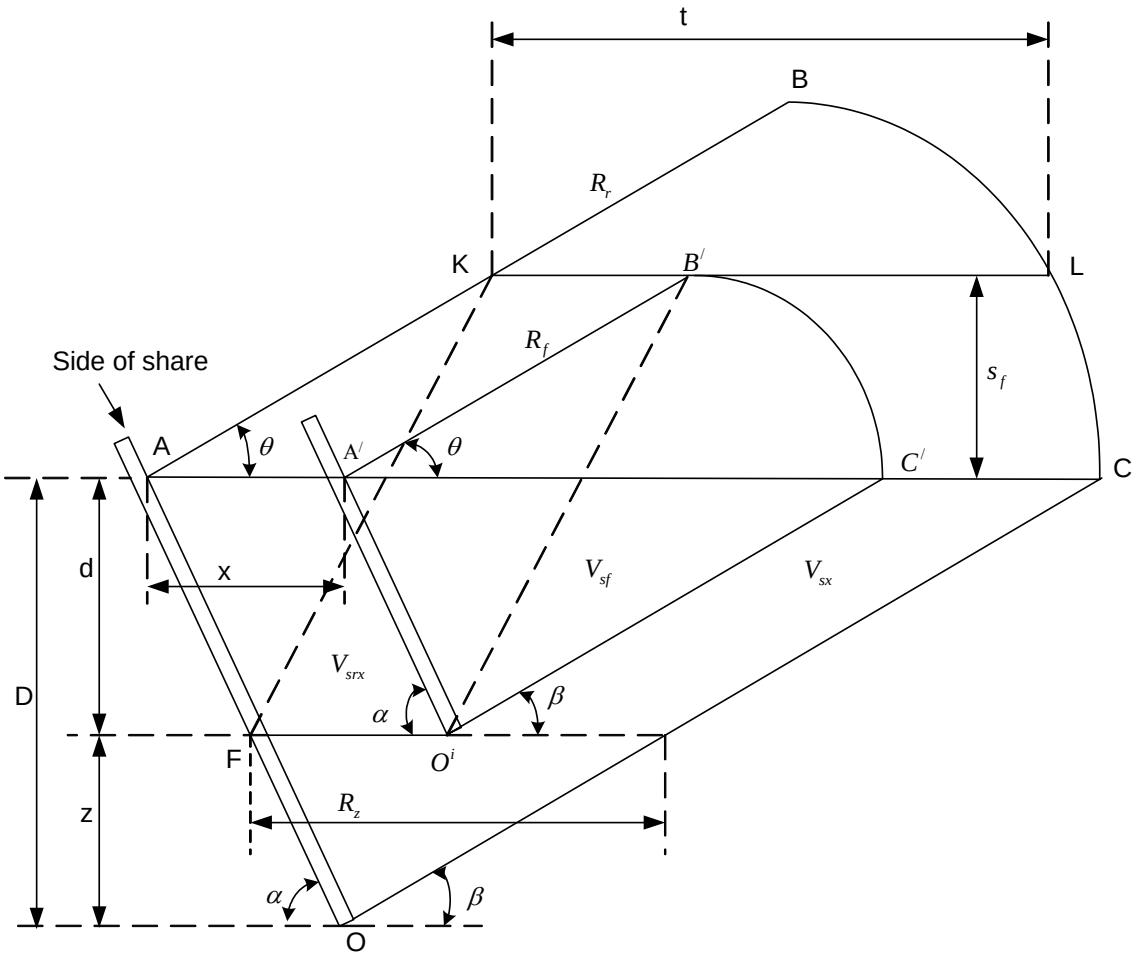

Figure 3.2.1: A side circular-wedge of the failed 3-D soil-profile.

Figure 3.2.1 shows a side circular soil-failure wedge when the spacing, x is less than the distance R_z. From the geometry of this figure:

$$t = \sqrt{R_r^2 - s_f^{\ 2}} - R_f \cos\theta \quad \text{.....3.27.}$$

According to Swick and Perumpral (1988), $\theta = \sin^{-1}(s_f/R_f)$.

Where:

s_f = Maximum width of the front side wedge (cm)

$s_f = 0.406(Rf) + 0.904(\alpha) - 6.03$ .....3.27a.

Figure 3.2.1a: A wire-model for the side circular-wedge when $x<R_z$.

Figure 3.2.1a shows a wire-model representing the three-dimensional two side circular-wedges of the right of the symmetric axis when viewing forward, at the spacing, x less than the distance R_z.

Unlike the center wedge, it was not easy to derive equations for the side circular-wedge because it was very difficult to visualize what happens at the sides as the spacing was varied. This wire-model put the researcher in position to visualize the geometry for

different spacings when the subsoiler spacing was varied and constituted a breakthrough for the researcher. Before the fabrication of this model, he could not proceed with the equations. With this wire-model, it was even possible to measure certain distances and lengths, and compare them with the developed equations for wedge dimensions.

3.2.1 Soil volume disturbed in the side wedge.

The soil volume V_{sx} disturbed by the rear subsoiler and the total volume V_{st} failed by both subsoilers in the side wedge, vary with the spacing, x as follows:

i). The spacing, x ranges between 0 and R_z ($0 <= x < R_z$).

At this spacing, the soil volume V_{sx} is made up of the portion between the circular surfaces defined by FOCBK and $B^{/}C^{/}O^{/}$ of figure 3.2.1. It is therefore expressed as:

$$V_{sx} = V_{sr} - (V_{sf} + V_{srx}) \quad \text{.....3.28.}$$

Where:

V_{sf} = the soil volume ($A^{/}B^{/}C^{/}O^{/}$) disturbed by the front subsoiler.

V_{sr} = the soil volume (ABCO) disturbed by the rear subsoiler, in the absence of the front subsoiler.

V_{srx} = the soil volume between triangles AKF and $B^{/}A^{/}O^{/}$

The area of triangle AKF = $0.5\ R_f\ d/\sin\alpha$.

The volume, V_{srx} therefore is expressed as follows:

$$V_{srx} = \frac{d}{2} R_f x \sin\theta \quad \text{.....3.29.}$$

(θ is applicable for the shortest distance between triangles AKF and $A^{/}B^{/}O^{/}$)

The volumes of the side circular failure wedges are determined by intergrating over angle increments as outlined by Godwin (1974). Using this technique, the soil volume in the differential element $O^{/}PA^{/}Q$ (fig.3.2.2) is determined by the following expression:

The volume of the differential element, $O'PQA' = dV_{sf} = (1/6)d\ R_f^2\ d\theta$.

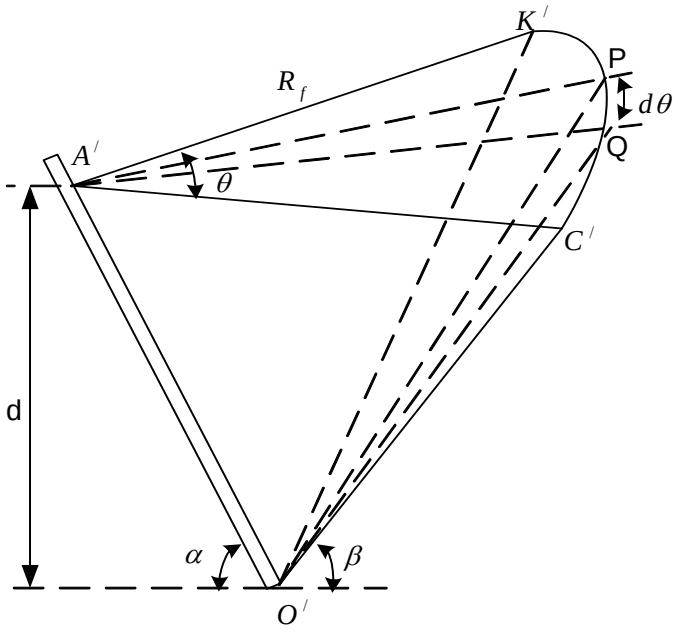

Figure 3.2.2: Definition of volume V_{sf} disturbed by FSS.

$$V_{sf} = \frac{1}{6} dR_f^2 \int_0^{\theta} d\theta = \frac{1}{6} dR_f^2 .\theta \quad \text{.....3.30.}$$

Similarly for the rear subsoiler:

$$V_{sr} = \frac{1}{6} DR_r^2 \theta \quad \text{.....3.31.}$$

Where: θ is in radians.

Substituting equations 3.29, 3.30 and 3.31 into equation 3.28 gives the volume V_{sx}:

$$V_{sx} = \frac{1}{6}\left[DR_r^2\theta - dR_f\left(R_f\theta + 3x\sin\theta\right)\right] \quad \text{.....3.32.}$$

The volume, V_{st} of soil disturbed by both subsoilers in this range is expressed as follows:

$$V_{st} = V_{cr} = \frac{1}{6} DR_r^2 \theta \quad \text{.....3.33.}$$

ii). The spacing, x ranges between R_z and t (R_z<= x <t).

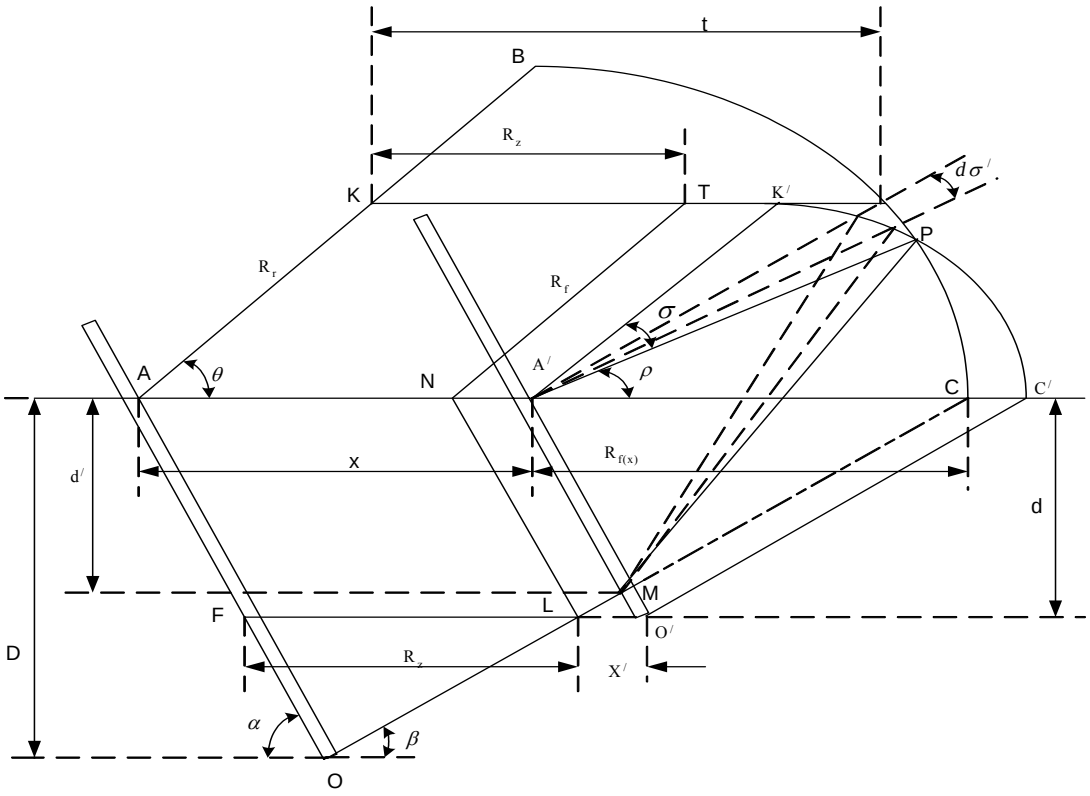

Figure 3.2.3: A circular side failure-wedge when R_z <= x < t.

Figure 3.2.3a: A wire-model for the circular side failure-wedge when R_z <= x < t.

At this spacing, the soil volume between the subsoilers consists of two portions of figure 3.2.3. Namely:

- Soil between triangles AFK and TLN = V_{srx}
- Soil between triangles NLT and $A^{/}K^{/}M = V_{stx}$.

Apart from the soil between the subsoilers, within ABPCO (fig.3.2.3), the front subsoiler also disturbs the soil volume in the curved surface $A^{/}K^{/}PCM$ and it consists of:

- The soil volume $A^{/}K^{/}PM = V^{/}_{1}$.
- The soil volume $A^{/}PCM = V^{/}_{2}$.

These two volumes are difined as V_{sfx} and thus expressed as follows:

$$V_{sfx} = V^{/}_{1} + V^{/}_{2} \quad \text{.....3.34.}$$

Therefore at this spacing, the volume V_{sx} disturbed by the rear subsoiler can be expressed as:

$$V_{sx} = V_{sr} - (V_{srx} + V_{stx} + V_{sfx}) \quad \text{.....3.35.}$$

The soil volumes between the subsoilers V_{srx} and V_{stx} are determined as below:

$$V_{srx} = \frac{d}{2} R_f R_z \sin\theta \quad \text{.....3.36.}$$

Reffering to figure 3.2.3b extracted from figure 3.2.3, the volume V_{stx} is determined as follows:

The area of triangle LNT = $R_f.d/2\sin\alpha$, hence the volume between triangles NLT and $A^{/}O^{/}K^{/} = 0.5\ d\ R_f\ x^{/}\ \sin\theta$ .....3.37.

Where:

$x^{/} = x\text{-}R_z$.

The volume, V between surfaces LTK/M and LTK/O/ (fig. 3.2.3b) is given by the following equation:

$$V = \frac{hx^{/}}{2} R_f \frac{\sin\alpha}{\cos\beta} \quad \text{.....3.38.}$$

Subtracting equation 3.38 from equation 3.37, the required volume between triangles NLT and A/MK/ (fig. 3.2.3b) equal to V_{stx} is obtained and thus:

$$V_{stx} = \frac{R_f}{2} x^{/} \left(d\sin\theta - \frac{\sin\alpha}{\cos\beta} h \right) \quad \text{.....3.39.}$$

The value of h in equation 3.39 can be determined from the geometry of triangle LMO/ in fgure 3.2.3b. Thus:

$$h = \frac{x^{/}}{\cot\beta + \cot\alpha}$$

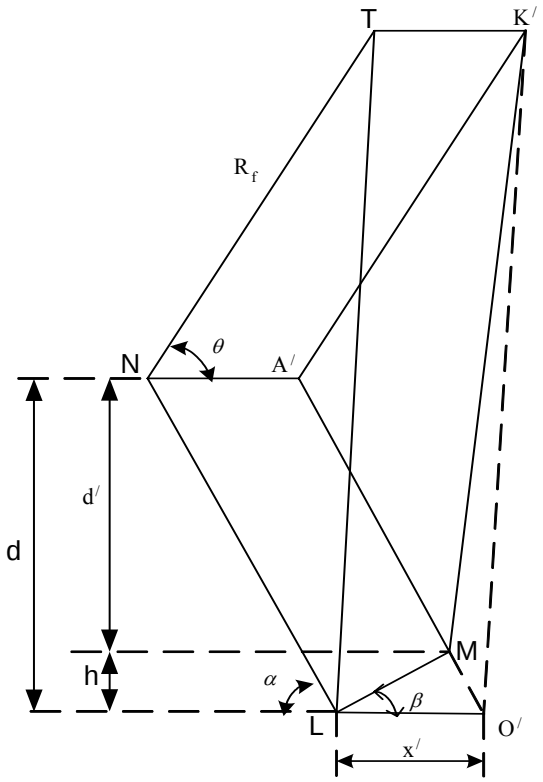

Figure 3.2.3b: Definition of volume V_{stx}.

The volume V_{sfx} i.e. portion $A^{/}K^{/}PCM$ of figure 3.2.3, consists of volumes $V^{/}_1$ and $V^{/}_2$ as indicated in equation 3.34. Therefore it is determined as follows:

$$V_1^{/} = \frac{1}{6} R_f^2 d^{/} \int_{\rho}^{\theta} d\sigma = \frac{1}{6} R_f^2 d^{/} \sigma \Big|_{\rho}^{\sigma} \quad \text{.....3.34}a.$$

Where:
$d^{/} = d - h.$

From figure 3.2.3c, when $x = R_z$, $\rho = 0$ while $\rho = \theta$ when $x = t$. The values of ρ when x is equal to any value between R_z and t can be easily interpolated since $\sigma + \rho = \theta$.

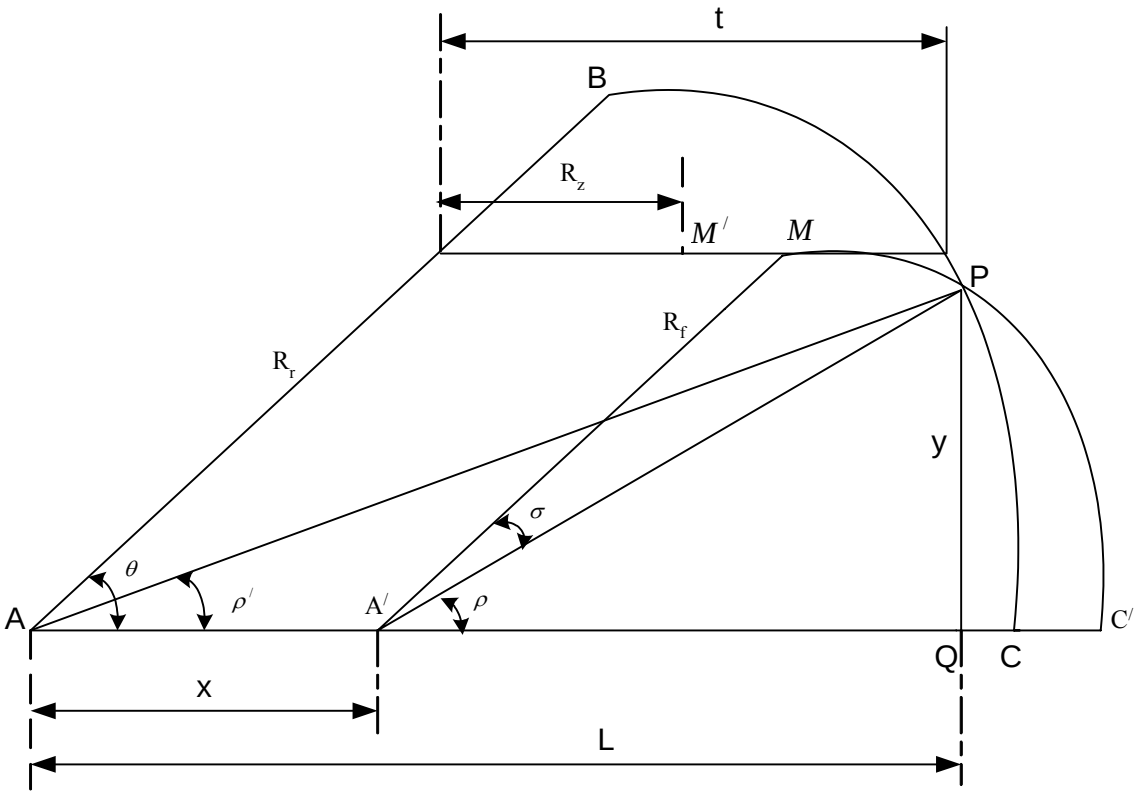

Figure 3.2.3c: Side circular wedges overlap when $R_z <= x < t$.

Figure 3.2.3c shows the top view of the front and rear side wedges overlaping when x ranges between R_z and t. When $x = R_z$, point M moves to $M^{/}$. From this figure, $V^{/}_2$ in equation 3.34 can be determined by calculating the area of arc $A^{/}PC$ and multiplying it

with the operating depth. Thus from triangle APQ:

$L^2 + y^2 = R_r^2$ .....i.

And from traingle $A^/PQ$;

$(L-x)^2 + y^2 = R^2_f$ ..... ii.

From equations i and ii, we solve for L.

$L = (R^2_r - R^2_f + x^2)/ 2x.$

$$Cos\rho^{/} = \frac{L}{R_r} = (R_r^2 - R_f^2 + x^2)/2x.R_r$$

Let $X = (R^2_r - R^2_f + x^2)/ 2x\ R_r$, therefore $\rho^/ = Cos^{-1}X$.

The area of $A^/PC = (1/2)\rho^/R^2_r$ – Area $APA^/ = (1/2)[\rho^/R^2_r - R_r x.\sin\rho^/]$.

Therefore the volume, $V^/_2$ in equation 3.34 is defined as follows:

$$V_2^{/} = \frac{d^{/}}{6}\left(R_r^2\rho^{/} - R_r x\sin\rho^{/}\right) \text{.....3.34}b.$$

Substituting equations 3.34a and 3.34b into equation 3.34 gives:

$$V_{sfx} = \frac{d^{/}}{6}\left(R_f^2\sigma + \rho^{/}R_r^2 - R_r x\sin\rho^{/}\right) \text{.....3.40.}$$

Then substituting equations 3.31, 3.36, 3.39 and 3.40 into equation 3.35 and simplifying, gives the volume V_{sx} disturbed by the rear subsoiler at this spacing:

$$V_{sx} = \frac{d}{6}R_f\left\{\frac{DR_r^2}{dR_f}\theta - \left[3R_z\sin\theta + 3x^{/}\left(\sin\theta - \frac{h\sin\theta}{d\cos\beta}\right) + \right.\right.$$

$$\left.\left.\frac{R_r d^{/}}{R_f d}\left(\frac{R_f^2}{R_r}\sigma + \rho^{/}R_r - x\sin\rho^{/}\right)\right]\right\} \text{.....3.41.}$$

The soil volume, V_{st} disturbed by both subsolers in this region, is determined as follows:

$V_{st} = V_{sr} + V'_{sf}$ ..... 3.42.

Where:

V'_{sf} = the soil volume disturbed by the front subsoiler.

$V'_{sf} = V_{sf} - V_{sfx}$ ..... 3.43.

Substituting equations 3.30 and 3.40 into 3.43, then substituting equations 3.43 and 3.31 into 3.42 and simplifying, the soil volume (V_{st}) disturbed by both subsoilers is expressed as follows:

$$V_{st} = \frac{1}{6}R_r^2\left(D\theta + d'\rho' - \frac{d'}{R_r}x\sin\rho'\right) + \frac{1}{6}R_f^2\left(d\theta - d'\sigma\right) \quad \text{.....3.44.}$$

iii). The spacing x, equal or greater than t (x=>t).

The volume V_{stx} between triangles NLT and $A'MK'$ (fig. 3.2.3b), at this spacing is expressed as below:

$$V_{stx} = \frac{1}{2}R_f x'\left(\frac{d}{\sin\alpha}\sin\theta - h\frac{\sin\alpha}{\cos\beta}\right) \quad \text{.....3.45.}$$

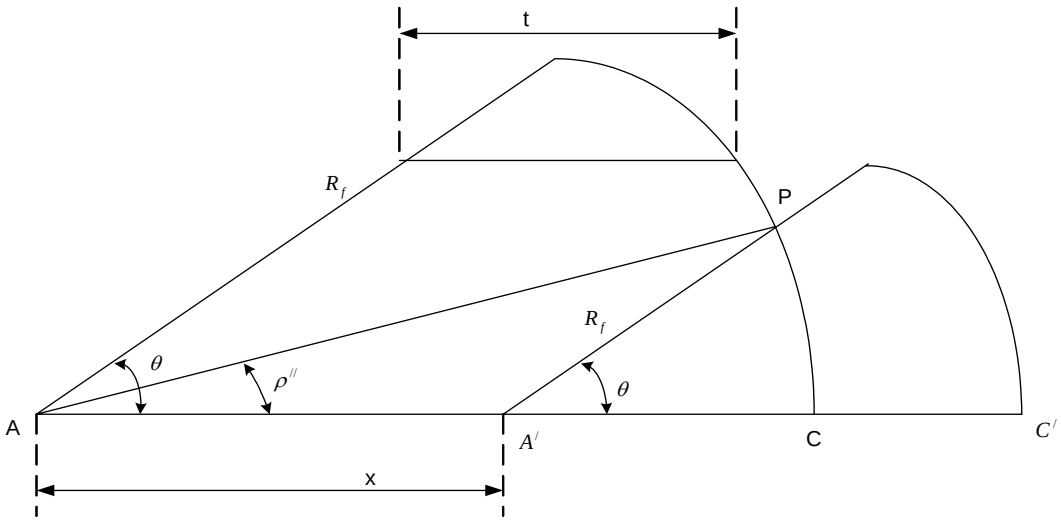

Figure 3.2.4: Side circular wedges overlapping when x>t.

Figures 3.2.4 and 3.2.4a show the top view of the rear and front side wedges overlapping when "x" exceeds "t". $A^{/}PC$ is the top view of V_{sfx} (equation 3.34). Therefore calculating the area of arc $A^{/}PC$ and multiplying it with the operating depth determines V_{sfx}. Thus:

Area $A^{/}PC$ = (Area of arc APC – Area of triangle $APA^{/}$) = $(1/2)R_r(R_r\rho^{//} - x\sin\rho^{//})$.

The volume, $V_{sfx} = (1/6)R_r d^{/}[R_r\rho^{//} - x\sin\rho^{//}]$.....3.46.

Note;

$\rho^{//} = Cos^{-1}X$ when x = t and $\rho^{//} = 0$ when x => R_r. Then when x is equal to any value between t and R, then $\rho^{//}$ can be interpolated.

Figure 3.2.4a: The wire-model for the side circular-wedges when x>t.

Substituting equations 3.31, 3.45, 3.46 and 3.47 into equation 3.34 and simplifying, gives the soil-volume (V_{sx}) disturbed by the RSS at this spacing:

$$V_{sx} = \frac{R_f d}{6}\left\{\frac{DR_r^2}{R_f d}\theta - \left[3R_z\sin\theta + 3x^{/}\left(\frac{\sin\theta}{\sin\alpha} - \frac{h\sin\alpha}{d\cos\beta}\right) + \frac{R_r d^{/}}{R_f d}\left(R_r\rho^{//} - x\sin\rho^{//}\right)\right]\right\}.....3.48.$$

The soil volume (V_{st}) disturbed by the two subsoilers at this spacing can be determined by substituting equations 3.30 and 3.34 into 3.43. Then substituting equations 3.31 and

3.43 into 3.42. After simplifying, the soil volume (V_{st}) disturbed by both subsoilere is expressed as follows:

$$V_{st} = \frac{1}{6}R_r^2\left(D\theta - d'\rho'' + \frac{x}{R_r}\sin\rho''\right) + \frac{1}{6}dR_f^2\theta \quad \text{.....3.49.}$$

3.2.2 Forces acting on the rear subsoiler due to the side wedge.

To determine the forces acting on the rear subsoiler due to the side wedge, integrals of the force components acting on the differential element AOPQ in figure 3.2.5 were calculated. Below are the procedures followed.

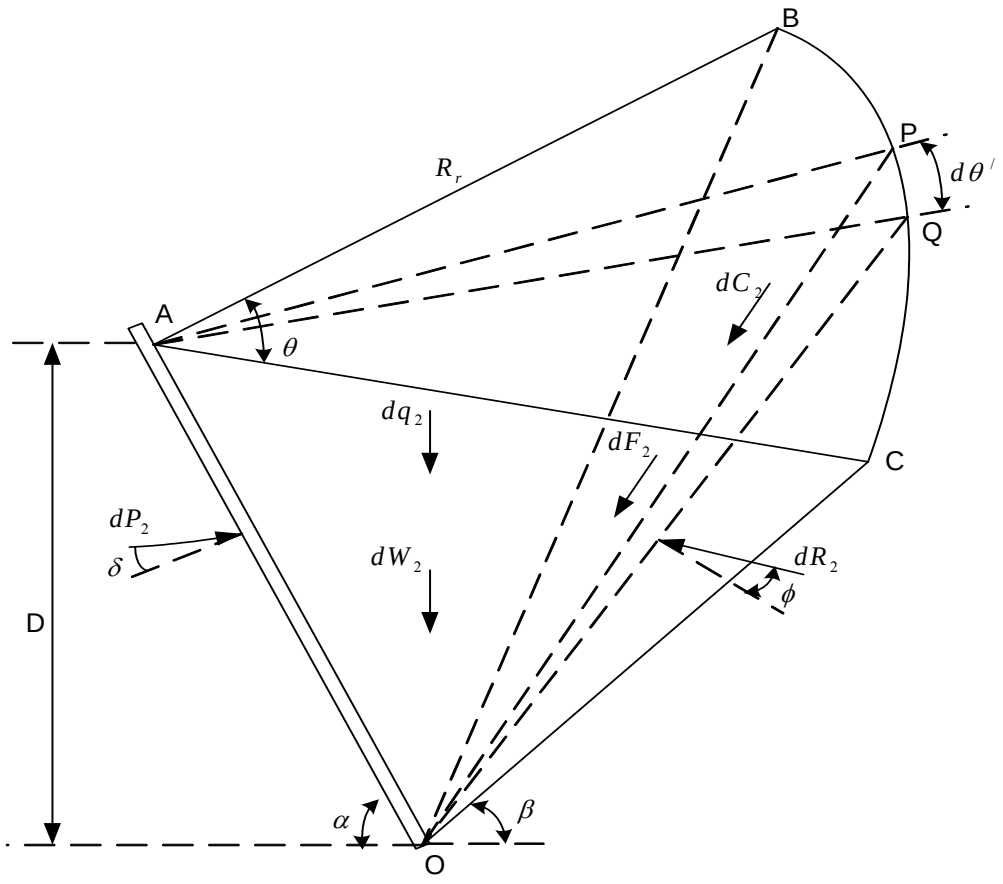

Figure 3.2.5: Forces acting on the side circular wedge failed by the RSS.

3.2.2.1 Weight of the disturbed soil mass by the rear subsoiler.

i). The spacing, x ranges between 0 and R_z (0 <= x < R_z).

From equation 3.32, the weight (dw_2) of the soil disturbed by the rear subsoiler in the differential element is expressed as below:

$$dw_2 = \frac{1}{6}\gamma\left[DR_r^2 - dR_f\left(R_f + 3\sin\theta.x\right)\right]d\theta' \quad \text{.....3.50.}$$

Where:

γ = Unit weight of soil (kNm^{-3}).

ii). The spacing, x ranges between R_z and t (R_z<= x < t).

From equation 3.40, the weight (dw_2) of the soil disturbed by the rear subsoiler in the differential element is determined as follows:

$$dw_2 = \frac{d}{6}\gamma R_f\left\{\frac{DR_r^2}{dR_f} - 3\left[R_z\sin\theta + x'\left(\sin\theta - \frac{h\sin\theta}{d\cos\beta}\right) + \right.\right.$$

$$\left.\left.\frac{R_r d'}{3R_f d}\left(\frac{R_f^2}{R_r}\sigma + \rho' R_r - x\sin\rho'\right)\right]\right\}d\theta' \quad \text{.....3.51.}$$

iii). The spacing, x equal or greater than t (x=>t).

From equation 3.31, the weight (dw_2) of the soil disturbed by the rear subsoiler in the differential element is expressed:

$$dw_2 = \frac{R_f d}{6}\left\{\frac{DR_r^2}{R_f d} - 3\left[R_z\sin\theta + x'\left(\frac{\sin\theta}{\sin\alpha} - \frac{h\sin\theta}{d\cos\beta}\right) + \right.\right.$$

$$\left.\left.\frac{d' R_r}{3dR_f}\left(R_r\rho'' - x\sin\rho''\right)\right]\right\}d\theta' \quad \text{.....3.52.}$$

3.2.2.2 Cohesion Force at the Rapture Surface of the Rear Subsoiler.

i). The spacing, x ranges between 0 and R_z (0 <= x < R_z).

Differential element cohesion force, dc_2:

$$dc_2 = \frac{c_c D R_r}{2\sin\beta} d\theta' \quad \text{.....3.53.}$$

Where:

c_c = Soil cohesion coefficient (kNm^{-2}).

ii). The spacing, x ranges between R_z and t (R_z<= x < t).

Differential element cohesion force, dc_2:

$$dc_2 = \frac{c_c z R_z}{2\sin\beta} d\theta' \quad \text{.....3.54.}$$

iii). The spacing, x equal or greater than t (x=>t).

$$dc_2 = \frac{c_c z R_z}{2\sin\beta} d\theta' \quad \text{.....3.54.}$$

3.2.2.3 Surcharge due to the soil failed by the front subsoiler.

i). The spacing, x ranges between 0 and R_z (0 <= x < R_z).

Surcharge pressure, dq_2 on the differential element is contributed by the differential elements of V_{sf} and V_{srx} in equation 3.28 Therefore dq_2 can be expressed as follows:

$$dq_2 = \frac{1}{6}\gamma R_f d\left(R_f + 3\sin\theta.x\right)d\theta.' \quad \text{.....3.55.}$$

ii). The spacing, x ranges between R_z and t (R_z <= x < t).

In this region, the surcharge pressure, dq_2 on the differential element is contributed by the differential elements of V_{srx}, V_{stx} and V_{sfx} in equation 3.35. Thus, dq_2:

$$dq_2 = \frac{dR_f}{2}\gamma\left[R_z \sin\theta + x'\left(\sin\theta - \frac{h\sin\theta}{d\cos\beta}\right) + \right.$$

$$\left.\frac{d'R_r}{3dR_f}\left(\frac{R_f^2}{R_r}\sigma + R_r\rho' - x\sin\rho'\right)\right]d\theta' \quad \text{.....3.56.}$$

iii). The spacing, x equal or greater than t (x=>t).

Similarly, in this region dq_2 is due to the same differential elements as in section b above. Therefore for dq_2:

$$dq_2 = \frac{dR_f}{2}\gamma\left[R_z \sin\theta + x'\left(\frac{\sin\theta}{\sin\alpha} - \frac{h\sin\theta}{d\cos\beta}\right) + \frac{d'R_r}{3dR_f}\left(R_r\rho'' - x\sin\rho''\right)\right]d\theta' \quad \text{.....3.57.}$$

3.2.2.4 Acceleration Force.

i). The spacing, x ranges between 0 and R_z (0 <= x < R_z).

Differential element acceleration force, dF_f due to the front subsoiler:

$$dF_f = \frac{1}{2g}\gamma dR_f v^2 \frac{\sin\beta}{\sin(\alpha+\beta)}d\theta'$$

Where:

g = gravitational constant ($9.81 ms^{-2}$).

v = operating speed (ms^{-1}).

γ = soil-unit weight (Nm^{-3}).

Differential element acceleration force, dF_r due to the rear subsoiler:

$$dF_r = \frac{1}{2g}\gamma DR_r v^2 \frac{\sin\beta}{\sin(\alpha+\beta)}d\theta'.$$

Actual differential element acceleration force, $dF_2 = dF_r - dF_f$. Thus:

$$dF_2 = \frac{1}{2g}\gamma v^2 \frac{\sin\beta}{\sin(\alpha+\beta)}[R_r D - R_f d]d\theta' \quad \text{.....3.58.}$$

ii). The spacing, x ranges between R_z and t (R_z <= x < t).

The volume of soil accelerated by the rear subsoiler, $V_{ra} = V_{sr} - V_{sfx}$.

Therefore the actual differential element acceleration force, dF_2 due to the rear subsoiler:

$$dF_2 = \frac{1}{2g}\gamma R_r v^2 d(x)\frac{\sin\beta}{\sin(\alpha+\beta)}\left[\frac{D}{d(x)} - \rho' + \sin\rho' + \frac{R_f}{R_r}\right]d\theta' \quad \text{.....3.59.}$$

iii). The spacing, x equal or greater than t (x=>t).

The volume of soil accelerated by the rear subsoiler, $V_{ra} = V_{sr} - V_{sfx}$.

Therefore the actual differential element acceleration force, dF_2 due to the rear subsoiler:

$$dF_2 = \frac{1}{2g}\gamma R_r v^2 d(x)\frac{\sin\beta}{\sin(\alpha+\beta)}\left[\frac{D}{d(x)} - \rho'' + \sin\rho''\right]d\theta' \quad \text{.....3.60.}$$

3.2.3 Determination of the disturbed soil-volume and forces.

Referring to figure 3.2.5:

i). Summation of forces on the differential element in the horizontal direction.

$dP_2 \sin(\alpha+\delta) = dR_2 \sin(\beta+\phi) + dc_2 \cos\beta + dA_2 \cos\beta.$

$dR_2 = [dP_2 \sin(\alpha+\delta) - \cos\beta\,(dc_2 + dA_2)]/\sin(\beta+\phi)$ .....3.61.

ii). Summation of forces on the differential element in the vertical direction.

$dP_2 \cos(\alpha+\delta) + dR_2 \cos(\beta+\phi) = dq_2 + dw_2 + dc_2 \sin\beta + dA_2 \sin\beta$ .....3.62.

Substituting equation 3.61 into 3.62 and solve for dP_2.

$dP_2 = \{dq_2 + dw_2 + dc_2 [\sin\beta + \cos\beta \cot(\beta+\phi)] + dA_2 [\sin\beta + \cos\beta \cot(\beta+\phi)]\}/$

$[\cos(\alpha+\delta) + \cot(\beta+\phi) \sin(\alpha+\delta)].$

The horizontal component, $dh_2 = dP_2 \sin(\alpha+\delta)$.

$dh_2 = \{dq_2 + dw_2 + dc_2 [\sin\beta + \cos\beta \cot(\beta+\phi)] + dA_2 [\sin\beta + \cos\beta \cot(\beta+\phi)]\}/$
$[\cot(\alpha+\delta) + \cot(\beta+\phi)].$

The horizontal component parallel to the direction of travel, $dH_2 = dh_2 \cos\theta^{/}$.
Where $\theta^{/}$ is the angle to the direction of travel in which dh_2 acts. The total horizontal force required to fail the crescents on the both sides of the soil failure wedge is equal to H_2.

$$H_2 = \int_0^{\theta} dh_2 \cos\theta^{/} \quad \text{.....3.63}a.$$

The vertical component, $dv_2 = dP_2 \cos(\alpha+\delta)$.
$dv_2 = \{dq_2 + dw_2 + dc_2 [\sin\beta + \cos\beta \cot(\beta+\phi)] + dA_2 [\sin\beta + \cos\beta \cot(\beta+\phi)]\}/$
$[1 + \cot(\beta+\phi)\tan(\alpha+\delta)].$

$dV_2 = dv_2 \cos\theta^{/}$

$$V_2 = \int_0^{\theta} dv_2 \cos\theta^{/} \quad \text{.....3.63}b.$$

The soil volume, V_{t2} failed by both subsoilers is expressed as below:

$V_{t2} = V_{st}\ldots$ .....3.64.

3.2.3.1 Integrals of the force components in equations 3.63a and b.

(a). Surcharge due to soil failed by the front subsoiler.

i). The spacing, x ranges between 0 and R_z ($0 <= x < R_z$).

$$Q_2 = \frac{1}{X_1}\int_0^{\theta} dq_2 \cos\theta^{/}.$$

$$Q_2 = \frac{1}{6X_1}\gamma R_f d\left[R_f + 3\sin\theta.x\Big|_0^{Rz}\right]\sin\theta \quad \text{.....3.65}a.$$

Where:

$X_1 = \cot(\alpha+\delta) + \cot(\beta+\phi)$.

ii). The spacing, x ranges between R_z and t (R_z <= x < t).

$$Q_2 = \frac{dR_f}{2X_1}\gamma\left[R_z\sin\theta + x'\sin\theta\left(1-\frac{h}{d\cos\beta}\right)+\frac{d'R_r}{3dR_f}\left(\frac{R_f^2}{R_r}\sigma + R_r\rho' - x\sin\rho'\right)\right]\sin\theta \quad \text{.....3.65}b.$$

iii). The spacing, x equal or greater than t (x=>t).

$$Q_2 = \frac{dR_f}{2X_1}\gamma\left[R_z\sin\theta + x'\sin\theta\left(\frac{1}{\sin\alpha}-\frac{h}{d\cos\beta}\right)+\frac{d'R_r}{3dR_f}\left(R_r\rho'' - x\sin\rho''\right)\right]\sin\theta \quad \text{.....3.65}c.$$

(b). Weight of the soil disturbed by the rear subsoiler.

i). The spacing, x ranges between 0 and R_z (0<= x < R_z).

$$W_2 = \int_0^{\theta} dw_2\cos\theta'.$$

$$W_2 = \frac{1}{6X_1}\gamma\left[DR_r^2 - R_f d\left(R_f + 3x\sin\theta.\right)\right]\sin\theta \quad \text{.....3.66}a.$$

ii). The spacing, x ranges between R_z and t (R_z <= x < t).

$$W_2 = \frac{dR_f}{6X_1}\gamma\left\{\frac{DR_r^2}{dR_f} - 3\left[R_z\sin\theta + x'\sin\theta\left(1-\frac{h}{d\cos\beta}\right)+\right.\right.$$

$$\left.\left.\frac{d'R_r}{3dR_f}\left(\frac{R_f^2}{R_r}\sigma + \rho' R_r - x\sin\rho'\right)\right]\right\}\sin\theta \quad \text{.....3.66}b.$$

iii). The spacing, x equal or greater than t (x=>t).

$$W_2 = \frac{dR_f}{6X_1}\gamma\left\{\frac{DR_r^2}{dR_f} - 3\left[R_z \sin\theta + x^{/} \sin\theta\left(\frac{1}{\sin\alpha} - \frac{h}{\cos\beta}\right) + \right.\right.$$

$$\left.\left.\frac{d^{/}R_r}{3dR_f}\left(R_r\rho^{//} - x\sin\rho^{//}\right)\right]\right\}\sin\theta \quad \text{.....3.66}c.$$

(c). Cohesion Force at the Rupture Surface.

i). The spacing, x ranges between 0 and R_z (0<= x < R_z).

$$C_2 = \int_0^{\theta} dc_2 \cos\theta^{/}$$

$$C_2 = X_2 \frac{cDR_r}{2\sin\beta}\sin\theta \quad \text{.....3.67}a.$$

Where:

$X_2 = [\sin\beta + \cos\beta \cot(\beta+\phi)]/[\cot(\alpha+\delta) + \cot(\beta + \phi)]$.

ii). The spacing, x range between R_z and t (R_z <= x <t).

$$C_2 = X_2 \frac{c_c zR_z}{2\sin\beta}\sin\theta \quad \text{.....3.67}b.$$

iii). The spacing, x equal or greater t (x=>t).

$$C_2 = X_2 \frac{c_c zR_z}{2\sin\beta}\sin\theta \quad \text{.....3.67}c.$$

(d). Acceleration Force.

i). The spacing, x ranges between 0 and R_z (0<= x < R_z).

$$F_2 = \int_0^{\theta} dA_2 \cos\theta^{/}$$

$$F_2 = \frac{X_2}{6g}\gamma v^2 \frac{\sin\beta}{\sin(\alpha+\beta)}\left(DR_r - R_f d\right)\sin\theta \quad \text{.....3.68}a.$$

ii). The spacing, x ranges between R_z and t (R_z <= x < t).

$$F_2 = \frac{X_2}{2g}\gamma R_r d' v^2 \frac{\sin\beta}{\sin(\alpha+\beta)}\left[\frac{D}{d'} - \rho' + \sin\rho' - \frac{R_f}{R_r}\right]\sin\theta \quad \text{.....3.68}b.$$

iii). The spacing, x equal or greater than t (x=>t).

$$F_2 = \frac{X_2}{2g}\gamma R_r d' v^2 \frac{\sin\beta}{\sin(\alpha+\beta)}\left[\frac{D}{d'} - \rho'' + \sin\rho''\right]\sin\theta \quad \text{.....3.68}c.$$

3.2.4 Frictional force acting on the sides of the rear subsoiler.

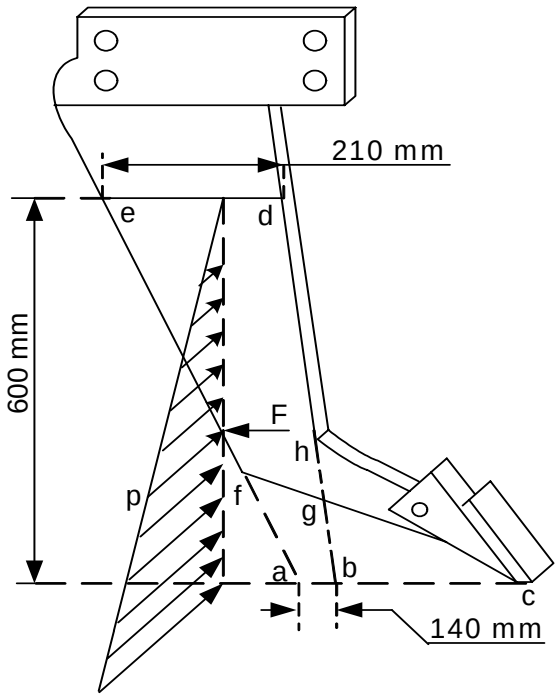

Figure 3.2.6: Soil pressure distribution on each side of the rear subsoiler.

The maximum soil pressure, $p_{max} = c\gamma h$ (kPa).....3.69a.

And the average soil pressure, $p_{av} = 0.5c\gamma h$ (kPa).....3.69b.

Where:

γ = Soil unit weight (kNm^{-3}).

g = Gravitational constant (9.81 ms^{-2}).

h = Distance from the soil surface to the point of action (m).

$$c = \frac{1 - \sin\phi}{1 + \sin\phi}$$

According to McKyes (1989) ϕ ranges between 25^0 and 41^0. Thus:

For $\phi = 36^0$, c = 0.26.

The total adhesion and friction force, $F_{tot} = 2A[c_a + p_{av} \tan\delta)$ .....3.70.

For $\phi = 36^0$; F_{tot} = 2 x 0.175 x 0.6(7 + 1.55 x 0.467) = 1.62 kN.

Where:

$\mu = \tan\delta$ = 0.467; Frictional coefficient.

A = Area abde (m^2).

Area cgh of the tool is approximated by area abgf.

3.3 Determination of the total disturbed soil-volume and forces.

The total volume of soil, V_T failed by the two subsoilers is given by:

$V_T = V_{t1} + 2V_{t2}$… .....3.71.

The total draft force, H required for the rear subsoiler to fail the center and the two side circular wedges, is expressed as:

$H = H_1 + 2H_2$… .....3.72.

The resulting total vertical load, V acting on the rear subsoiler, is expressed as:

$V_r = V_1 + 2V_2$ .....3.73.

Ploughing tests conducted with a moldboard plough indicated that 50% of the exerted draft force per unit area tilled, is used for cutting, 30% accounts for elevating, pulverizing and inverting the tilled soil slice and 20% is used for overcoming the rolling resistance (Brainer, Kepner and Barger, 1950). A subsoiler does not elevate or invert the

tilled soil and no wheels were used, therefore it is assumed that 30% of its draft force requirements per unit area tilled accounts for pulverizing the soil. Godwin (1974) expressed the maximum cross-sectional area of a tilled profile as follows:

$$A = d(w+s) \quad \text{.....3.72.}$$

The cross-sectional area tilled by the rear subsoiler:

$$A_r = w(D - d) + (D * s_r - d * s_f) \quad \text{.....3.73.}$$

A_r = Maximum cross-sectional area tilled by the RSS (m^2).
d = Operating depth of the FSS (m).
D = Operating depth of the RSS (m).
s_f = Maximum width the side wedge failed by the FSS (m).
s_r = Maximum width the side wedge failed by the RSS (m).
w = Operating width of the subsoilers (m).

Srivastava et al (1993) indicated the values of specific draft for sandy clay loam soil when tilled by a moldboard plough, to range between 4 and 8 Ncm^{-2}. In this study a specific draft of 70 kNm^{-2} is assumed. The draft force required by the rear subsoiler to till the above cross-sectional area can be approximated in this model as follows:

$$H_a = 70*A_r \text{ (kN)}$$

Thus the draft force required for soil pulverization, based on the 30% increase in unit draft, is approximated as follows:

$$H_p = 0.3 * H_a \quad \text{.....3.74.}$$

Therefore the total draft force required by the rear subsoiler can be expressed as follows:

$$H_{Tot} = H + H_p + F_{tot} \quad \text{.....3.75.}$$

Where:

H_{Tot} = Total draft force required by the rear subsoiler (kN).

H = Draft force required to fail the soil block, accelerate and slide it over the share (kN).

H_a= Draft force required by the rear subsoiler to till a cross-section area (kN).

H_p = Draft force required to pulverize the tilled soil (kN).

F_{tot} = Total frictional force acting on the sides of the rear subsoiler (1.62 kN).

It is also possible to replace H_p by 0.3H, thus 30% of the draft force is added for pulverization.

Appendix B presents a Matlab-based computer program coded to solve this model for the horizontal and vertical forces on the rear subsoiler.

CHAPTER IV

4 INSTRUMENTATION AND CALIBRATION.

4.1 Instrumentation.

Two subsoilers were mounted in tandem onto an instrumented tillage dynamometer (fig.4.1a & b). The tillage dynamometer consists of a mainframe (MF) to which a sub-frame (SF) is attached through load-cells (L_3, L_4 and L_5). The sub-frame therefore floats on the mainframe with its longitudinal movement restricted by load-cell L_6. Between the mainframe and the front vertical load cell (L_5) are well-lubricated small rollers in a dust cover. These rollers provide for a limited longitudinal movement of the sub-frame relative to the mainframe. Two parallel side braces with ball joints perpendicular to the sub-frame prevent lateral movement of the sub-frame.

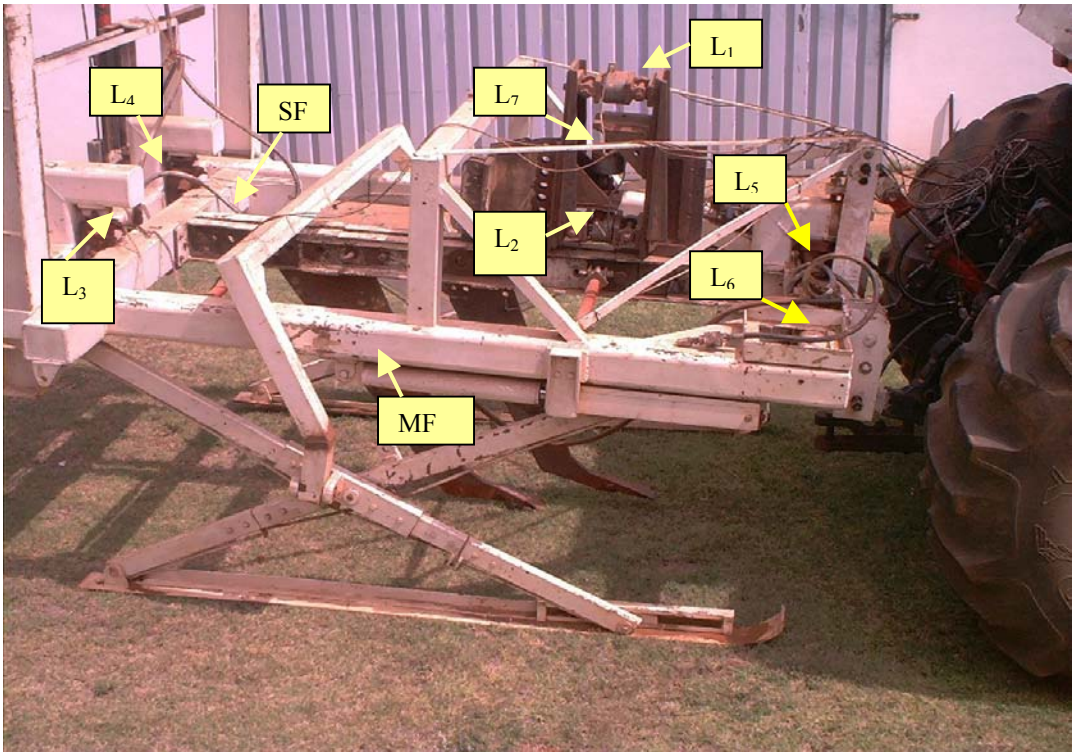

Figure 4.1a: Tillage dynamometer.

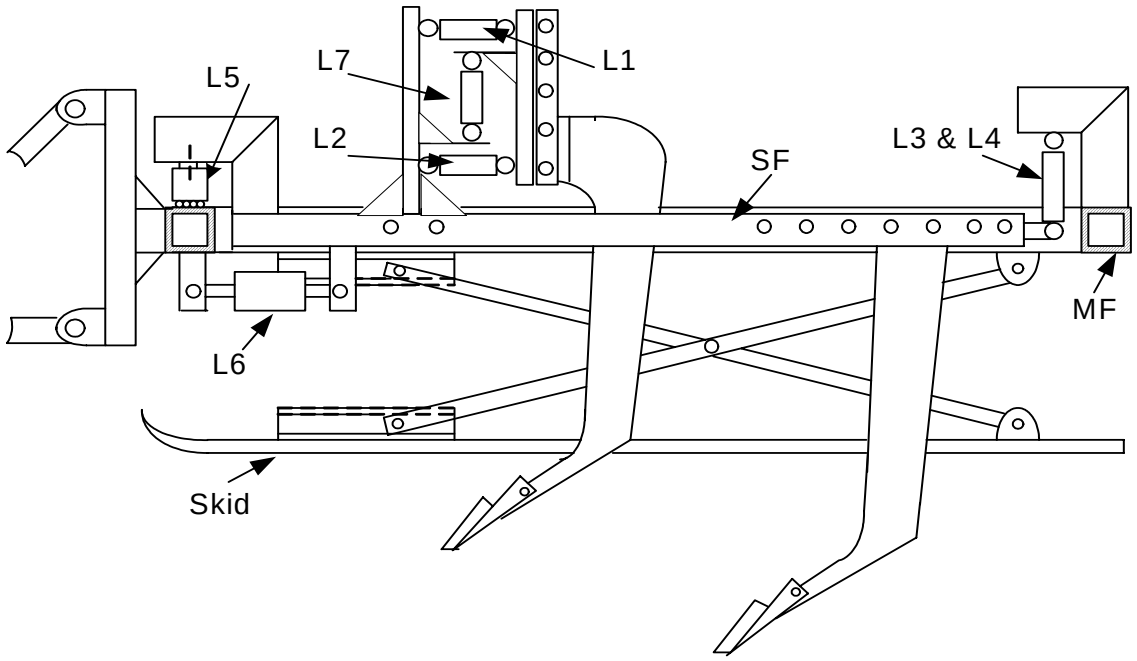

Figure 4.1b: Tillage Dynamometer.

The rear subsoiler was connected directly to the sub-frame with a provision for varying its position longitudinally. The front subsoiler is also mounted to the sub-frame through a system of load-cells (L_1, L_2 and L_7) with a provision of varying its position vertically. Load-cell L_7 is connected to the sub-frame through ball joints to protect it from possible bending moments. Load-cells L_1 and L_2 have four pivot points each allowing limited vertical movement and no side-movement.

The dynamometer is equipped with skids that slide over the ground, thus maintaining a uniform depth for both subsoilers. Further more, the skids are connected to the main frame through a hydraulically operated linkage systems, which level the entire dynamometer laterally. This is possible since each linkage system can be operated separately by shutting or opening the relevant hydraulic valves. The skids also adjust the operating depth, while the entire dynamometer is horizontally leveled through a hydraulic cylinder used as top link.

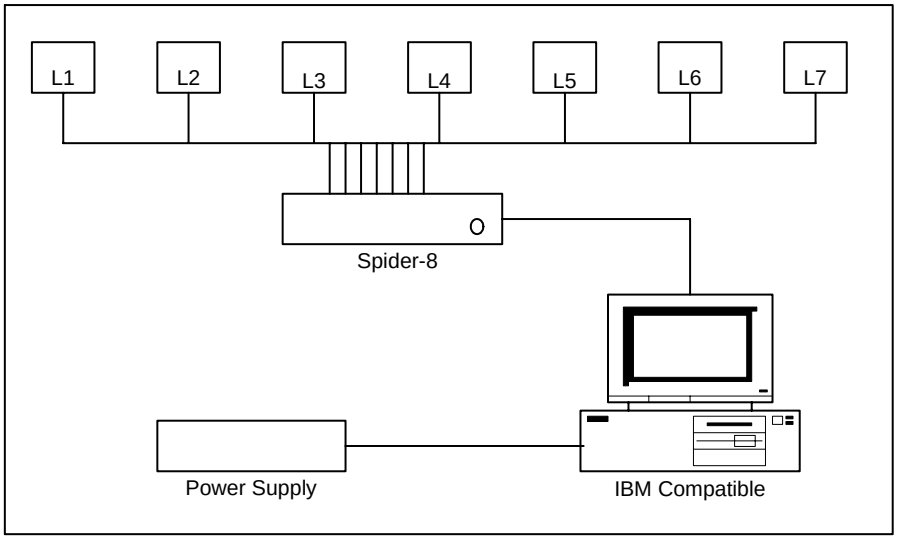

Figure 4.2: Schematic layout of the instrumentation.

During the field tests, a Spider-8 data acquisition system was installed in the tractor cabin. This system was powered by a 12V DC/220 V~, 500W inverter-power supply. All the seven load-cells were connected to this data-logger for signal filtering and amplification, which in turn was connected to a computer-processing unit (fig. 4.2). The sensitivity of all the load cells was 2mV per input volt at full load. The exerted force on each respective load-cell was determined as follows:

$F_a = F_{cal} * V_{out}$.

Where:

F_a = Applied force on the load-cell (N).

F_{cal} = Load-cell calibration factor (N/mV).

V_{out} = Output voltage signal from the data acquisition system (mV).

4.1.1 Determination of forces acting on the subsoilers.

In operation the mainframe is connected to the three-point linkage system of the tractor. The applied draft force is transferred to the sub-frame through load-cell L_6. The resulting vertical force components for both subsoilers were registered by load-cells L_3, L_4 and L_5. The draft force requirements of the front subsoiler were determined from the output signals of load-cells L_1 and L_2. The resulting vertical component was registered by load-cell L_7 (Fig.4.1).

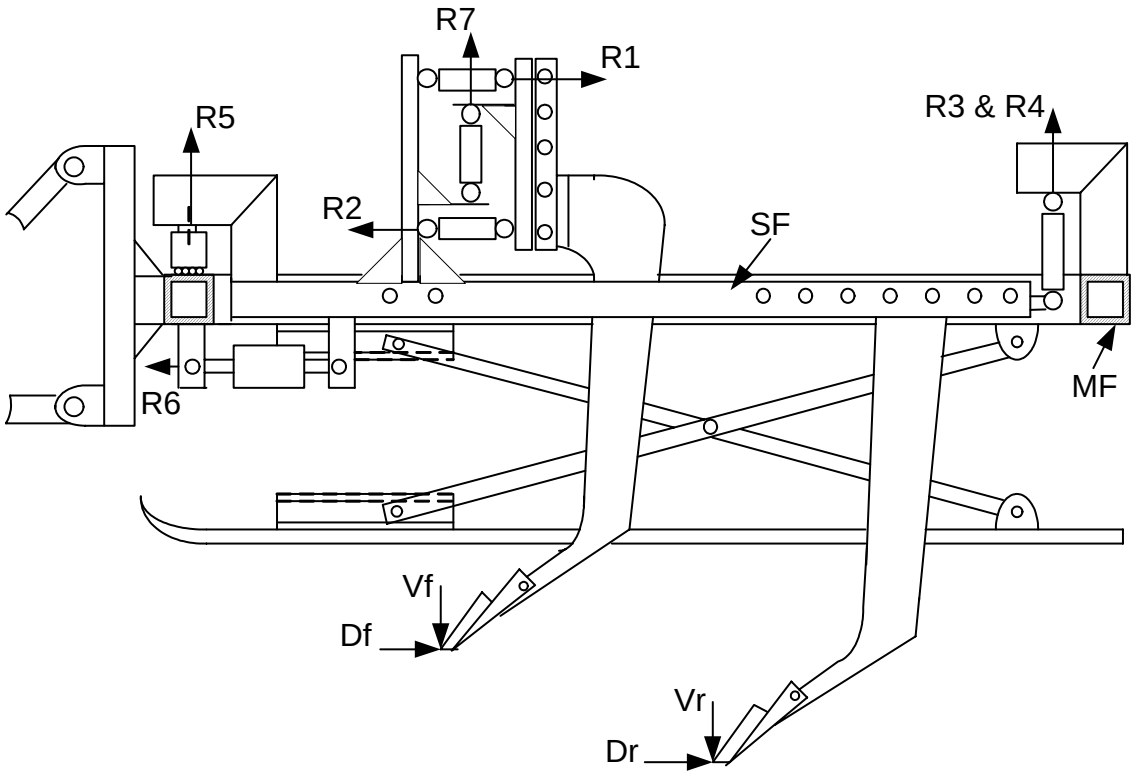

Figure 4.3: Tillage dynamometer loading in operation.

The force components acting on each subsoiler are determined from the dynamometer-equilibrium equations. Below are the dynamometer-equilibrium conditions due to the horizontal loading as shown in figure 4.3.

4.1.1.1 Mainframe.

Horizontal equilibrium is achieved when:

$$R_6 = D_f + D_r \ldots \quad \text{.....4.1.}$$

Vertical equilibrium is achieved when:

$$R_5 = V_f + V_r - (R_3 + R_4 \quad \text{.....4.2.}$$

4.1.1.2 Front subsoiler load-cell system.

Horizontal equilibrium is achieved when:

$$D_f = R_2 - R_1. \quad \text{.....4.3.}$$

Vertical equilibrium is achieved when:

$$V_f = R_7 \quad \text{.....4.4.}$$

From equations 4.1 and 4.2 draft force requirement, D_r and vertical loading, V_r of the rear subsoiler are determined as follows:

$$D_r = R_6 - D_f. \quad \text{.....4.5.}$$

$$V_r = R_5 - V_f + (R_3 + R_4). \quad \text{.....4.6.}$$

Where:

D_r = Horizontal soil force exerted on the rear subsoiler (N).

D_f = Horizontal soil force exerted on the front subsoiler (N).

V_f = Vertical soil force at the front subsoiler (N).

V_r = Vertical soil force at the rear subsoiler (N).

$R_1 \ldots R_7$ = Reactions at load-cells, L_1 to L_7 respectively (N).

Draft force, D_f and vertical load V_f at the front subsoiler, are determined from equations 4.3 and 4.4 respectively.

4.2 Calibration of the load-cells.

All the load-cells were calibrated outside the dynamometer system to determine the calibration factor of each load-cell. Each of the load-cells was suspended from a beam and vertically loaded with known dead masses. The vertical loads were increased at intervals up to about 50% of each load-cell capacity. The output signal from the

transducer was transmitted into a data-logger based processing system. The load cell output voltage was read from the computer monitor and plotted versus the corresponding applied load. The resulting output data-points were fitted with a regression line. Figure 4.4 shows such a plot for load cell L_5.

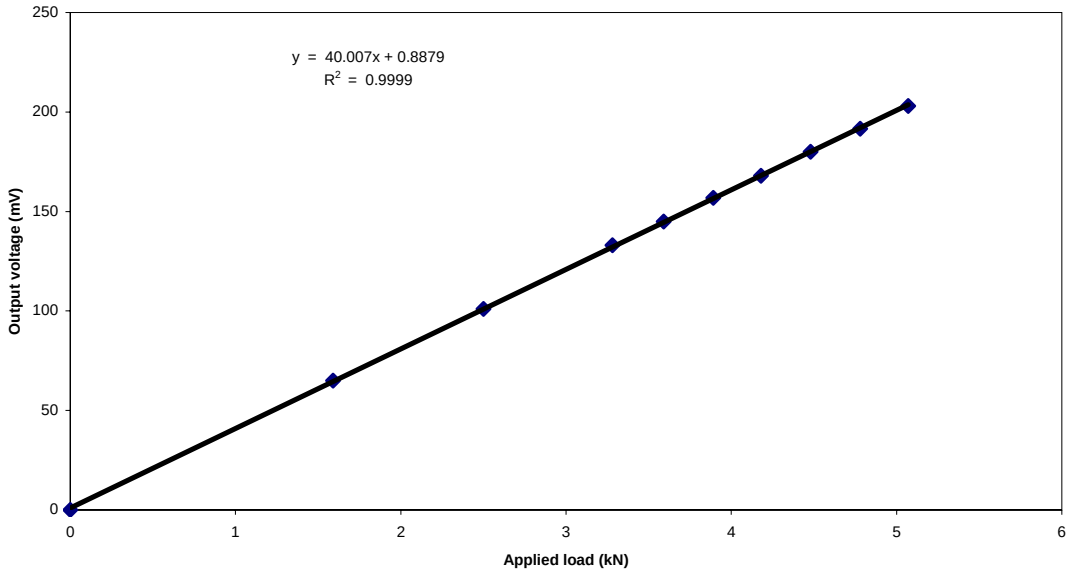

Figure 4.4: Calibration curve for load-cell, C5.

All the regression lines for the other load cells were highly linear with the coefficients of determination ranging between 0.9998 and 1. The equations of the regression lines describing the relationship between the output voltage and the applied loads were used to determine the calibration factor of each respective load cell. Table 1 presents the calibration factors for all the load cells.

Table 4.1. Load-Cell Calibration Factors.

Load Cell	Cal-Factor (N/V)
C1	25235
C2	25310
C3	5018
C4	5028
C5	24871
C6	49650
C7	25367

Cal-Factor stands for calibration factor.

4.3 Calibration of the tillage-dynamometer.

To account for possible errors due to friction within the dynamometer load-cell system, it was calibrated by loading in the horizontal and vertical planes. In the horizontal plane, it was loaded by exerting a known horizontal pull at the foot of the front subsoiler. In the vertical plane, it was loaded by putting known masses on a platform fixed to the foot of the front susbsoiler.

As it was loaded, the output voltage signals for the various load-cells were recorded. The recorded values were used in the equilibrium equations of the dynamometer, to check if the equilibrium conditions were not violated. Furthermore, recorded values were also used to establish how well each load-cell was measuring the applied force to the dynamometer and/or subsoilers.

4.3.1 Equilibrium during horizontal loading.

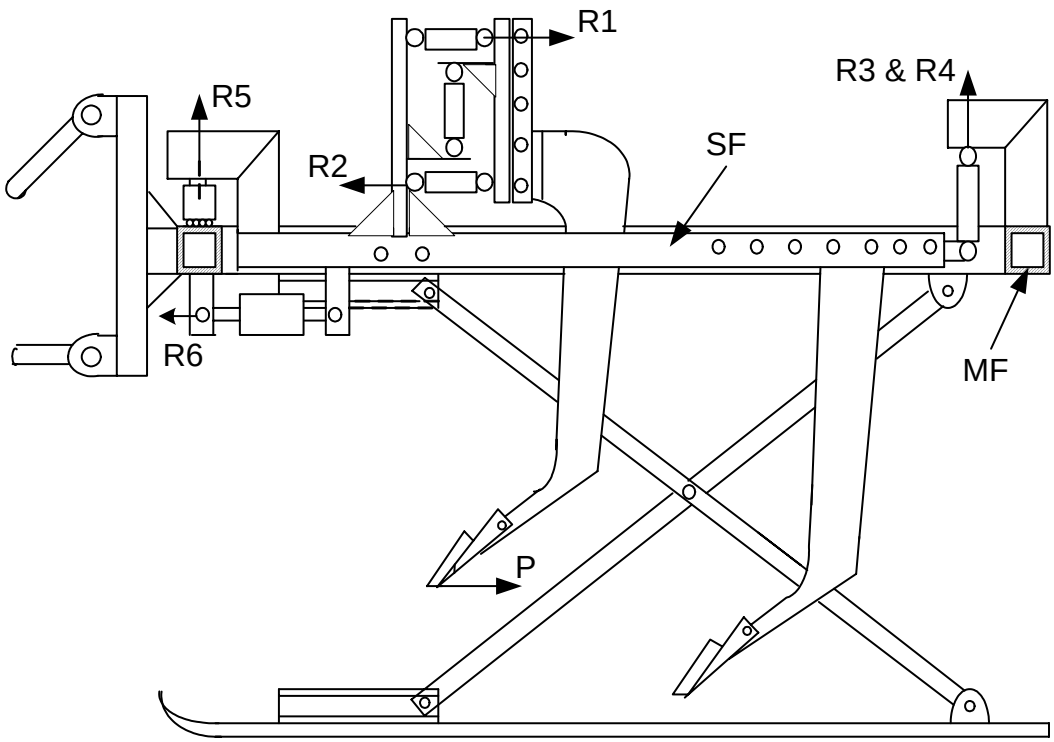

Figure 4.5: Horizontal loading of the tillage dynamometer.

This test was conducted with all the load-cells in the dynamometer system. A known pull, P was exerted on the front subsoiler as indicated in figure 4.5. It was increased in steps from zero to about 14 kN. At the same time, reactions of the load-cells due to this horizontal loading were continuously recorded.

4.3.1.1 Vertical Plane.

In the vertical plane, equilibrium of the main frame is achieved with the force P applied on the centerline under the following conditions:

$R_5 = R_3 + R_4$. ……...4.7.

$R_3 = R_4$ .....……..4.8.

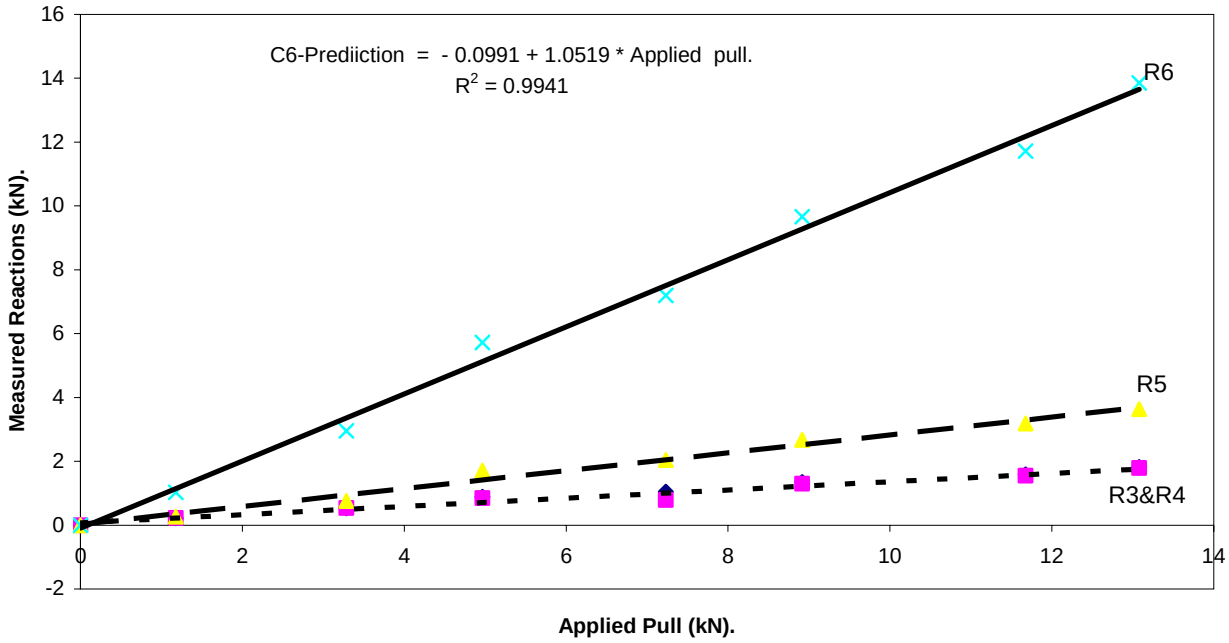

Figure 4.6: Reactions of load-cells at the mainframe due to horizontal loading.

As shown by figure 4.6, when the pull exceeded 5000 N, the measured reactions R_3, R_4 and R_5 were in agreement with equation 4.7 with an error of about 1%. This was acceptable since in field tests, the total draft for both subsoilers always exceeds 5000

Newton. Removing offset of the load-cell output voltages at zero pull eliminated the influence of the weight of subsoilers and sub-frame. There was no significant discrepancy between R_3 and R_4 hence the requirement of equation 4.8 was fulfilled. This means the loading was largely symmetrical.

4.3.1.2 Horizontal Plane.

In the horizontal plane, mainframe equilibrium is achieved when:

$$P = R_6 \quad \text{.....} \quad 4.9.$$

From figure 4.6, load-cell L_6 measured the applied pull with of 4.5% error therefore equation 4.9 was largely fulfilled. The front subsoiler-load cell system is in horizontal equilibrium when:

$$P = R_2 - R_1 \quad \text{.....} \quad 4.10.$$

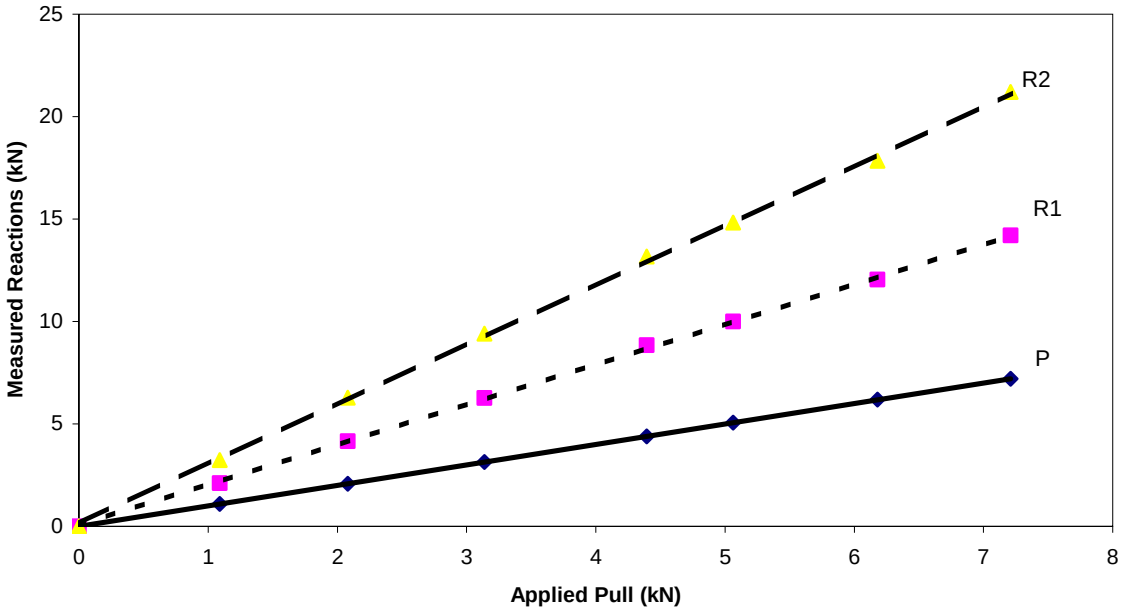

Figure 4.7: Reactions at the front shank load-cells due to horizontal loading.

From figure 4.7, measured reactions R_1 and R_2 were in agreement with equation 4.10 with an error of 4%. The vertical load cell, R_7, was insensitive to horizontal loading.

4.3.2 Equilibrium during vertical loading.

This test was conducted by recording output voltages from all the load cells as dead weights were placed on a loading platform fixed to the foot of the front subsoiler (Fig.4.8). The weight was increased in intervals from zero to about 14 kN.

4.3.2.1 Vertical Plane.

In this plane, the main frame is in equilibrium when;

$W = R_3 + R_4 + R_5$ .....4.11.

The recorded reactions followed the expression with an average error of about 3% (Fig.4.9).

The load-cell system at the front subsoiler achieve vertical equilibrium when:

$W = R_7$… .....4.12.

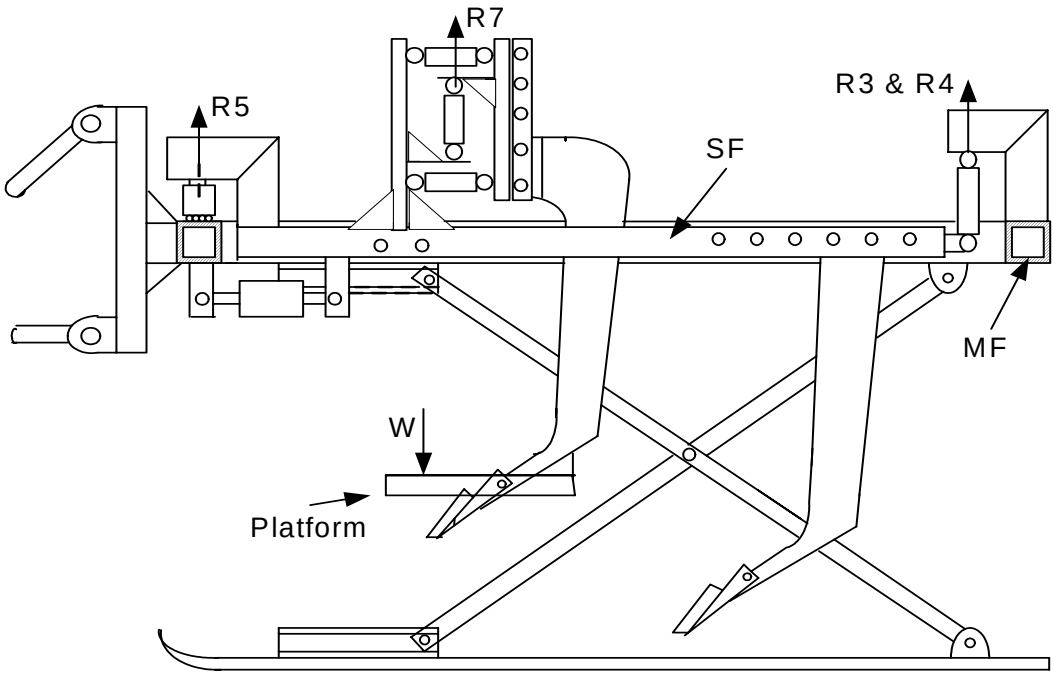

Figure 4.8: Vertical loading of the tillage dynamometer.

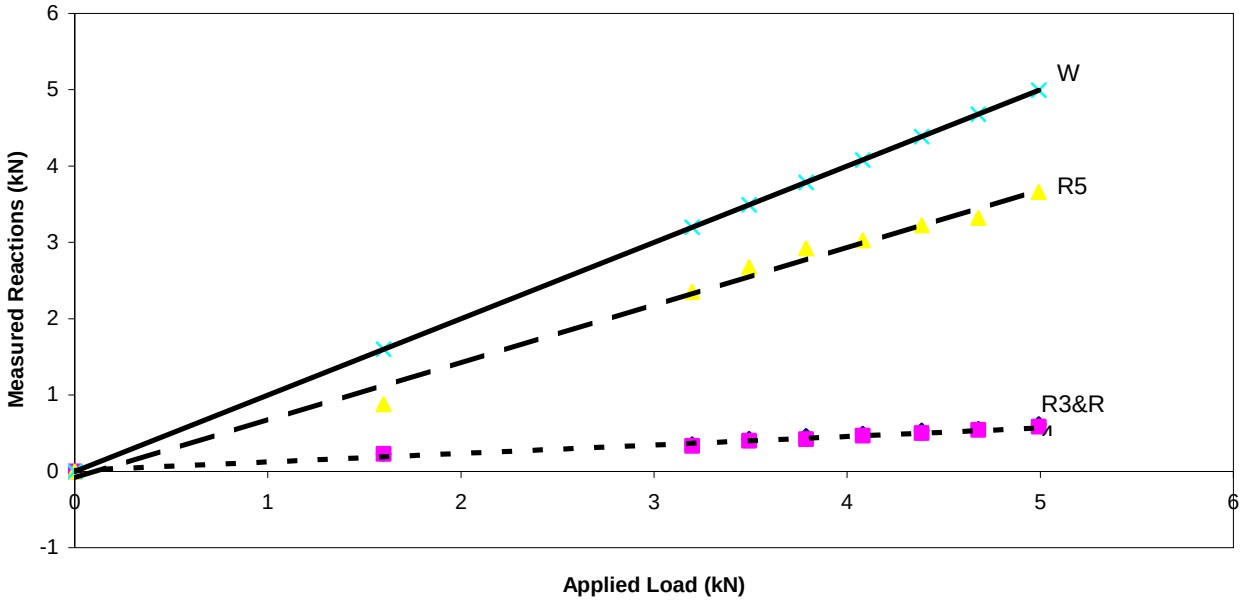

Figure 4.9: Reactions of the load-cells on the mainframe due to vertical loading.

The regression line fitted on the plot (fig.4.10), for weights versus the corresponding measured reaction values of R_7, has a slope of 0.97 and a vertical intercept of -0.065 translating into an average error of 3%.

4.3.2.2 Horizontal Plane.

The horizontal load-cell, L_6 was not sensitive to vertical loading. However the two horizontal load cells, L_1 and L_2 were sensitive to vertical loads but their values were similar with opposite signs (fig.4.10). This means therefore that the two forces eliminate each other.

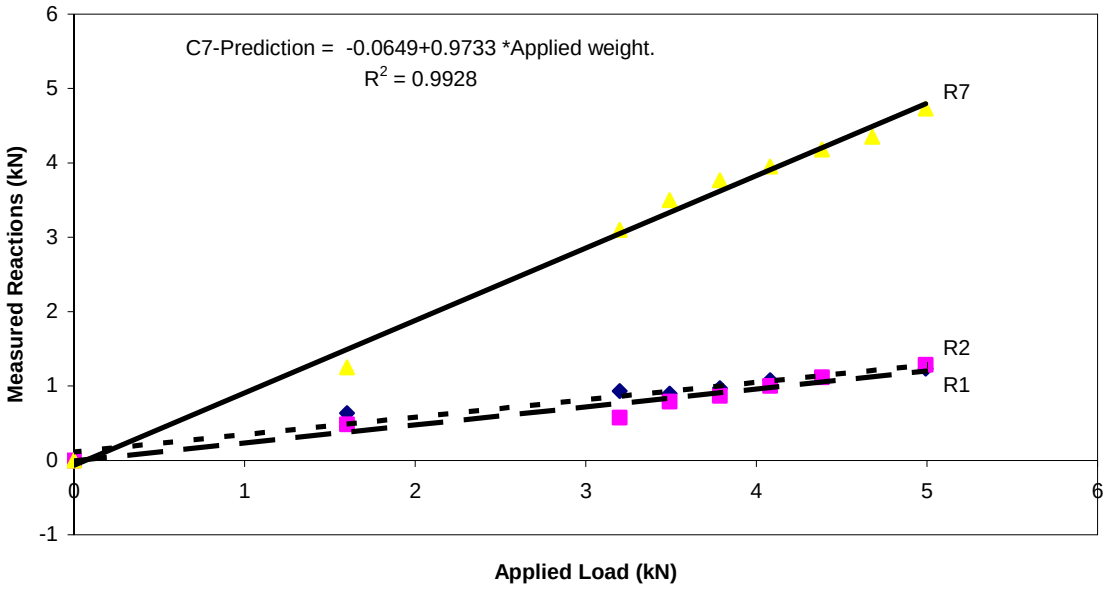

Figure 4.10: Reactions of the front shank load-cells due to vertical loading.

4.3.3 Force measurement by an extended octagonal ring transducer.

Since the forces acting on a subsoiler are in two dimensions and a moment in one dimension (fig.4.12), they can be measured by an extended octagonal ring transducer (McLaughlin, Tessier and Guilbert. 1998). An extended octagonal ring presented in figure 4.11 was therefore selected to measure the soil reacting forces on the front subsoiler in a tandem configuration. Useful data was collected with the extended octagonal ring but unfortunately it was damaged before the field tests were completed and had to be replaced by the load-cell system as discussed in previous paragraphs.

The transducer 1 was clamped on steel metal plate 2 as shown in figure 4.12 that was fixed on the sub-frame (SF) of the tillage dynamometer. The front subsoiler was then directly clamped to the transducer. Strain gauge bridge circuits in figure 4.12a and b were used to measure the vertical (V) and horizontal (H) forces acting on the subsoiler.

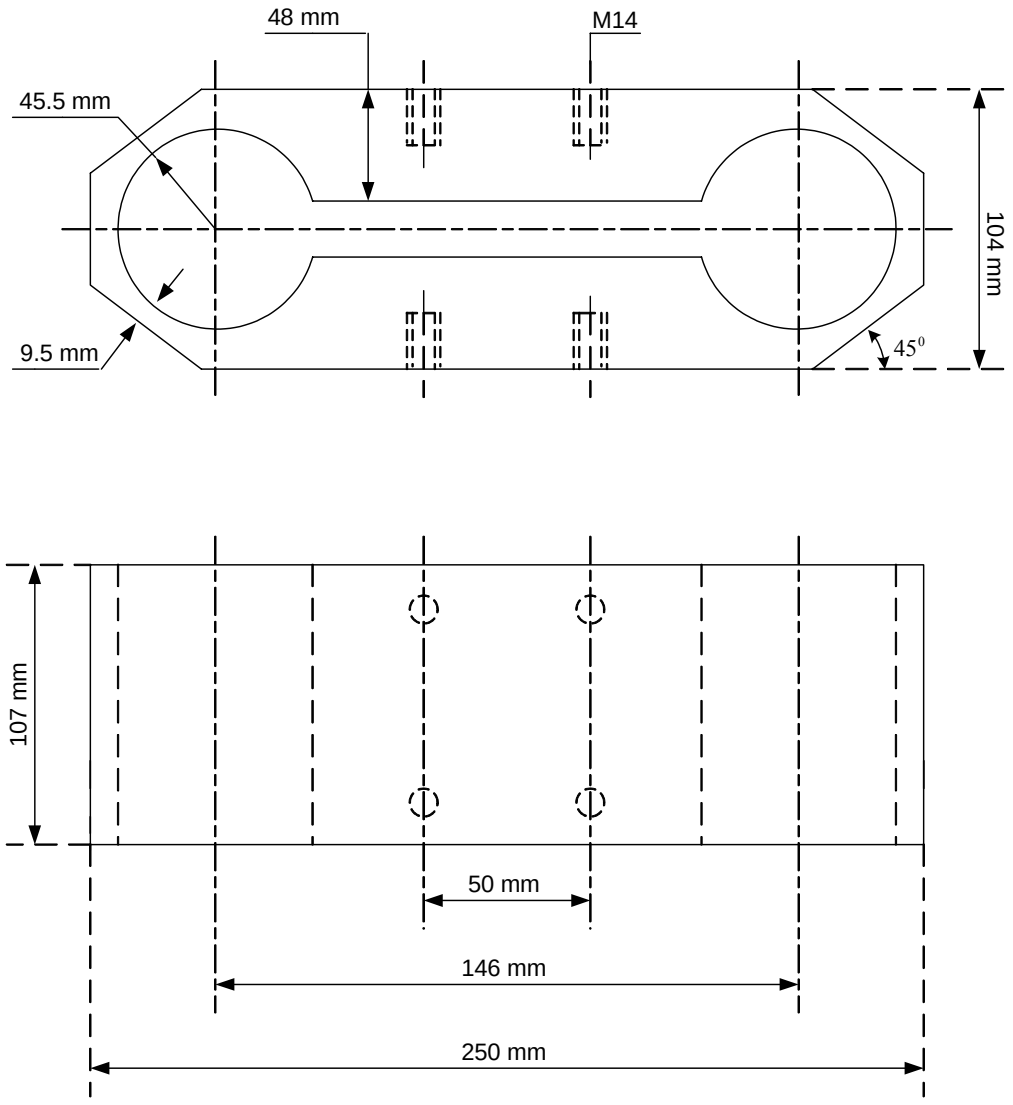

Figure 4.11: Extended octagonal ring transducer used during initial tests.

Calibration results showed a linear relationship between the applied loads and the output with the coefficient of determination equal to 0.9986 and 0.9974 for the horizontal and vertical bridges respectively (Fig. 4.13 & 4.14). The horizontal was not sensitive to vertical loading and also the vertical bridge was not sensitive to horizontal loading. Both bridges were independent of the loading positions thus moments due to forces H and V. The sensitivity of the horizontal bridge was 2.25 μ $N^{-1}V^{-1}$ while that of the vertical bridge was 3.77 μ $N^{-1}V^{-1}$. The cross sensitivity between the bridges was negligible.

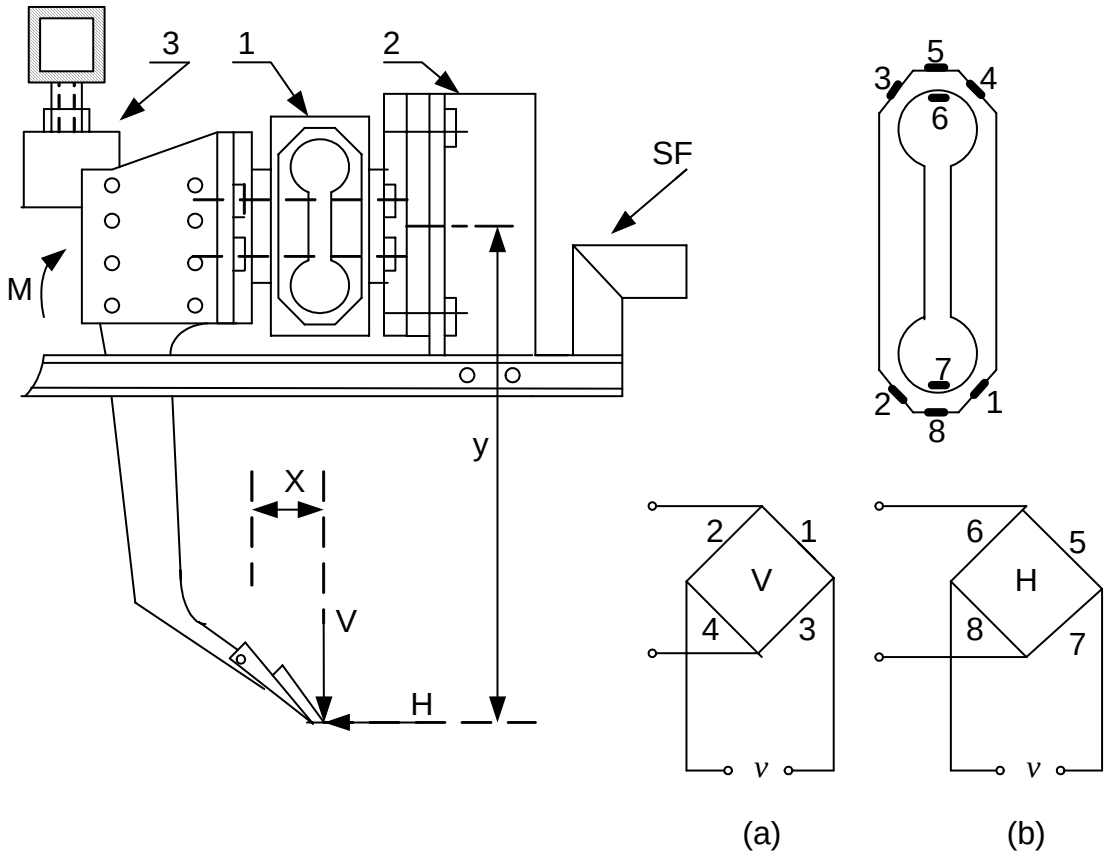

Figure 4.12: Front subsoiler clamped to the extended octagonal ring transducer.

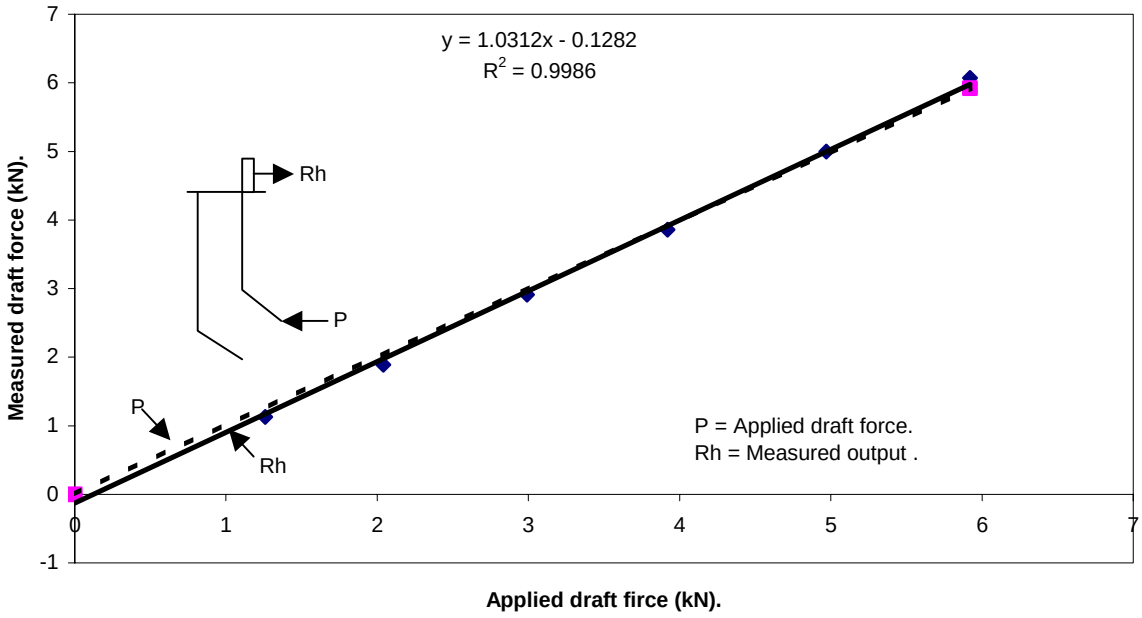

Figure 4.13: Investing how the horizontal bridge measures the draft force.

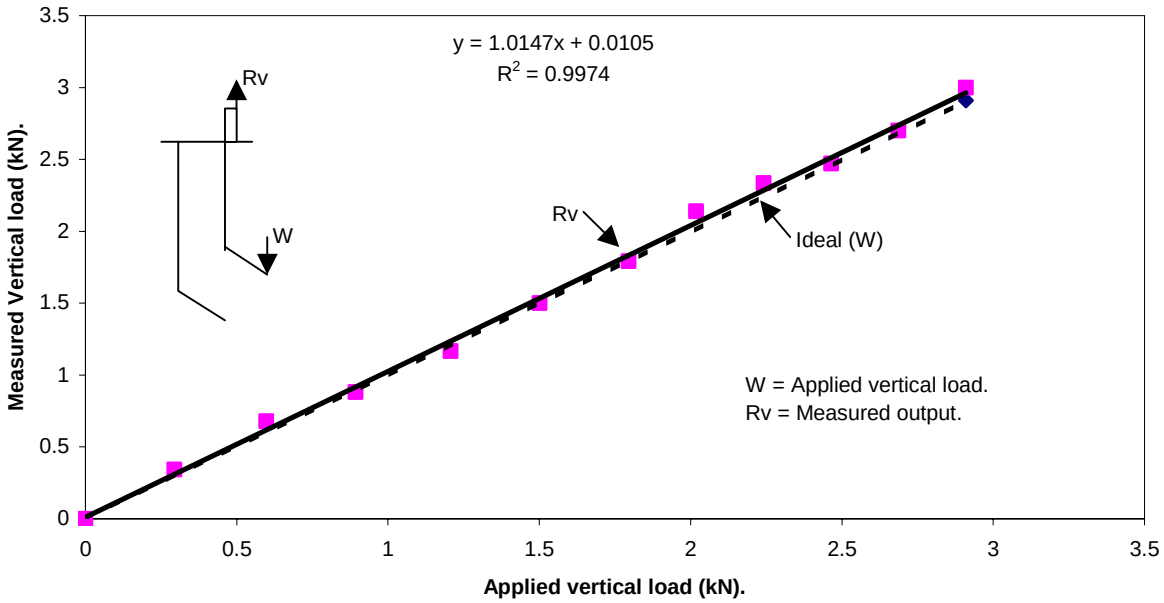

Figure 4.14: Investigating how the vertical bridge measures the vertical loading.

The maximum allowable loading of the transducer was determined as follows:

According to Godwin (1975), maximum strain for an extended octagonal ring transducer is determined by the following equation:

$$\varepsilon_{\max} = \frac{1.35kM}{Ebn^2} \quad \text{.....4.8.}$$

$$\sigma_{all} = E\varepsilon_{\max} \quad \text{.....4.9.}$$

Where:

ε_{max} = Maximum strain.

σ_{all} = Allowable stress (MPa).

E = Modulus of elasticity (MPa)

n = Ring thickness (m).

b = Width of the transducer (m).

M = Applied moment (kN.m).

2L = Distance between ring centres (m).

r = Mean radius of the ring (m).

k = L/r.

By substituting equation 4.9 into 4.8 and using the transducer dimensions in figure 4.11:

$$M = \frac{bt^2\sigma_{all}}{1.35k} = 6.71kN.m$$

The transducer was machined from a steel alloy with allowable stress of 1500 MPa and heat-treated.

From figure 4.12, the applied moment M = yH + xV = 6.71 kN.m.
Where y = 1.1 m at a maximum operating depth of the front subsoiler.
Assuming xV accounts for 25% of the applied moment M then the maximum horizontal loading, H = 4.6 kN.

The maximum horizontal loading was close to the anticipated loading during the field operations. A mechanical safety mechanism 3 (fig. 4.12) was therefore put in place to protect the transducer from possible damage. However it was damaged when the subsoiler hit an obstacle in the ground. A two-dimensional force transducer system, as discussed above, was designed and assembled to replace the damaged extended octagonal ring transducer.

CHAPTER V.

5 RESEARCH METHODOLOGY.

For proper prosecution of this research project, both theoretical as well as field experimental work have been undertaken. The theoretical part included the development of the mathematical force model for predicting the draft force requirement of the rear subsoiler, as well as coding a Matlab-based computer program (Appendix B) for solving the proposed mathematical model. At the same time, the field experiment portion of the study, involved the collection of data for verification of the proposed mathematical model and determining the parameters for optimizing energy input.

All the experimental work was executed under field conditions at the Experimental Farm, University of Pretoria. Hay had been harvested from the field where the tests were conducted. In order to achieve realistic experimental conditions, the tests were conducted during the dry winter season. That is the period when uncontrollable influences such as moisture regime could be kept at desired levels by irrigating the test plots and allows it to get to the correct soil water content.

5.1 Experimental design.

The experimental field was divided into treatment areas. Each treatment area was treated as completely randomized with four replications. The size of each treatment area was sufficient to ensure that disturbed soil resulting from a previous run would not affect a current test. All the runs were conducted at the same engine speed and transmission ratio while the draft and vertical forces were recorded continuously. The depth of the rear subsoiler, for all the tests was held constant at 600 mm. The operating depth for the front subsoiler was varied at three different levels. At each depth setting, the spacing “x” (fig.5.1) was varied at four different positions (Table 5.1).

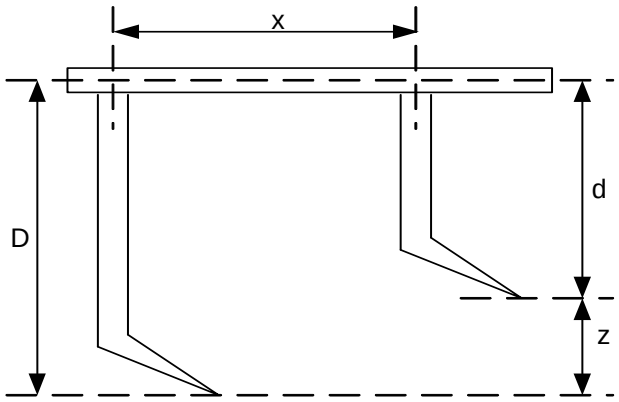

Figure 5.1: Subsoiler Setting.

The variables were:

- Spacing, x.
- Front subsoiler operating depth, d.

The response variables were the horizontal and vertical force components acting on an individual subsoiler and cross sectional area of the three-dimensional failure profiles.

Table 5.1: Subsoiler settings during the field tests.

Position	x (mm)	d (mm)	z (mm)
Pos11	300	410	190
Pos12	420	410	190
Pos13	540	410	190
Pos14	790	410	190
Pos21	300	460	140
Pos22	420	460	140
Pos23	540	460	140
Pos24	790	460	140
Pos31	300	510	90
Pos32	420	510	90
Pos33	540	510	90
Pos34	790	510	90

D = 600 mm for all positions.

Table 5.1 above, shows the front subsoiler depth-spacing combinations randomly tested with four replicates in different treatment areas.

5.2 Determination of soil properties.

a). Soil Classification.

Soil samples were randomly collected from the test field for classification. The sieve analysis method was used to classify the soil as outlined by Bardet (1997). It was classified as sandy clay-loam containing 24% clay, 10% silt and 66% sand.

b). Soil Unit Weight.

Different spots were randomly selected in the test field. The soil was dug at each spot and its mass was determined. The created hole was lined with a plastic film and filled with a known volume of water. Then the soil density and unit-weight were determined by calculating the ratio of the mass of the removed soil to its volume. This test was repeated in all the selected spots and the average unit weight was found to be 19890 N/m^3 at soil water content of 9.15% (db).

c). Soil Water Content.

At least five soil samples were collected from each treatment area for checking the uniformity of the soil water content. Soil water content was determined using the standard method outlined by Bardet (1997). A soil water content-coefficient of variation of at least 10% from the mean value of 9.15% dry basis (8.25% - 10.10%) was targeted. In cases where the soil water content was found not to fall within this range, the collected data was not used when evaluating the performance of the mathematical models. However it was used in expressing the maximum width of the failed side circular wedge as a function of soil water content.

d). Soil shear strength.

For the measurement of soil shear strength, a torsional shearing device was used. This device measured cohesion, adhesion, internal soil friction angle and soil-metal friction angle. It was equipped with one load-cell that measured the applied normal force and one torque arm with strain gauges to measure the applied torque. It was mounted to a tractor with a Spider8-data acquisition system on board to which the two load cells were connected. A shearing ring plate with grousers was attached to the head of the device to

measure cohesion and soil internal friction angle. A smooth steel plate without grousers was used to measure adhesion and soil-metal friction angle.

Using the tractor hydraulic system, a normal force was applied to press the plate on a leveled soil surface. With the help of a special hydraulic circuit, the normal force could be kept constant during shearing. At a constant normal force, torque was applied to rotate the plate and cause soil shear-failure by a separate hydraulic power system. This test was repeated several times varying the normal force at close spots.

The point where the torque signal started decreasing from its maximum value indicated the torque at which soil failure took place. Using equation 5.1, the maximum shear stress was calculated from the applied torque-value at soil failure.

$$\tau_{max} = \frac{3T}{2\pi\left(R_1^3 - R_2^3\right)} \quad \text{.....5.1.}$$

Where:

τ_{max} = Maximum shear stress at soil failure (kPa).

T = Applied torque (kNm)

R_1= Outer radius of the ring plate (m).

R_2 = Inner radius of the ring plate (m).

The inner and outer radii for the ring plate without grousers were 0.065 and 0.15 m respectively. For the ring plate with grousers, the inner and outer radii were 0.065 and 0.147 m respectively.

The normal stress corresponding to torque at soil-failure, was determined by dividing the applied normal force with the effective area of the respective ring plate. The maximum shear stress was then plotted against normal stress. The slopes of the obtained graphs, define either soil internal friction angle or soil-metal friction angle while cohesion or adhesion is defined by the vertical intercepts as represented by Coulomb's equation.

An example of the models describing the relationship between the maximum soil-metal frictional stress and normal stress in figure 5.2a and maximum shear and normal stresses are presented in figures 5.2b

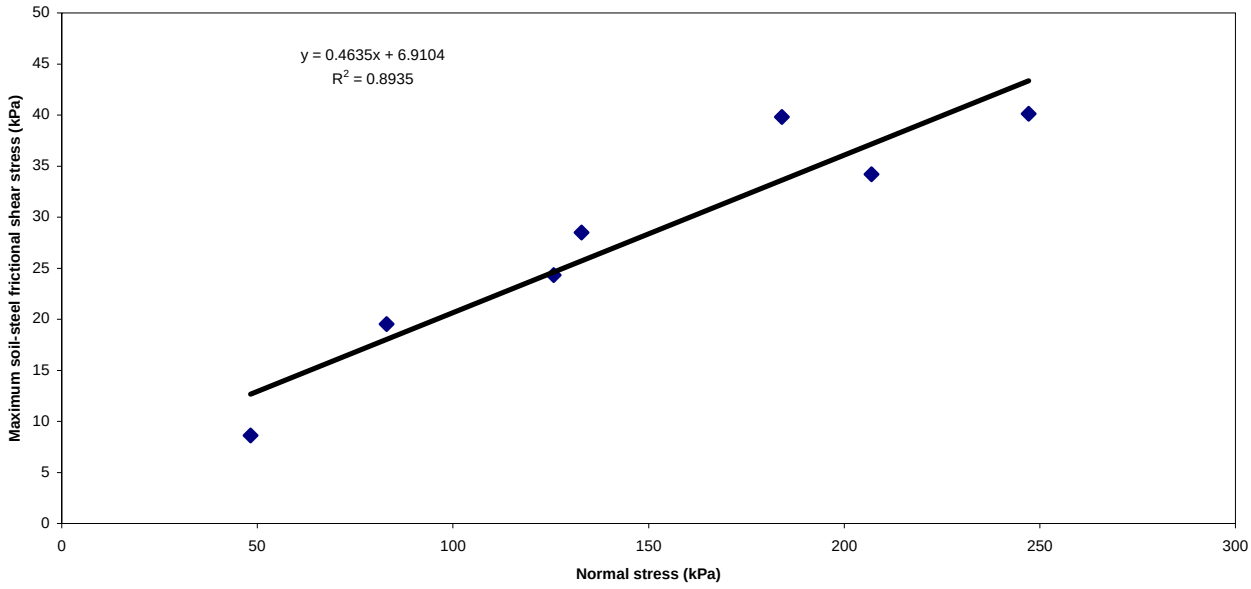

Figure 5.2a: Maximum soil-steel frictional and normal stress relationship at metal soil failure plain.

From the model of figure 5.2a the soil-steel frictional characteristics at the interface were determined as follows:

a). Soil-tool interface friction angle and adhesion.

$\tau = 0.4635\sigma_n + 6.9104$……5.2.

Where:

τ = Maximum soil-steel frictional stress at failure (kPa).

σ_n = Normal stress (kPa).

Thus:

- Soil-tool friction angle, $\delta = \tan^{-1}(0.4635) = 24.86^0$
- Adhesion coefficient, $c_a = 6.9$ kPa.

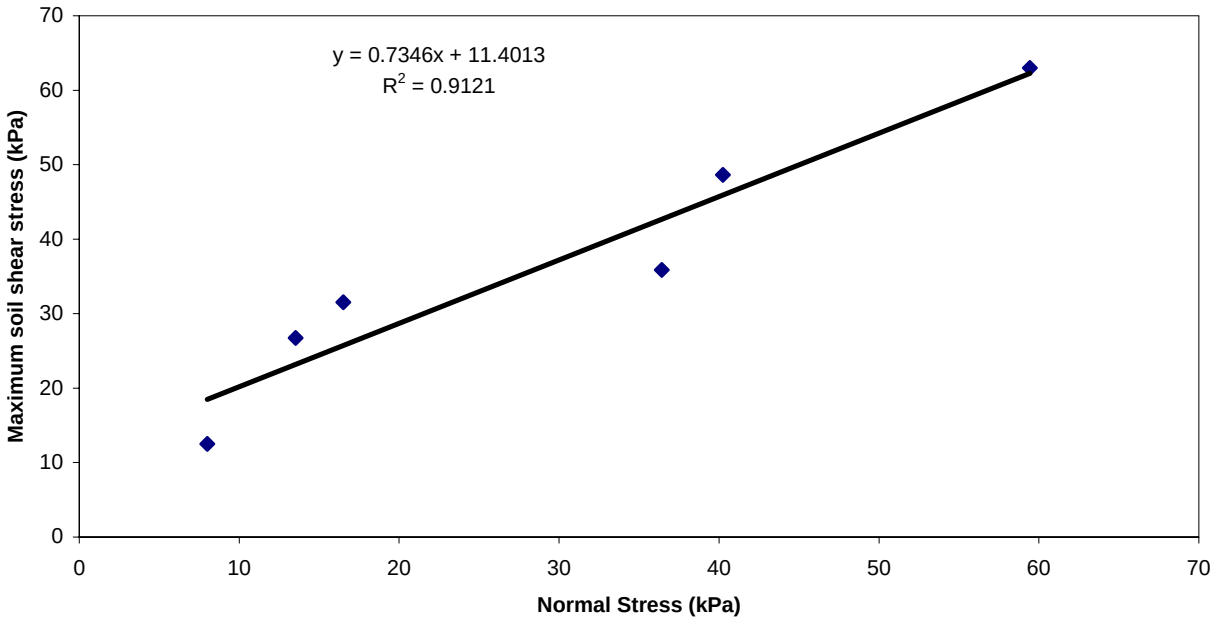

Figure 5.2b: Maximum shear and normal stress relationship at soil to soil failure plane.

From the model of figure 5.2b the soil-shear characteristics were determined as follows:

b). Soil internal friction angle and cohesion.

$\tau = 0.7346\sigma_n + 11.4013$……..5.3.

Thus:

- Soil internal friction angle, $\phi = \tan^{-1}(0.7346) = 36.3^0$.
- Cohesion coefficient, $c_c = 11.4$ kPa.

Table 5.2: Characteristics of the soil in the experimental field.

Characteristic.	**Value.**
Soil classification	Sandy clay-loam
Unit weight	19890 N/m^3 at 9.15% (db)
Soil-metal friction angle	24.86^0
Soil internal friction angle.	36.3^0
Cohesion coefficient	11.4 kPa
Adhesion coefficient	7 kPa
Soil water content	9.15% (db)

5.3 Data collection.

5.3.1 Verification of the proposed mathematical model.

Before tests were conducted in each treatment area, at least five-cone index measurements were taken to quantify soil strength. The aim was to ensure that the soil strength was relatively uniform in all the treatment areas. Soil samples were also collected for determining its unit weight and soil water content. Determination of soil water content was necessary for ascertaining its uniformity. Soil shear tests were also conducted in each treatment area to determine the relevant soil/soil and soil/tool characteristics.

At the beginning of a run, the subsoilers were engaged into the ground to the required depth and the dynamometer was properly leveled in both lateral and horizontal planes by the hydraulic system. At predetermined engine speed of 1200 rpm and gear transmission ratio (gear one-low) the tractor was driven towards an already prepared area at the end of the test ground. An area was cleared of surface cover at the end of the treatment area for measuring both the projected area of the failed soil profile and its volume for each run. During the run, travel speed, draft and vertical force components were continuously measured.

5.3.2 Development of the soil-failure profiles.

At first a computer-penetrometer technique was used to measure the three-dimensional failed-profile. However this technique was abandoned because it was found to be very time consuming. A faster manual method was therefore used. The two methods are discussed below:

a). The computer-penetrometer method.

A penetrometer-system capable of measuring soil penetration resistance at varying depth was constructed and assembled at the Department of Civil and Biosystems Engineering, University of Pretoria. This system is mounted at the rear of the tillage dynamometer (Fig.5.3).

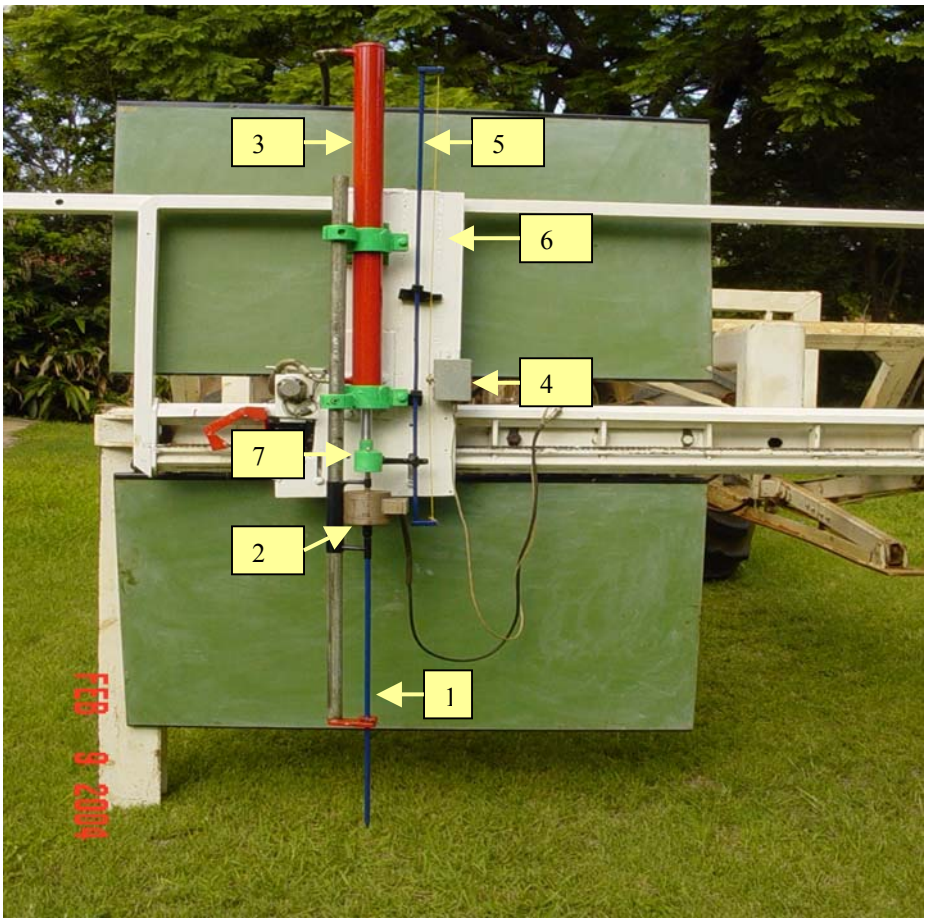

Figure 5.3: The penetrometer system mounted on the tillage dynamometer.

The penetrometer-system consists of the following components:

- A 500 kg capacity load-cell (2) in which a stainless steel penetrometer rod (1) is threaded. The penetrometer-cone has a 30^0 included angle with a maximum cross-sectional area of 1.13 cm^2.
- A hydraulic cylinder (3) onto which the load-cell is attached through a metal block (7) with a safety device.
- A potentiometer (4) fitted with a pulley and a string attached to a metal bar (5). The metal bar is fixed to the cylinder rod. The sting runs several turns around the pulley and as the cylinder rod extends, it is pulled and drives the pulley, which in turn drives the potentiometer wiper. The stroke of the cylinder rod and

therefore the displacement of the penetrometer rod into the ground can be determined from the variation of the potentiometer-voltage output.

The above items are bolted on a steel frame (6) with teflon rollers. This frame is driven at 50 mm grid intervals across the dynamometer frame by a 12 Volt electric wiper motor and a gearbox, operated from the tractor cabin. As the penetrometer rod is pushed into the ground by the hydraulic cylinder, the voltage output signals of the potentiometer and the load-cell are continuously recorded by the data acquisition system. The potentiometer output signal determines the displacement of the penetrometer rod while that of the load-cell determines the soil-penetration resistance encountered by the penetrometer rod. The typical computer voltage output signals are shown in figure 5.4. At point A penetration started and ended at point B. From point B to C, the penetrometer was stationary and withdrawal started at point C (negative force) and ended at D.

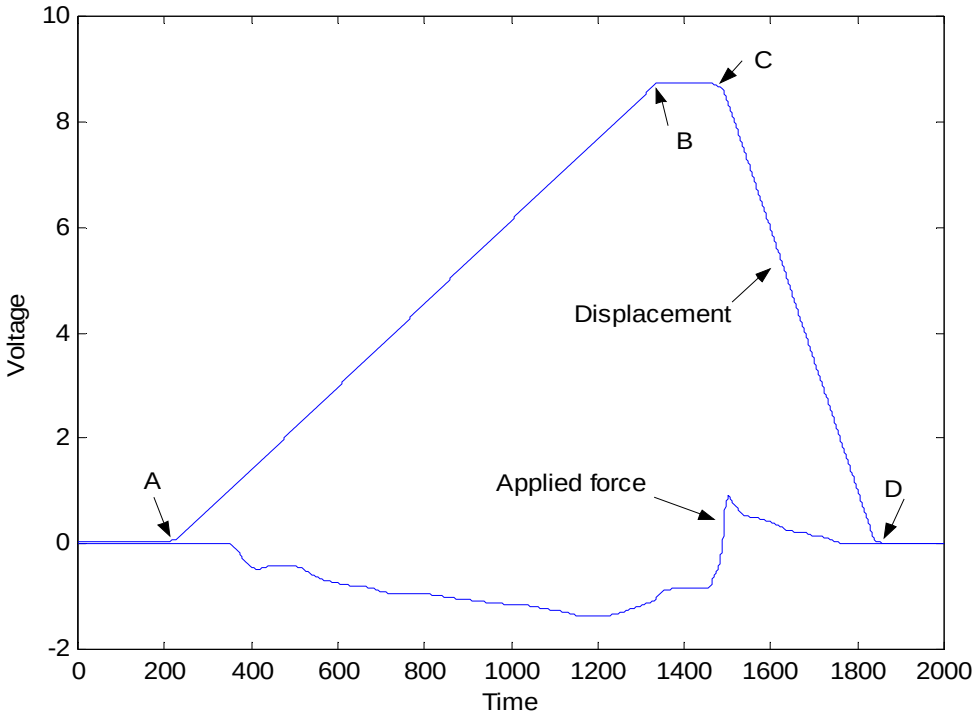

Figure 5.4: Voltage output signals of the penetrometer-displacement and applied force.

Soil-penetration resistance at varying depth was randomly measured before disturbing the soil, then it was again measured on a 50 mm grid after being disturbed. A Matlab-based computer program in Appendix C was coded to use the collected data to map a three-dimensional failed soil-profile.

The computer program was able to map the profile by comparing data collected in undisturbed soil with that collected after its disturbance. If the penetration value was found to be less, it meant that at that particular position the soil was disturbed and the program displayed so. When the program indicated 'undisturbed' repeatedly for a predetermined specified number of times for a specific displacement/depth, it meant that the border of the soil-failed profile was passed. Thus the first displayed depth with a higher penetration value was therefore recorded as the actual depth of the profile at that point. The program displayed so and indicated the actual depth. In case the program maintained 'undisturbed' for a displacement less than predetermined number of recordings then that was regarded as an encounter of a soil clod.

a). The Manual method.

At the end of each run, the tractor was stopped in an already cleared area, and then reversed and the subsoilers disengaged. The pulverized soil was manually removed. A pin-profile meter (Fig.5.5) was used to measure the exposed undisturbed soil profile. This meter consists of equally spaced pins that are lowered onto the soil surface of the exposed profile until contact was made. Pin relative elevations were measured. This was repeated at uniform longitudinal intervals until the entire profile was covered. The measured pin elevations were used in a Matlab-based computer program (Appendix D) to determine both the cross-section area of the specific profile and the total volume of the soil disturbed by the two subsoilers.

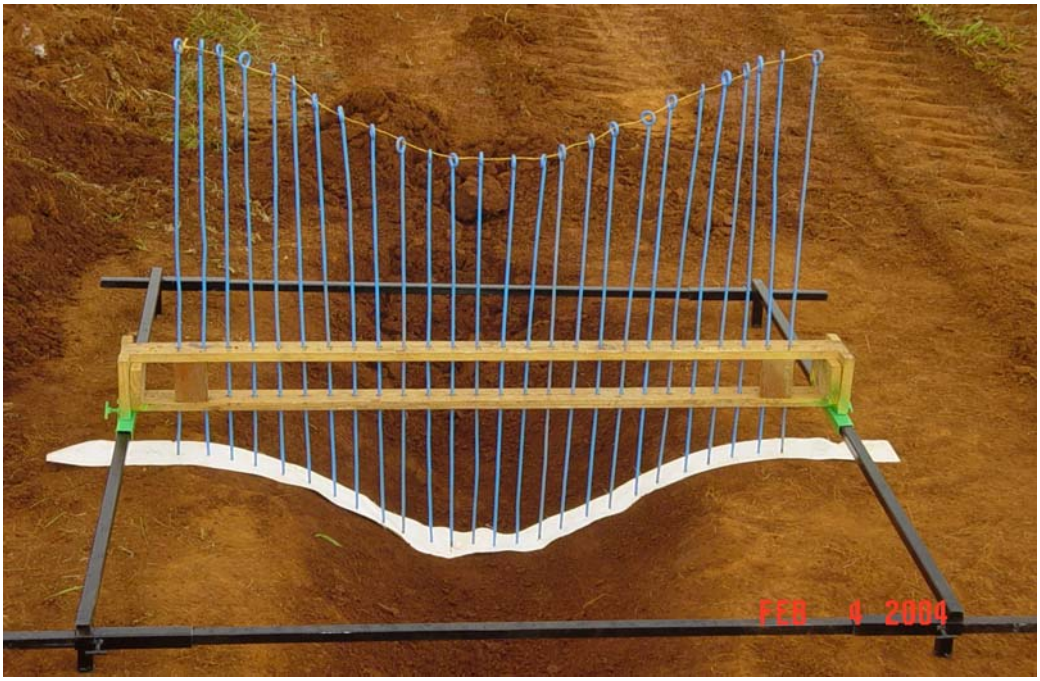

Figure 5.5: The pin-profile meter.

CHAPTER VI.

6 RESULTS AND DISCUSSION.

6.1 Statistical analyses

The SigmaStat-software was used to conduct the statistical analyses. The correlation method was used for the establishment of the relationships between various variables. Computing the Pearson correlation coefficient did this. After the establishment of the existence of a relationship then its significance was determined by conducting one of the following hypothesis tests:

Ho: $\beta_0 = \beta_1 = 0$

H1: $\beta_1 = 0$ and/or $\beta_0 \neq 0$

Or

Ho: $\beta_0 = \beta_1 = 0$

H1: at least on of $\beta i \neq 0$

Where: I = 1,2.

Using SigmaStat, regression analysis was performed to describe the relationship between the respective variables and also to determine the confidence interval of the fitted curves.

6.2 Soil-failure profiles.

The three-dimensional soil-failure profiles developed using the manual and computer-penetrometer methods are presented in figures 6.1 and 6.7 respectively. The shape of the manually measured profile is shown in figure 6.1 and its depth is equal to the tool operating depth while its bottom width is approximately equal to the width of the tool as indicated in figure 6.1a.

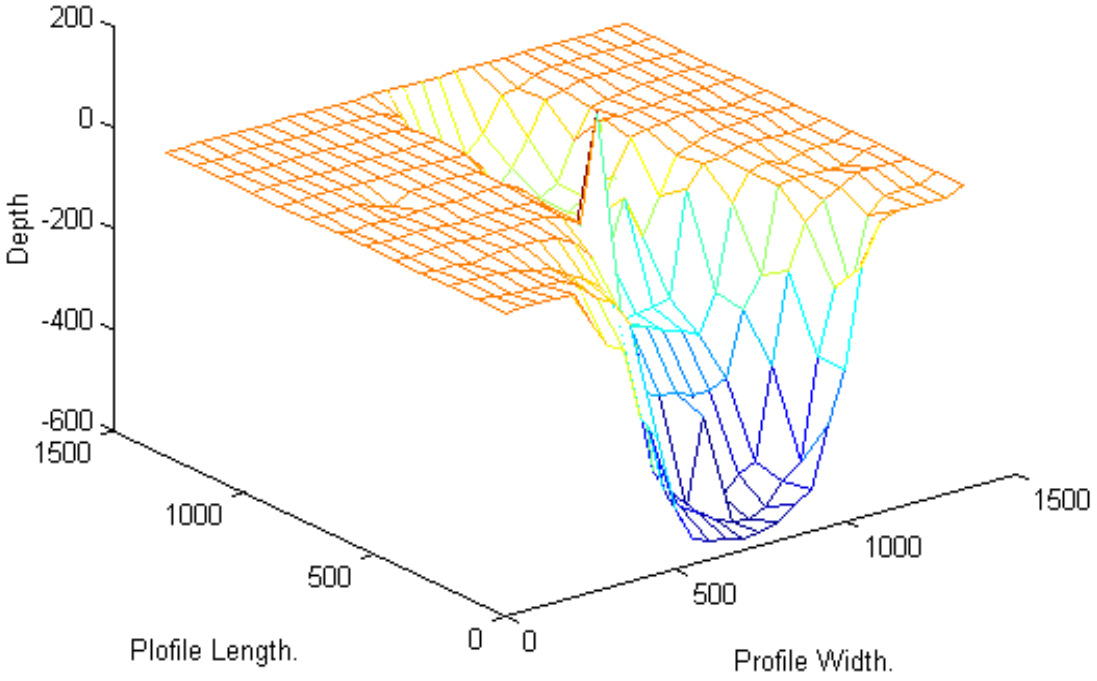

Figure 6.1: Pin-profile meter measured profile.

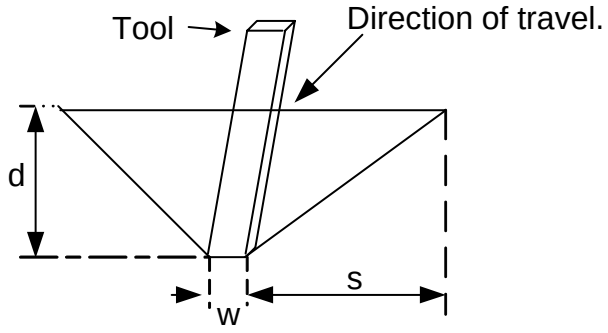

Figure 6.1a: Manually measured shape of failed cross-section area.

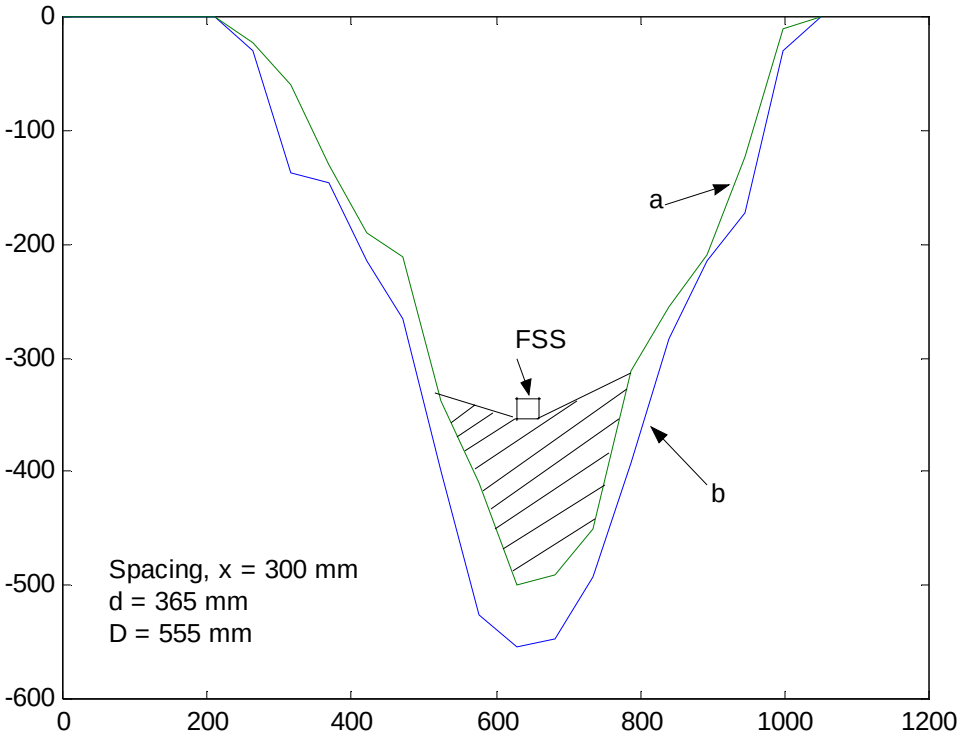

Figure 6.2a: Measured cross-section areas of failed soil-profile at the FSS and RSS. (x = 300 mm).

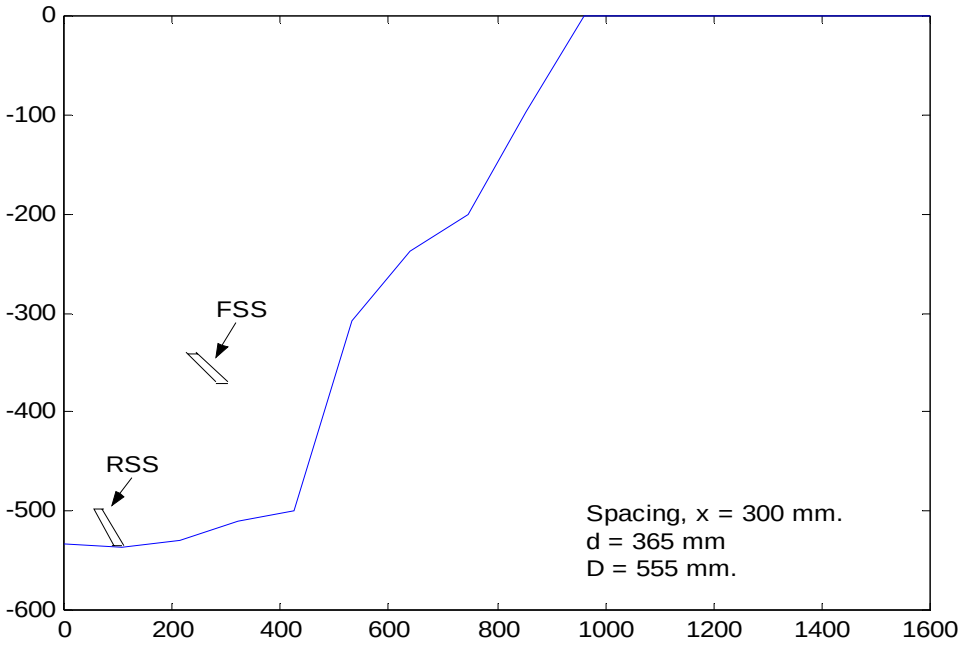

Figure 6.2b: Measured longitudinal section of the failed-profile by the two subsoilers (x = 300 mm).

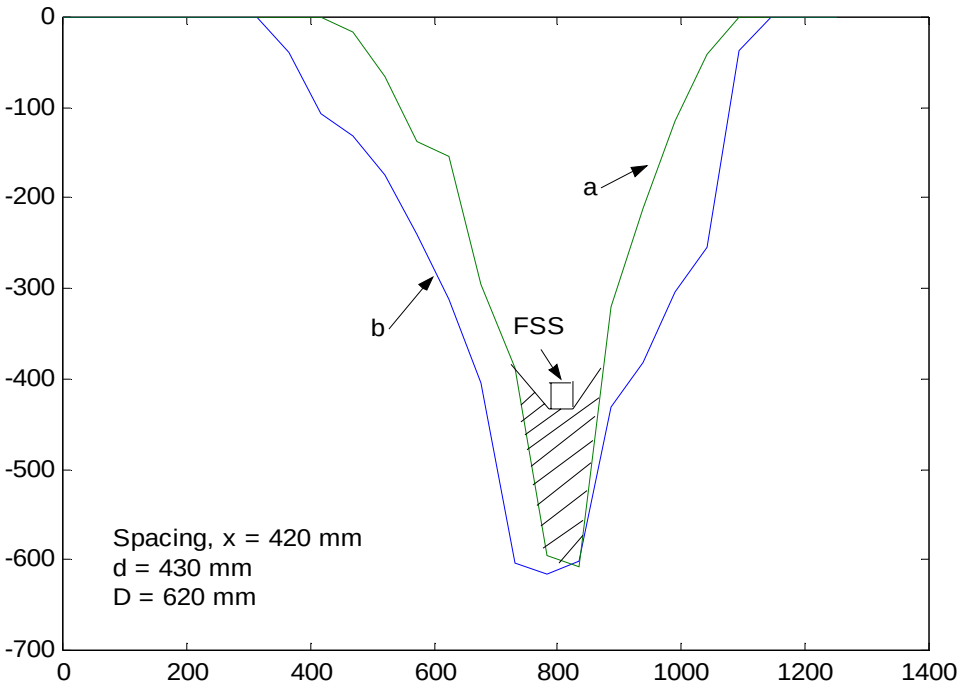

Figure 6.3a: Measured cross-section areas of failed soil-profile at FSS and RSS. (x = 420 mm).

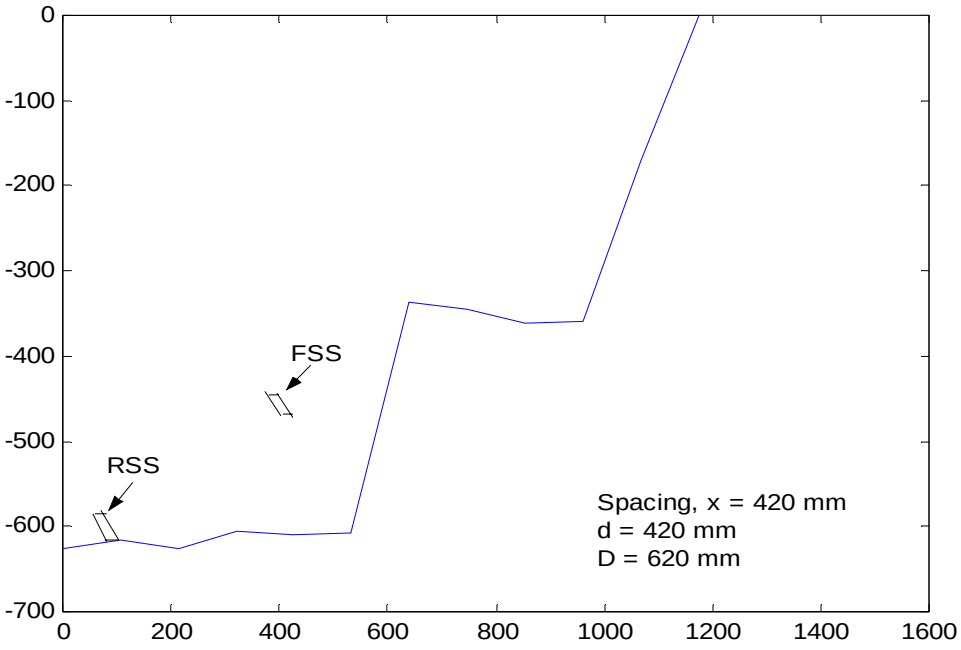

Figure 6.3b: Measured longitudinal section of the failed-profile by the two subsoilers (x = 420 mm).

When the two subsoilers are spaced close to each other, the rear subsoiler influences the size of the maximum cross-sectional area of the soil-profile failed at the longitudinal position of the front subsoiler. Figures 6.2a and 6.3a present the measured maximum cross-sectional areas of the failed soil-profiles at the front (FSS) and rear subsoilers (RSS) at a spacing of 300 and 420 mm respectively. The longitudinal sections of the failed soil-profiles at the same spacing and operating depth are given in figures 6.2b and 6.3b respectively. In both cases the positions of the front subsoilers are indicated and the depths of the failure-surfaces (a) due to the action of the FSS are almost equal to the depth of the failure-surfaces (b) of the rear subsoiler. This is due to the subsoilers being spaced in such way that they are longitudinally and vertically close, resulting in the rear subsoiler doing most of the tilling. The shaded portion of the failure-surfaces (a) below the FSS, is disturbed by the rear subsoiler. Possibly also by the spiral failure pattern.

From figures 6.2b and 6.3b, it is clear that the profiles failed by the front subsoiler are within those failed by the rear subsoiler. This means therefore that at the above spacings the soil failed, accelerated and lifted by the front subsoiler does not settle before being re-accelerated by the rear subsoiler.

Figures 6.4a and 6.5a present maximum failed cross-sectional areas at the front and rear subsoilers for a spacing of 540 and 790 mm respectively. The failed longitudinal sections at the same spacing and operating depth are presented in figures 6.4b and 6.5b respectively.

In this case the subsoilers were spaced far enough to allow the front subsoiler to till with no significant influence from the rear subsoiler. The depth of each failed cross-sectional area was therefore equal to the operating depth of the respective subsoiler. From the longitudinal sections, the soil-profiles failed by the two subsoilers, did not overlap in time. This means that the soil failed, accelerated and lifted by the front subsoiler, probably settled behind this subsoiler before being re-accelerated by the rear subsoiler.

At different operating depths of the front subsoiler, similar soil-failure profiles were recorded and they presented in appendix F.

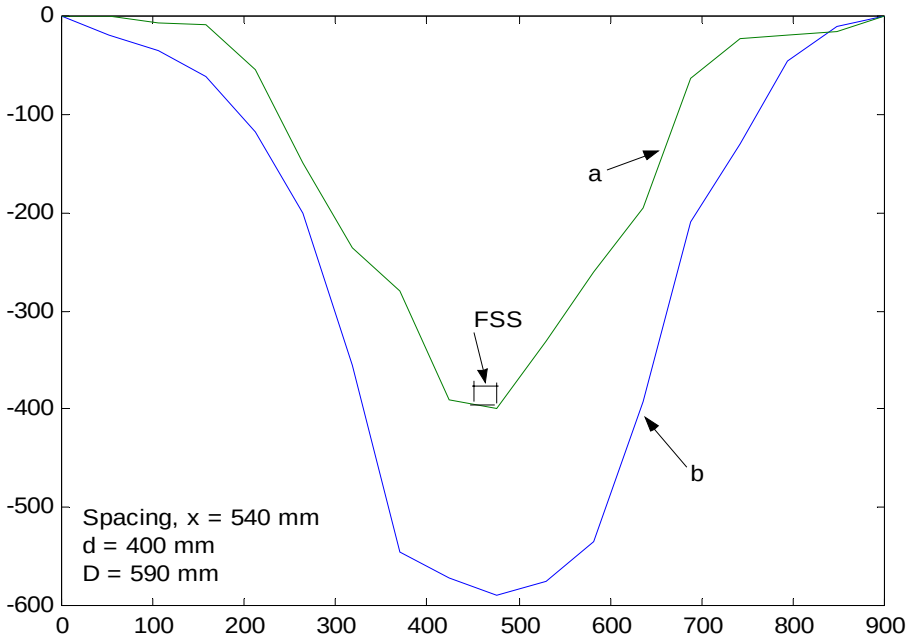

Figure 6.4a: Measured cross-section areas of failed soil-profile at the FSS and RSS. (x = 540 mm).

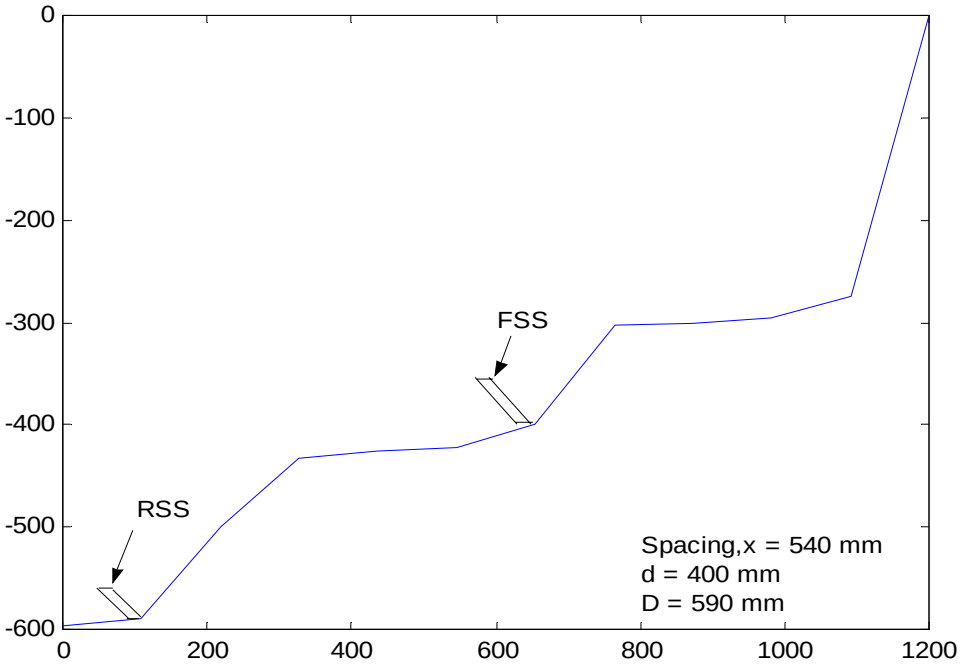

Figure 6.4b: Measured longitudinal section of the failed-profile by the two subsoilers (x = 540 mm).

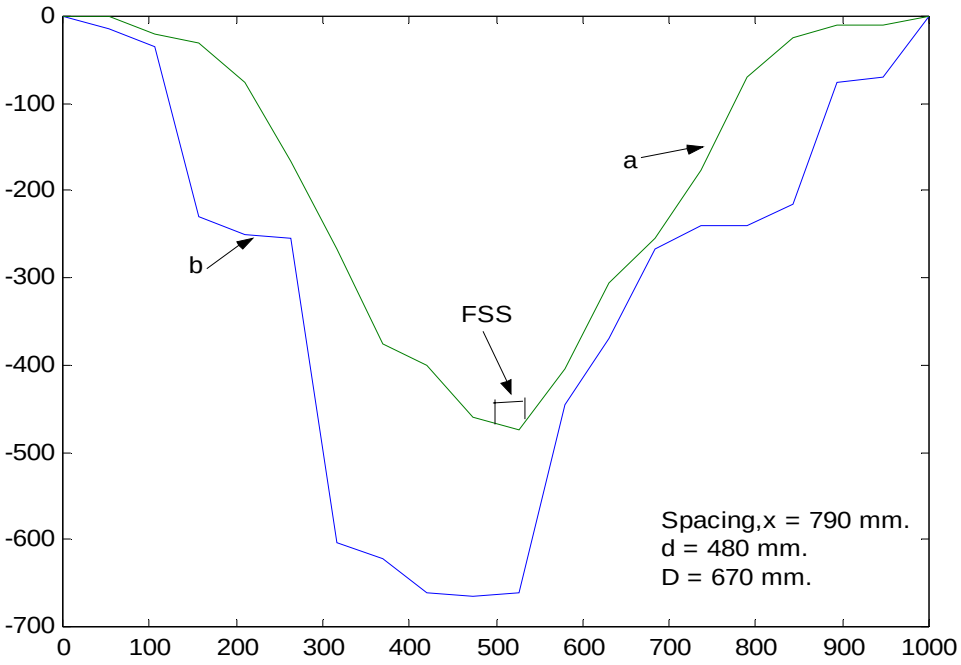

Figure 6.5a: Measured cross-section areas of the failed soil-profile at the FSS and RSS. (x = 790 mm).

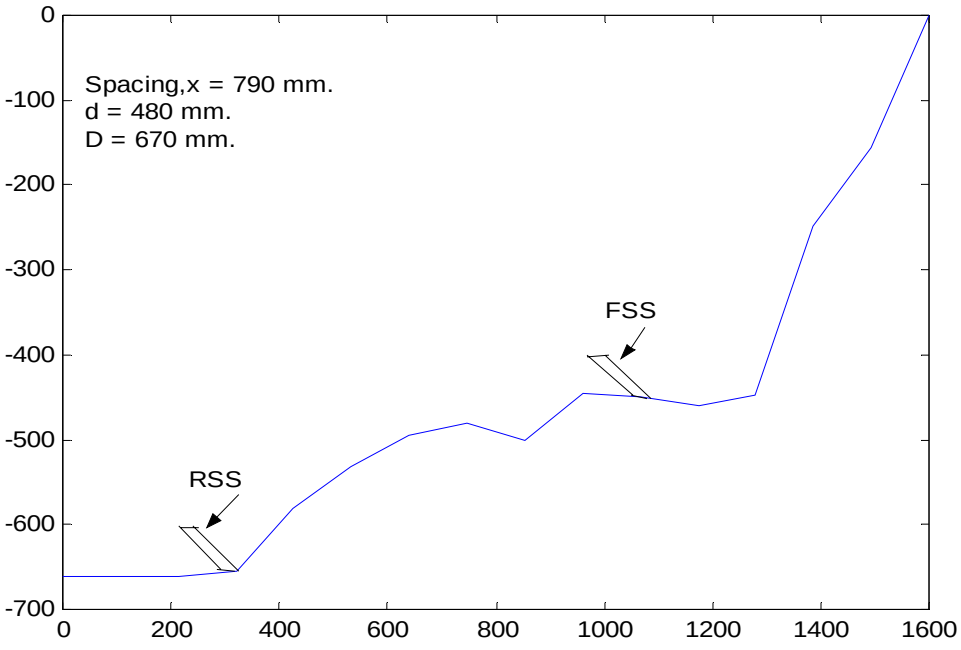

Figure 6.5b: Measured longitudinal section of the failed-profile by the two subsoilers (x = 790 mm).

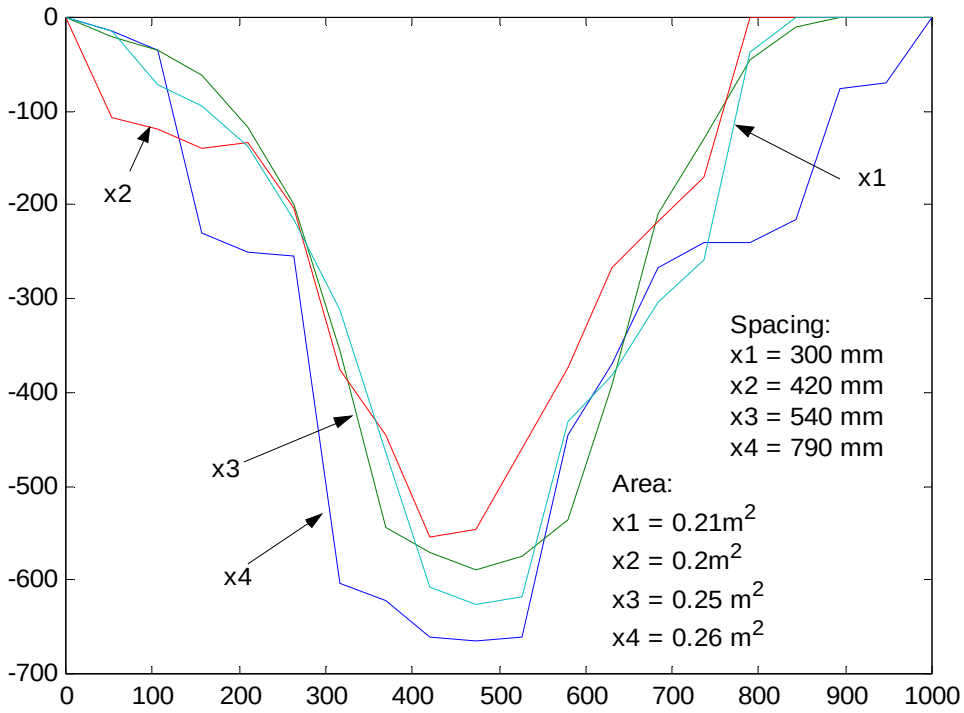

Figure 6.6a: The maximum cross-sectional areas of failed-profiles at varying spacing.

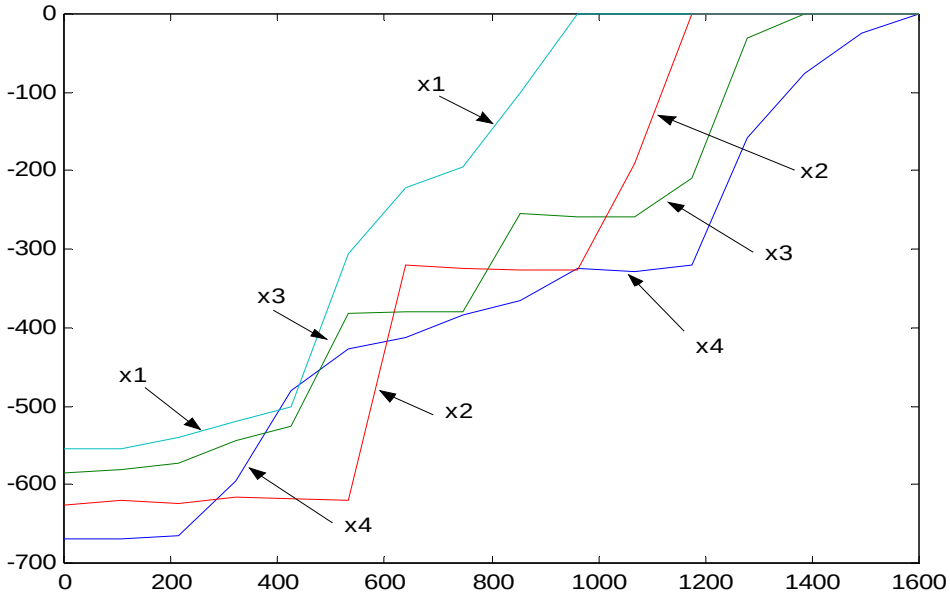

Figure 6.6b: Maximum longitudinal sectional areas of failed-profiles at varying spacing.

Figures 6.6a and 6.6b present the maximum cross-sectional and longitudinal areas respectively of the failed profiles at the four different spacings used in the study. The soil water content ranged between 8.53 and 9.93% db and it is clear from the figures that the size of the tilled maximum cross-sectional and longitudinal areas increased as the spacing was increased.

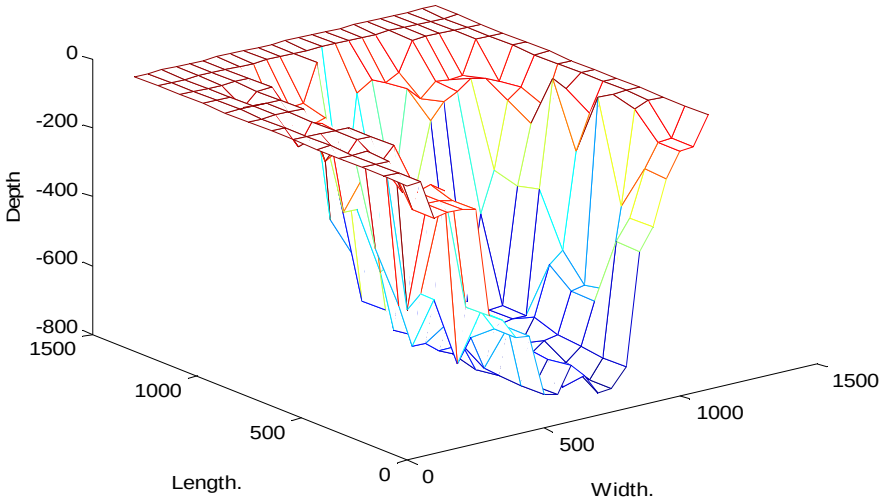

Figure 6.7: Computer-Penetrometer measured profile.

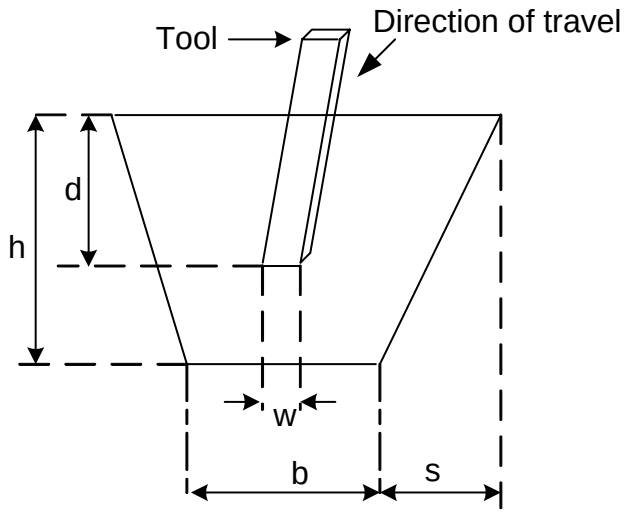

Figure 6.7a: Penetrometer measured shape of the failed cross-sectional area.

The shape of the same disturbed profile identified by prodding with a penetrometer is shown in figure 6.7. As shown in figure 6.7a the bottom of the profile was located at a depth, h which was lower than the tool operating depth, d. The profile bottom width, b was also found to be wider than the tool width, w. This means that based on the penetrometer, the action of the tillage tool fails soil beyond its operating depth and width. For example, the tool operating depth was 580 mm but the computer-penetrometer method located the bottom of soil-failed profiled at 723 mm. As explained in the literature, this is caused by the spiral failure-surface originating from the rear subsoiler going below its operating depth and also wider than the tillage tool. This method of measuring the three-dimensional failed-profile was discontinued because data logging was too time consuming. However, this method certainly justifies further development as it can offer much more advantages.

6.3 Formation of the longitudinal soil-failure pattern.

The formation of the longitudinal soil-failure patterns at the font and rear subsoileras interpreted based on the vertical and longitudinal force on the subsoiler are presented in figures 6.8a and 6.8b respectively. From point b_1 (fig.6.8a), the front subsoiler compressed a block of soil and the draft force (D_f) increased reaching a peak at point c_1 just before failure took place, then it dropped to e_1. When the soil failed at c_1, the vertical force (V_f) instantaneously increased from c_2 to e_2 as part of the failed block was accelerated up the share. The front subsoiler also carried the soil while it moved up the inclined surface of the share thus increasing the vertical load.

At the rear subsoiler (fig.6.8b), the same soil-failure pattern developed except that when the draft force (D_f) was maximum at FSS, it (D_r) was minimum for the RSS. This means therefore that the moment of soil failure at the FSS (a_1) coincided with the commencement of soil compression at the RSS (a_3) and vice versa. The alternation of soil-failure at the two subsoilers reduced their total draft requirements since high draft force at the FSS corresponded with low draft force at RSS as can be seen in figure 6.8.

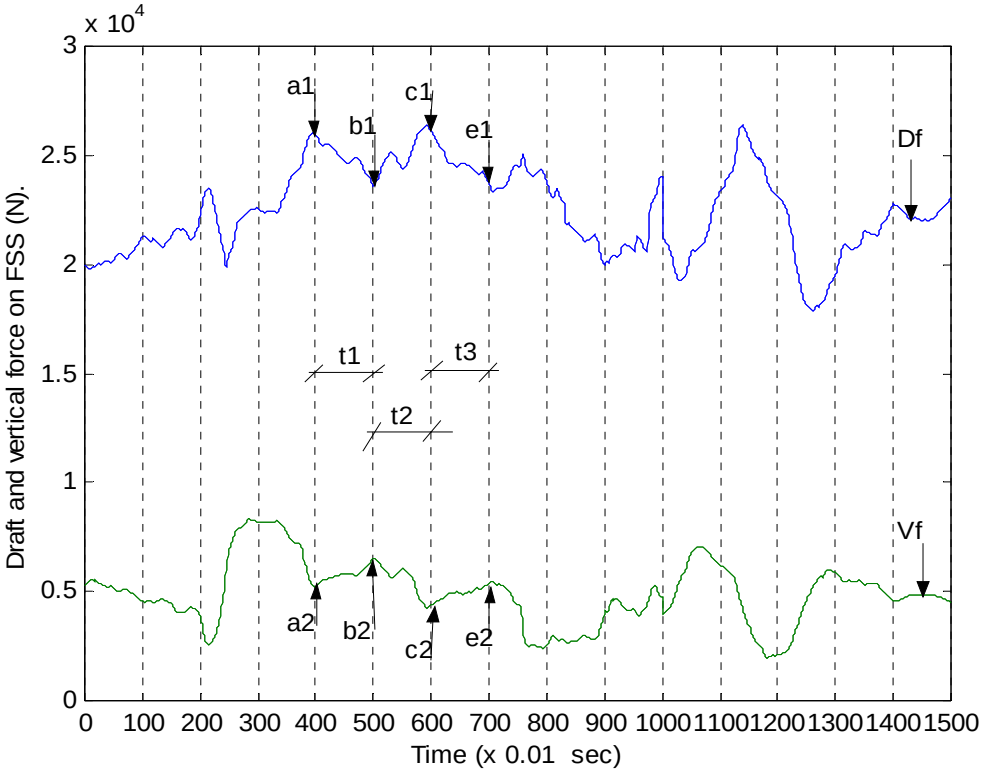

(a). Front Subsoiler.

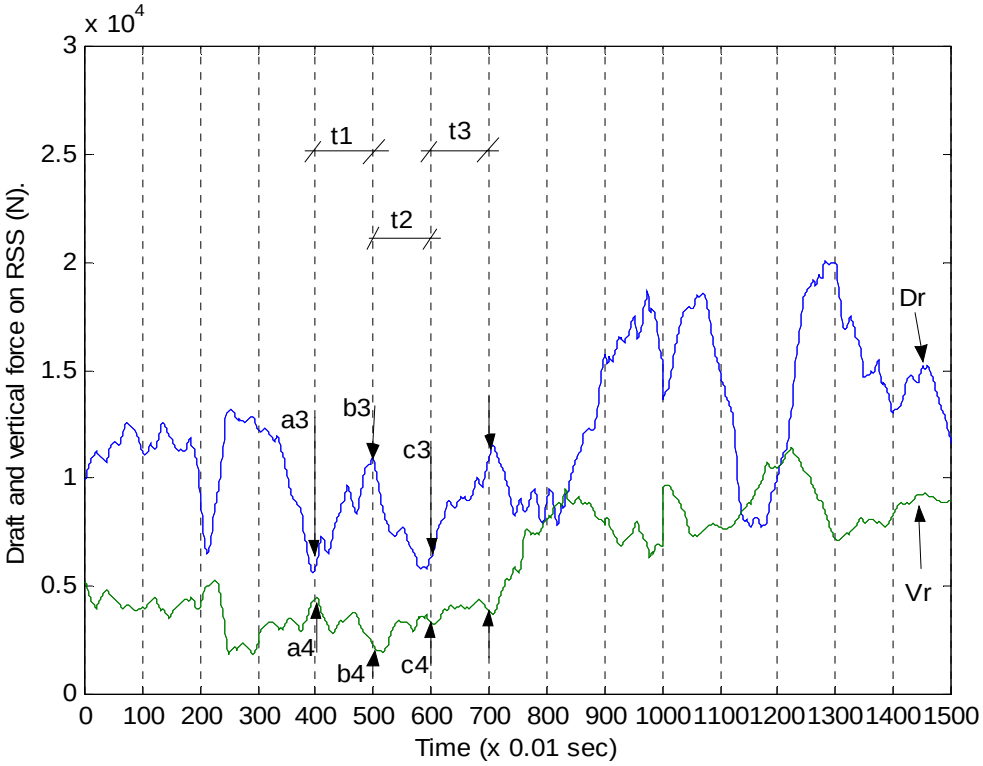

(b). Rear Subsoiler.

Figure 6.8: Longitudinal soil-failure pattern at the front and rear subsoilers. (Spacing x = 300 mm).

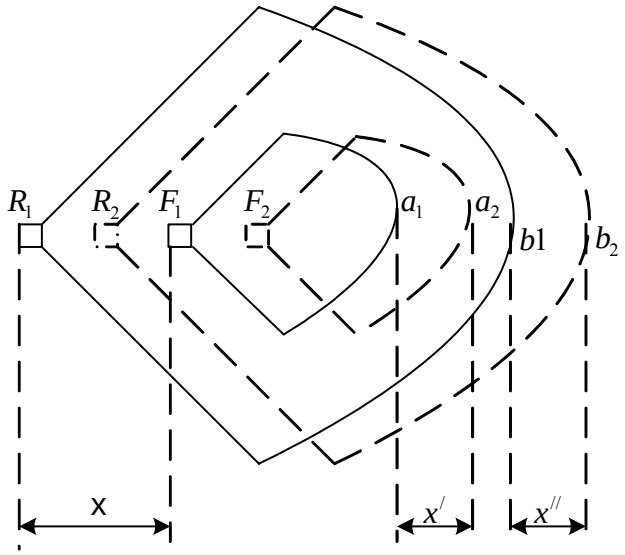

Figure 6.9: Top view of the failed soil profile by two subsoilers in tandem. (spacing x = 300 mm).

In figure 6.9, the forward tip of the block failed by rear subsoiler R_1 is at point b1 while that of the front subsoil is located at point a_1. When the subsoilers move forward to positions R_2 and F_2 respectively, the forward tips of the failed blocks are at points a_2 and b_2 for the FSS and RSS respectively.

For FSS (fig. 6.8a & 6.9), the theoretical failed-block length, $b_1c_1 = x^{/} = vt_2 = 0.44$ m.
The distance covered accelerating the failed block = $vt_2 = 0.44$ m.
For RSS (fig. 6.8b & 6.9), the theoretical failed-block length, $a_3b_3 = x^{//} = vt_1 = 0.44$ m.
The distance covered accelerating the failed block = $vt_1 = 0.44$ m.
Unfortunately the lengths of failed blocks were not experimentally recorded.
Where:
v = Operating speed of the subsoiler (0.44 ms^{-1}).
t_i = Time (1 s). i = 1,2,3,…n.

At a close spacing of 300 mm, the failed-blocks by both subsoilers, were of the same length and the duration for compressing, the soil-block and accelerating and lifting it after failure was almost equal. It was noted though that the above outlined maxima and minima in the failure-patterns at both subsoilers were at times slightly out of phase.

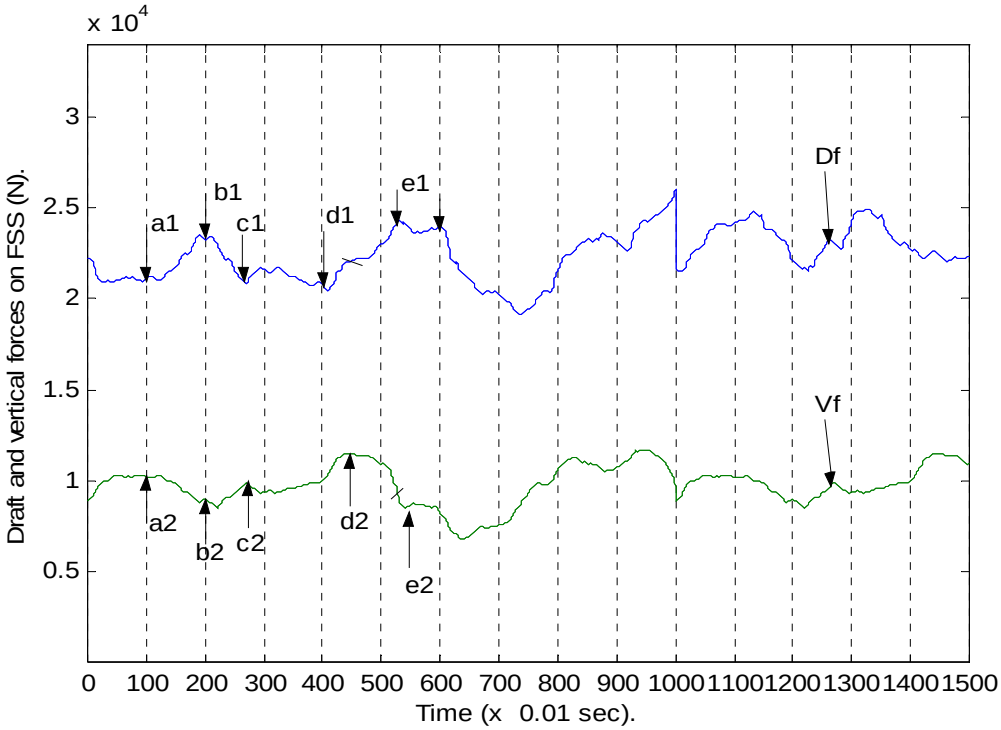

(a): Front subsoiler.

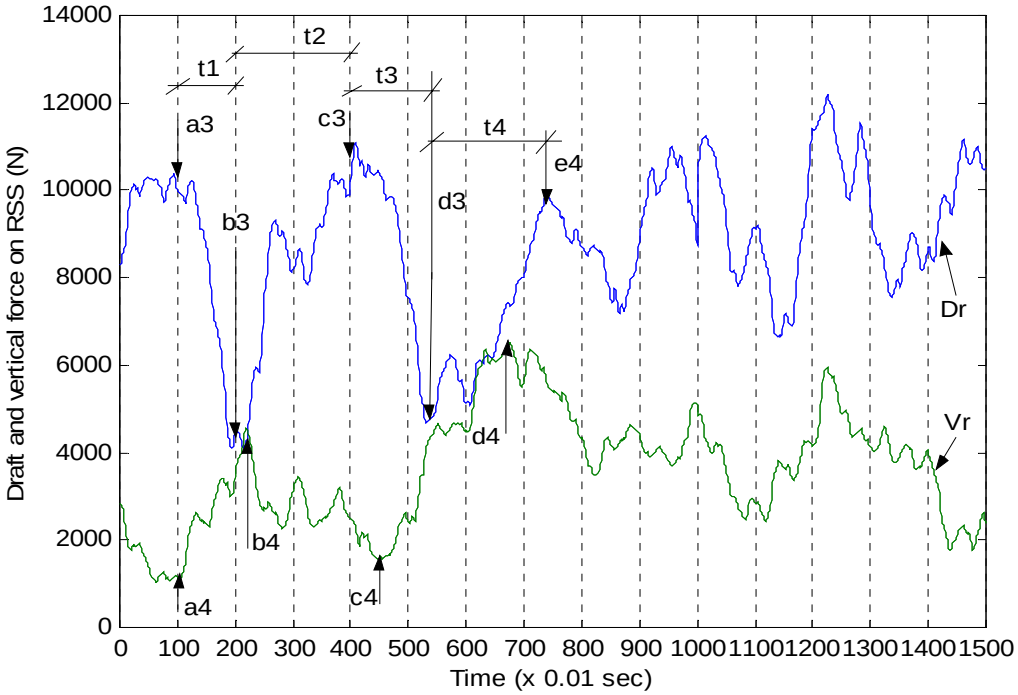

(b): Rear subsoiler.

Figure 6.10: Longitudinal soil-failure pattern at the front and rear subsoilers. (Spacing x = 790 mm)

The soil failure pattern at the font and rear subsoiler as depicted by soil forces, is presented as depicted by the soil forces for a spacing of 790 mm in figures 6.10a and 6.10b respectively. For the FSS (fig.6.10a), the draft force is generally out of phase with the vertical force. That is when the draft force is at maximum, the vertical force is not necessarily at a minimum. The peaks of both the draft and vertical forces are also not uniformly spaced.

For the RSS (fig.6.10b), the draft and vertical forces are also out of phase. However, the duration for soil compression seem to be longer than accelerating it after failure. For example:

Time taken to compress the soil from b_3 to c_3, $t_2 = 2s$.
The length of the compressed block, $l = vt_2 = 0.88$ m.
To accelerate this block from c_3 to d_3, the time taken, $t_3 = 1.5$ s.
The distance covered accelerating and lifting this block = $vt_3 = 0.66$ m.

At a larger spacing of 790 mm, the two subsoilers reacted independently. This resulted in increased total draft force. However, since the rear subsoiler compressed larger soil-blocks, the maximum failed cross-sectional areas were much larger as compared to a closer spacing resulting in larger cross-sectional areas tilled per unit draft force.

6.4 Variation of force components on the front and rear subsoiler.

Figures 6.11a and 6.12 show the variation of the draft force and vertical loading at the front (FSS) and rear subsoiler (RSS) respectively as the spacing was varied. The operating depth of the front subsoiler was 410 mm while that of the rear subsoiler was 600 mm. This means that the effective operating depth of the rear subsoiler in undisturbed soil was 190 mm. At a close spacing of 300 mm, the rear subsoiler recorded a higher draft force value (RSS) than the front subsoiler (FSS) as shown in figure 6.11a. When the subsoilers are close at this operating depth of the front subsoiler, the rear

subsoiler did most of the tilling and therefore it required a lager draft force than the front subsoiler.

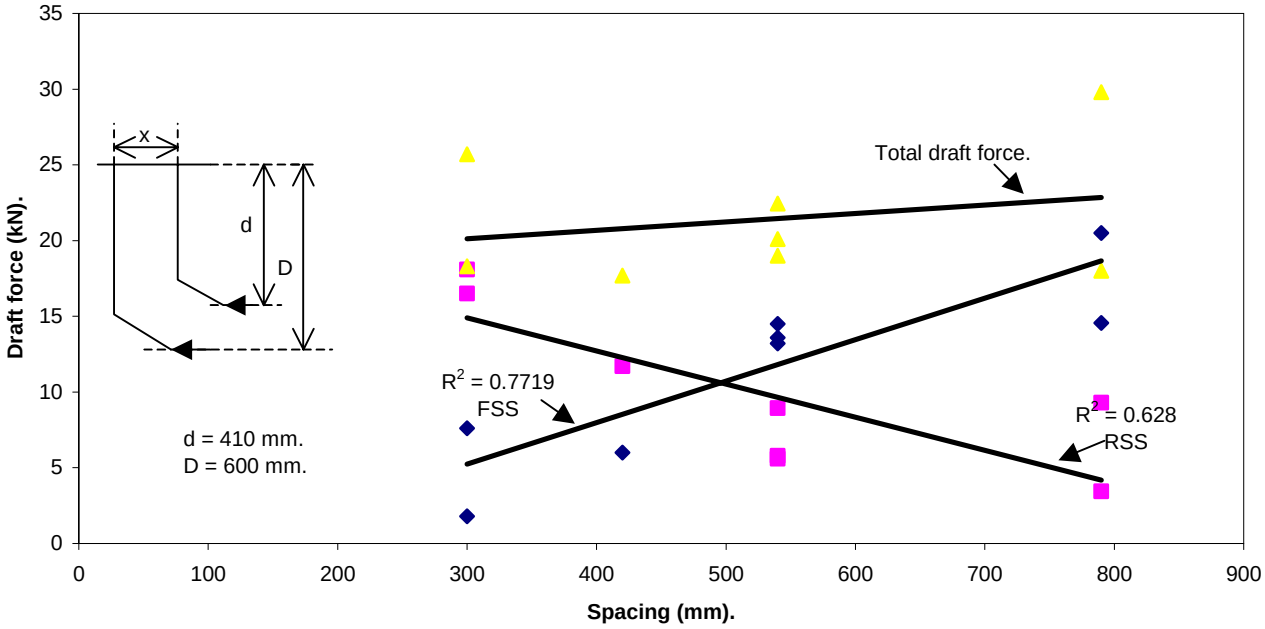

Figure 6.11a: Variation of the draft force with spacing,x at the front and rear subsoiler. (d = 410 mm).

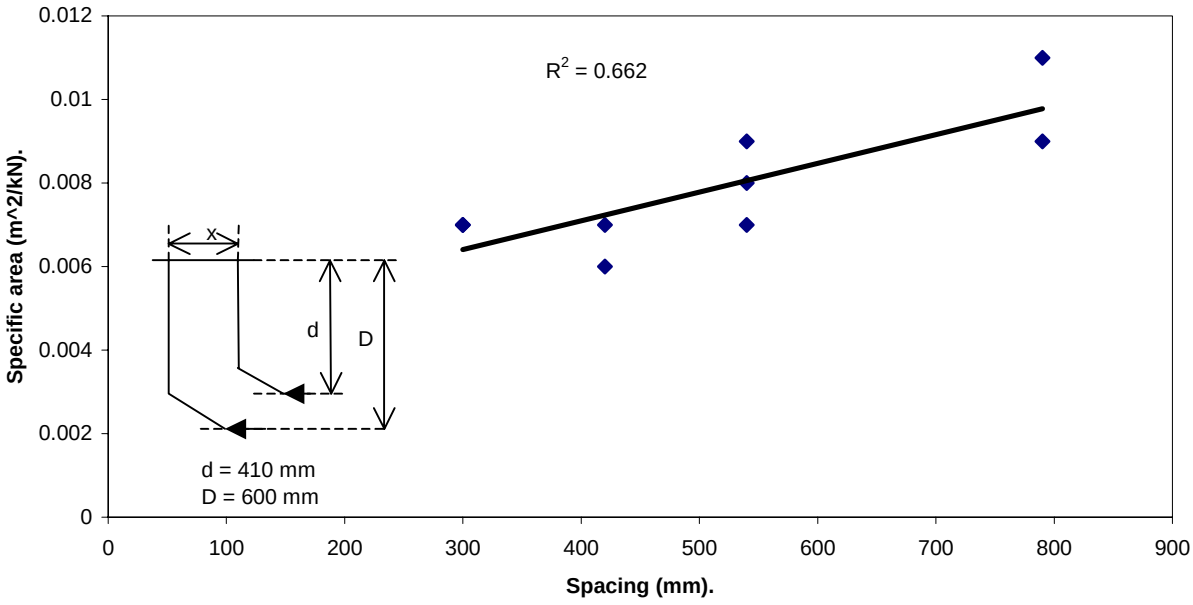

Figure 6.11b: Cross-section area tilled per unit draft force versus spacing, x. (d = 410 mm)

As the spacing increased, the draft force requirement of the front subsoiler increased as that of the rear decreased. This was due to a reduction of the RSS influence to that of the FSS. The total draft force increased with spacing. As noted earlier, the maxima and minima of the draft and vertical forces in the soil-failure patterns at RSS and FSS were out of phase at large spacing, which resulted in increased total draft force requirements.

The term specific area designates the cross-section area tilled per unit draft force. Even though the total draft force increased, the specific area also increased with spacing as indicated in figure 6.11b. This means therefore that the failed cross-sectional area increased faster than the exerted draft force.

It was anticipated that at this close spacing, the front subsoiler would carry more vertical load but from figure 6.12, in practice the rear subsoiler (RSS) carried more vertical load. This is attributed to the fact that the rear subsoiler does most of the tilling and therefore it inevitably carries more vertical load. The total vertical load on the FSS increased with increased spacing, as the subsoilers are loaded independently.

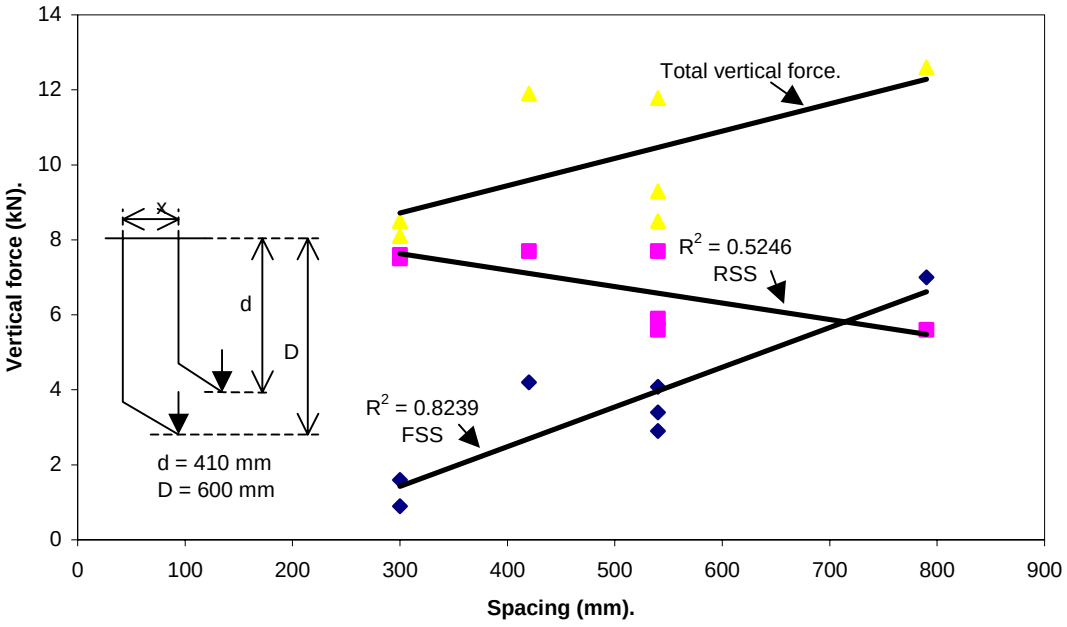

Figure 6.12 : Variation of vertical force with spacing, x at the front and rear subsoiler. (d = 410 mm)

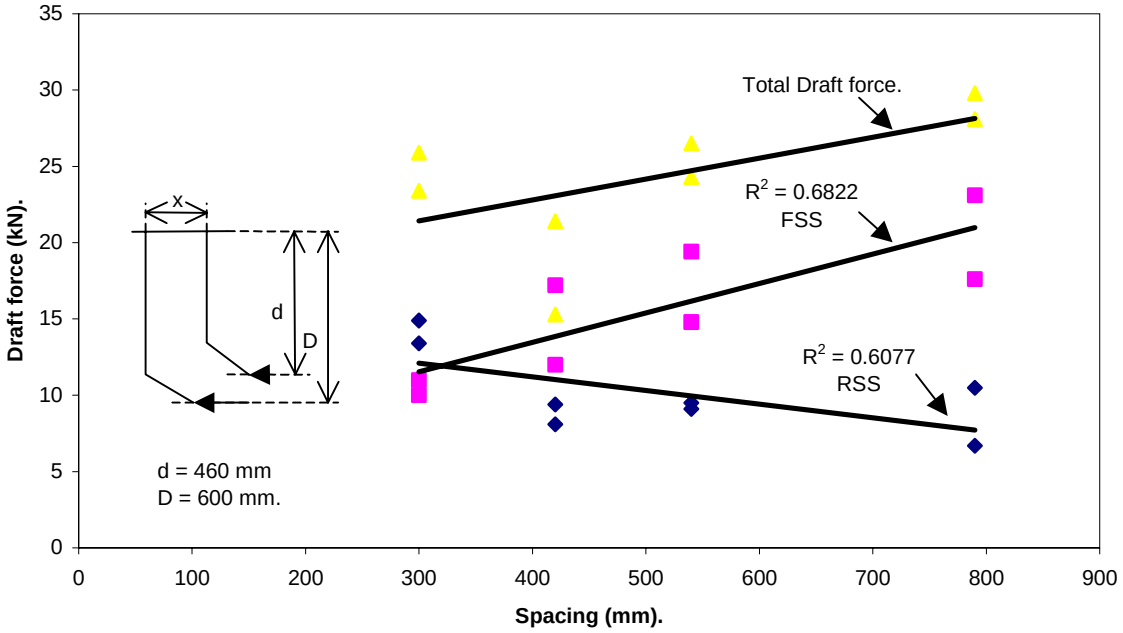

Figure 6.13a : Variation of the draft force with spacing, x at the front and rear subsoilers. (d = 460 mm)

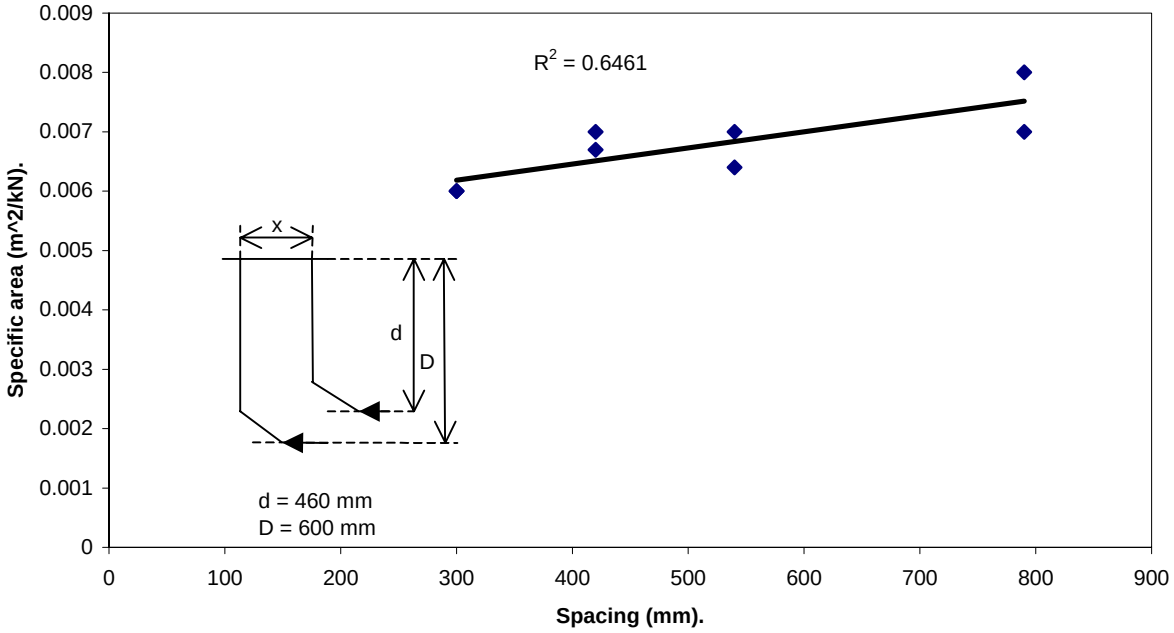

Figure 6.13b : Cross-section area tilled per unit draft force versus spacing, x. (d = 460 mm).

In figure 6.13a, the variation of the draft force is presented when the operating depth of the front subsoiler was increased to 460 mm. At the closest spacing, the two subsoilers were working as a unit therefore their draft force requirement was almost equal. As the

spacing was increased, the draft force for the front subsoiler increased and that of the RSS reduced for the same reasons as above. The total draft force increased with spacing as well as the specific area as explained earlier (fig.6.13b).

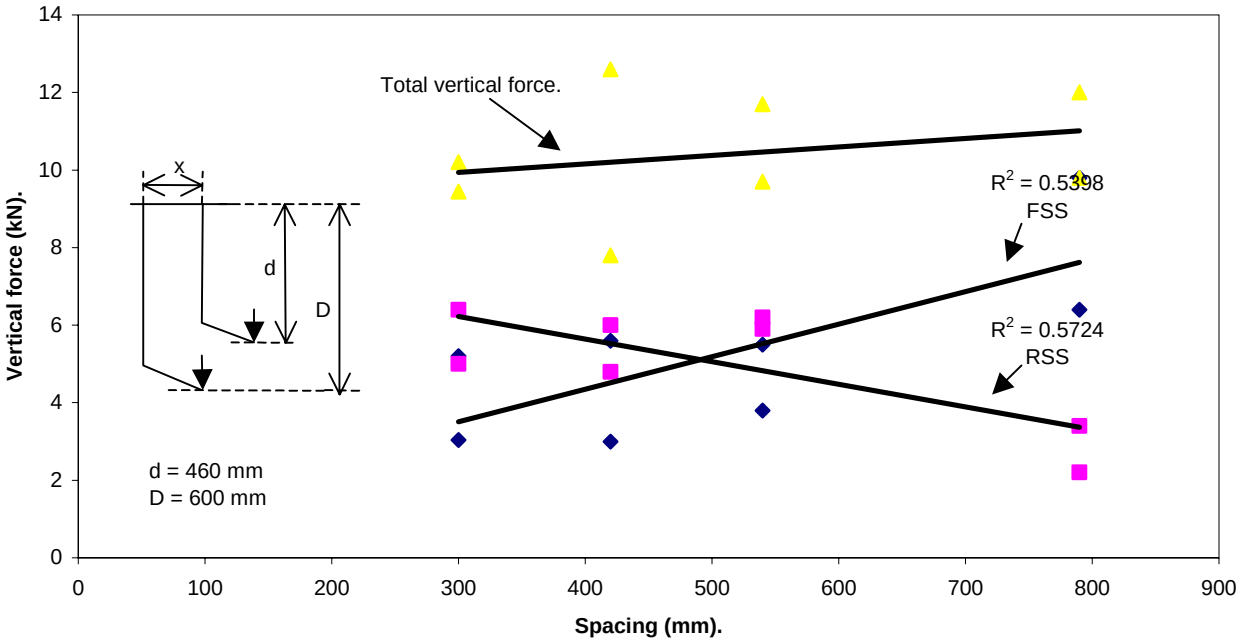

Figure :6.14: Variation of vertical force with spacing, x at the front and rear subsoiler. (d = 460 mm).

Since the vertical spacing between the subsoilers was only 140 mm, the rear subsoiler carried more vertical load at a close horizontal spacing of 300 mm (fig. 6.14). As the spacing increased, the vertical load on the front subsoiler increased as the influence from the rear subsoiler reduced. At the same time, the vertical load on the rear subsoiler reduced. The total vertical load increased with spacing. The low R-square values are attributed to variation in soil water content even though it was kept as constant as possible. Figure 6.15a presents the variation of the draft force at both subsoilers when the operating depth of the front subsoiler was increased to 510 mm, without changing that of the rear subsoiler. Since at a spacing of 300 mm the subsoilers were vertically and horizontally close, they displayed an almost equal draft force requirement. As the spacing was increased, the influence of the rear subsoiler to the front one reduced. This resulted in increasing the draft force requirement of the front subsoiler while reducing

that of the rear subsoiler. As explained earlier, the total draft force and specific area (fig. 6.15b) increased with increased spacing.

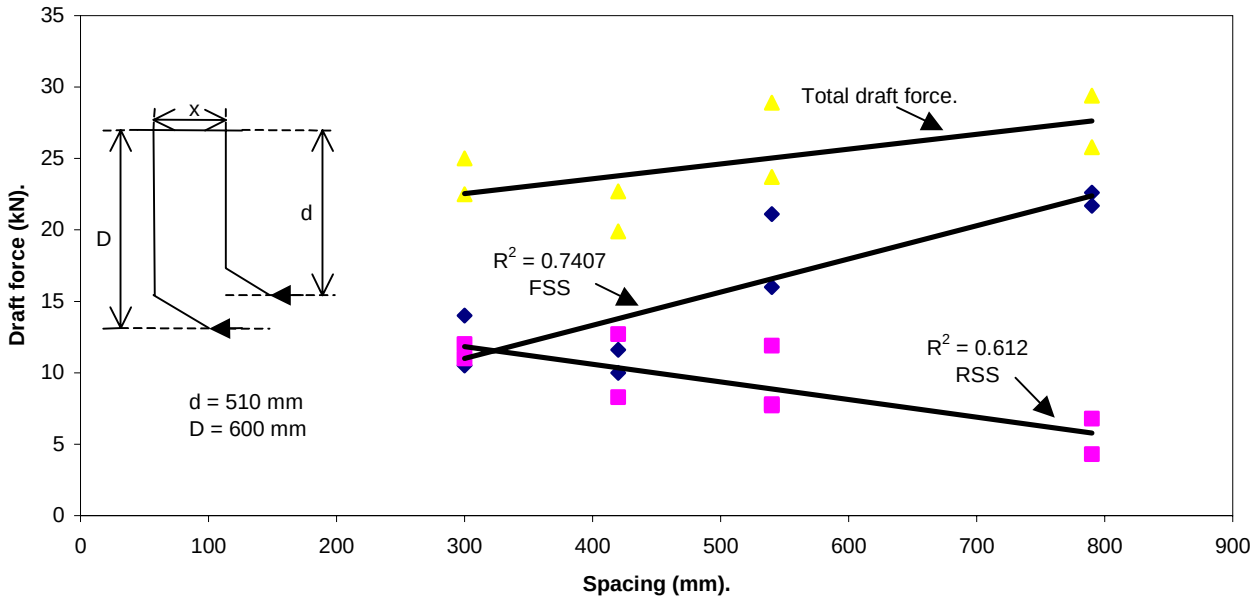

Figure 6.15a: Variation of draft force at the front and rear ubsoiler with spacing, x. (d = 510 mm).

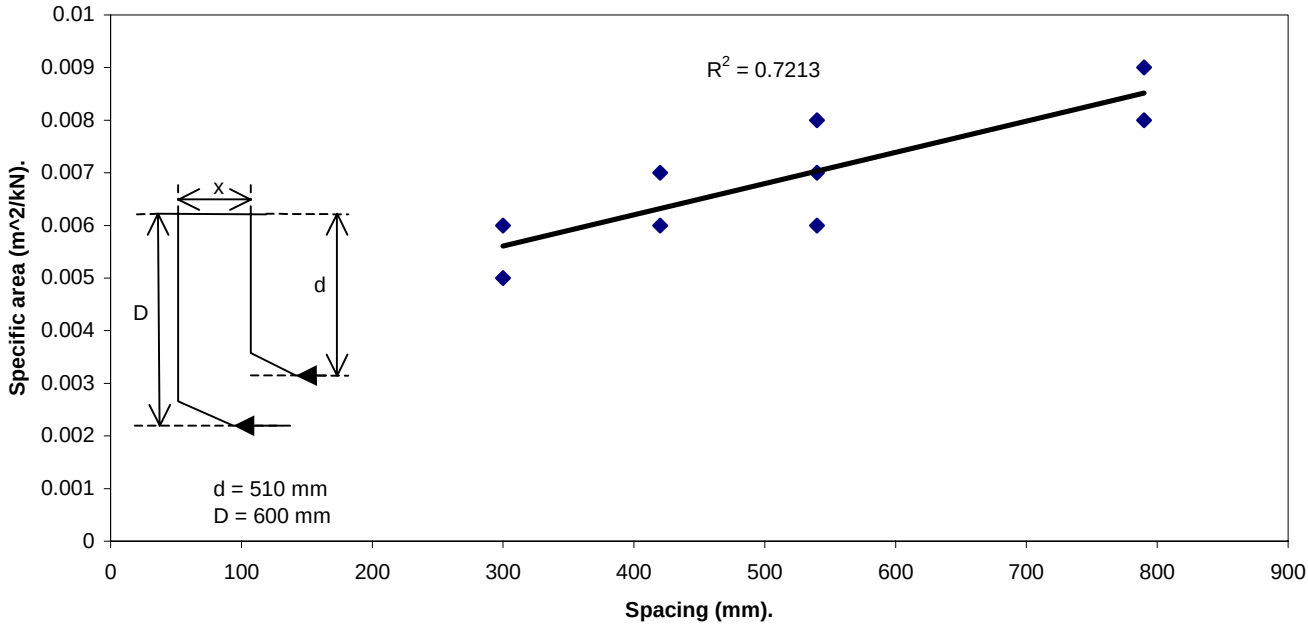

Figure 6.15b: Cross-section area tilled per draft force versus spacing. (d = 510 mm).

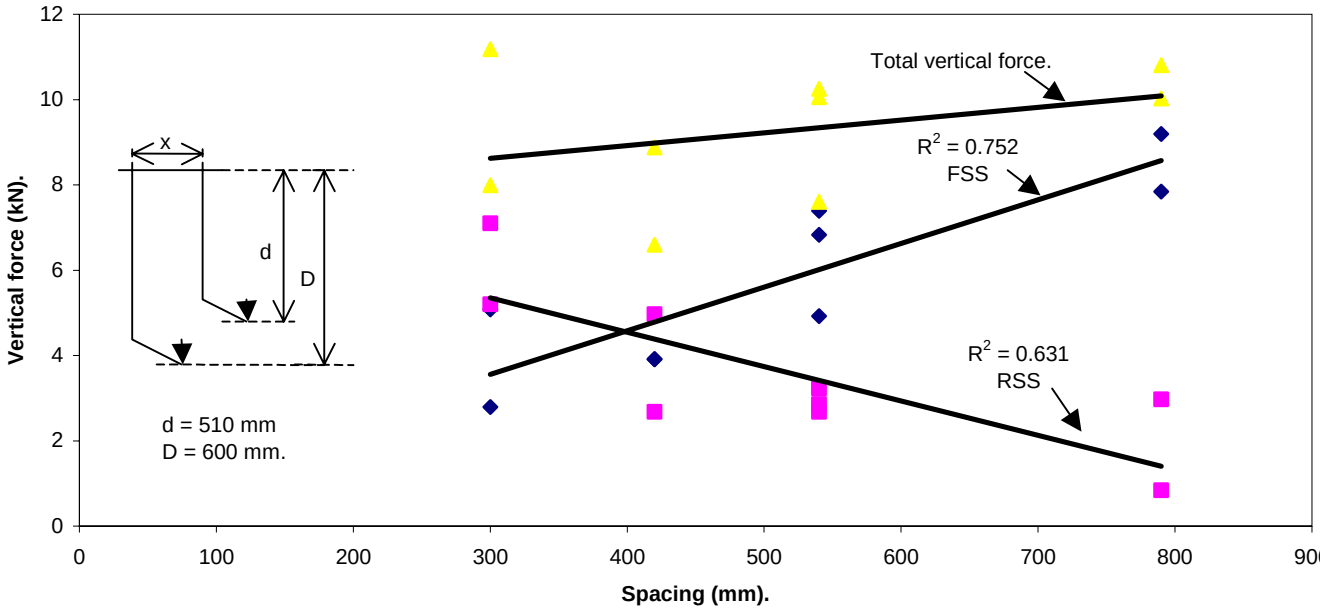

Figure 6.16 : Variation of the vertical force with spacing at the front and rear subsoiler. (d = 510 mm)

Figure 6.16 shows how the vertical force varied at each subsoiler when the operating depth of the front subsoiler was 510 mm. Due to the closeness of the subsoilers at a spacing of 300 mm, the rear subsoiler carried slightly more vertical load. As the spacing increased each subsoiler started to till more independently resulting into increased vertical load at the front subsoiler and decreased at the rear subsoiler.

6.5 Performance of the mathematical soil-failure and force models.

6.5.1 Prediction of the volume of the failed-profile.

In the proposed mathematical model, Swick and Perumpral's (1988) empirical equation was tested on how accurately it predicted the maximum width of the failed circular wedge, s. This equation is reproduced below:

$$s_f = 0.46R_f + 0.904(\alpha) - 6.03 \quad \text{.....6.1.}$$

Where:

s_f = Maximum width of the side circular-wedge failed by the FSS (cm).

R_f = Rupture radius of the FSS (cm).

α = Rake angle (degrees).

It was however observed that for the specific circumstance of the front subsoiler, this equation greatly over predicted the maximum width of a failed soil-profile as well as the rupture radius, leading to the failed volume being over predicted by the model. Since the draft force is related to the soil-volume failed and failure surface area, it was anticipated that the model was likely to also over predict the exerted force. In practice this did not happen but predicted and recorded forces were comparable. The front subsoiler was also operated deeper than for the research results reported by Swick and Perumpral (1988).

As pointed out earlier, the soil water content (swc) variation was kept as close as possible during the field experiments. The data collected when soil water content exceeded the targeted range was omitted when testing the performance of the proposed model however from such data, it was observed that the failed profiles were either too wide or too narrow depending on the soil water content. The data was therefore used to express the maximum width of the failed-circular wedge (s) for the rear subsoiler as a function of soil water content. Thus s = f(swc) is presented in equation 6.2 and figure 6.17.

$$s_r = 1146.6e^{-0.1413x} \quad \text{.....6.2.}$$

Where:

s_r = Maximum width of a failed circular-wedge (mm) at an operating depth of 600 mm of RSS.

x = Soil water content (db%).

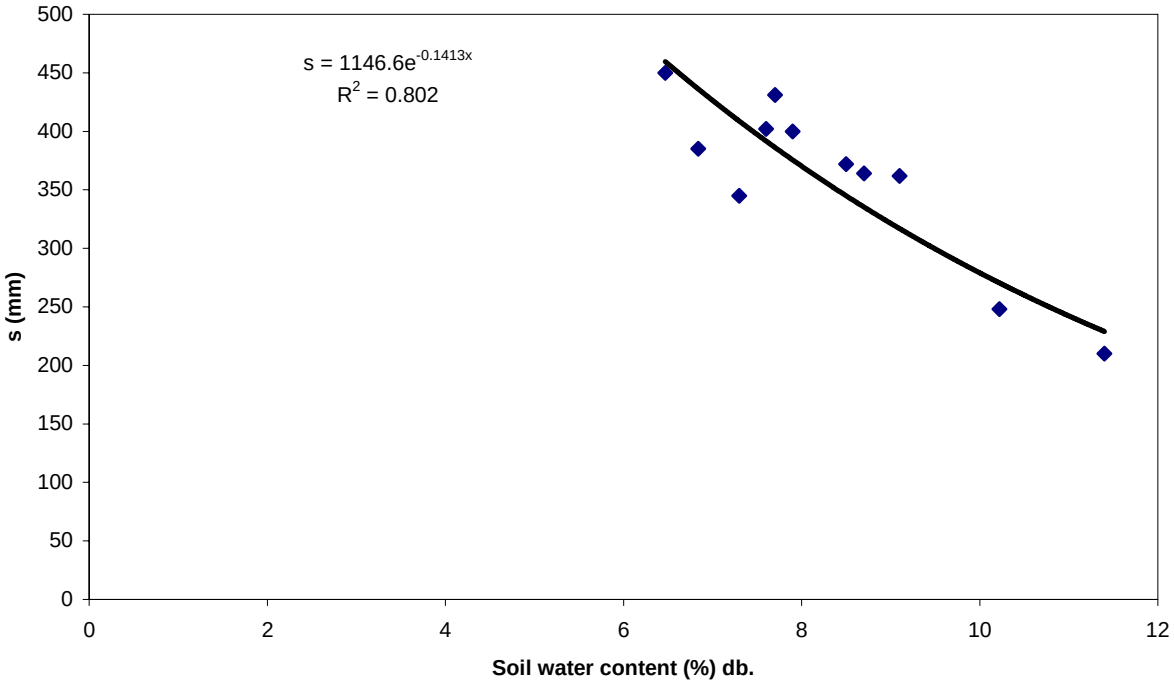

Figure 6.17: Measured maximum 's' versus soil water content at an operating depth of 600 mm.

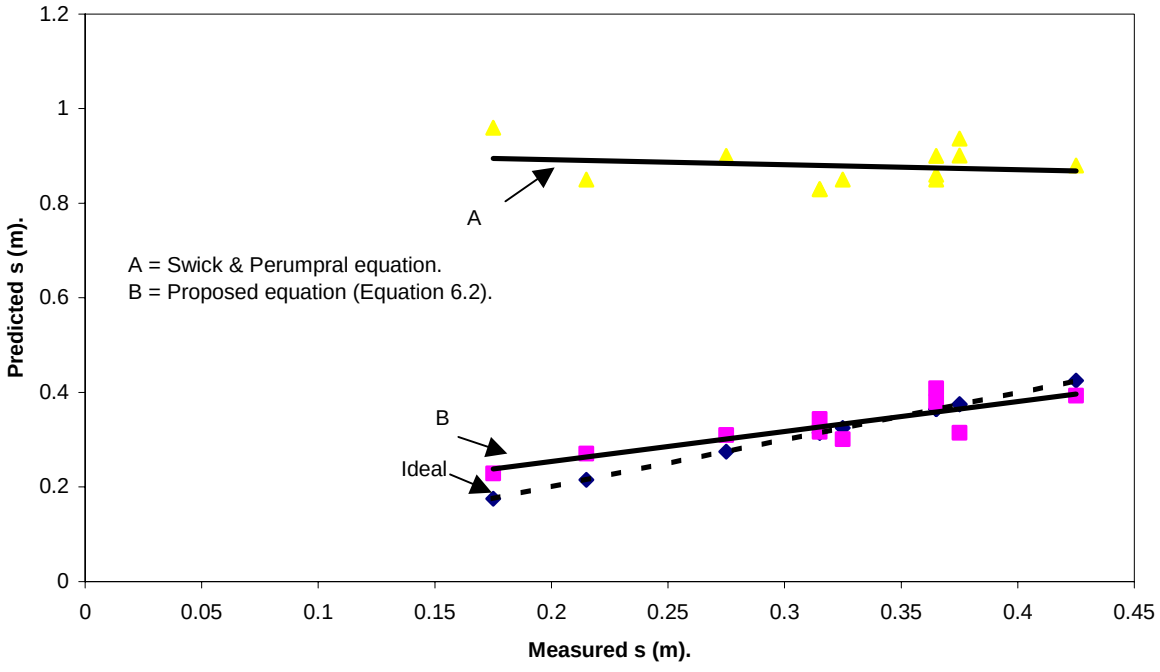

Figure 6.18: Comparing measured s with that predicted by the proposed and Swick's equation at different values of swc.

Figure 6.18 compares the measured "s" for the rear subsoiler with those determined by equations 6.1 and 6.2. From this figure, it is clear that equation 6.1 greatly over predicts the width of the failed profile. This is due to over prediction of the rupture radius, which is a characteristic of the mathematical model based on analytical analysis. In such models the true covered rupture plane is replaced with a flat plane resulting in over prediction of rupture distance. Further more this equation is insensitive to soil water content since they worked with dry soils under laboratory conditions. However equation 6.2 adequately predicted the maximum width of the failed soil-profiles.

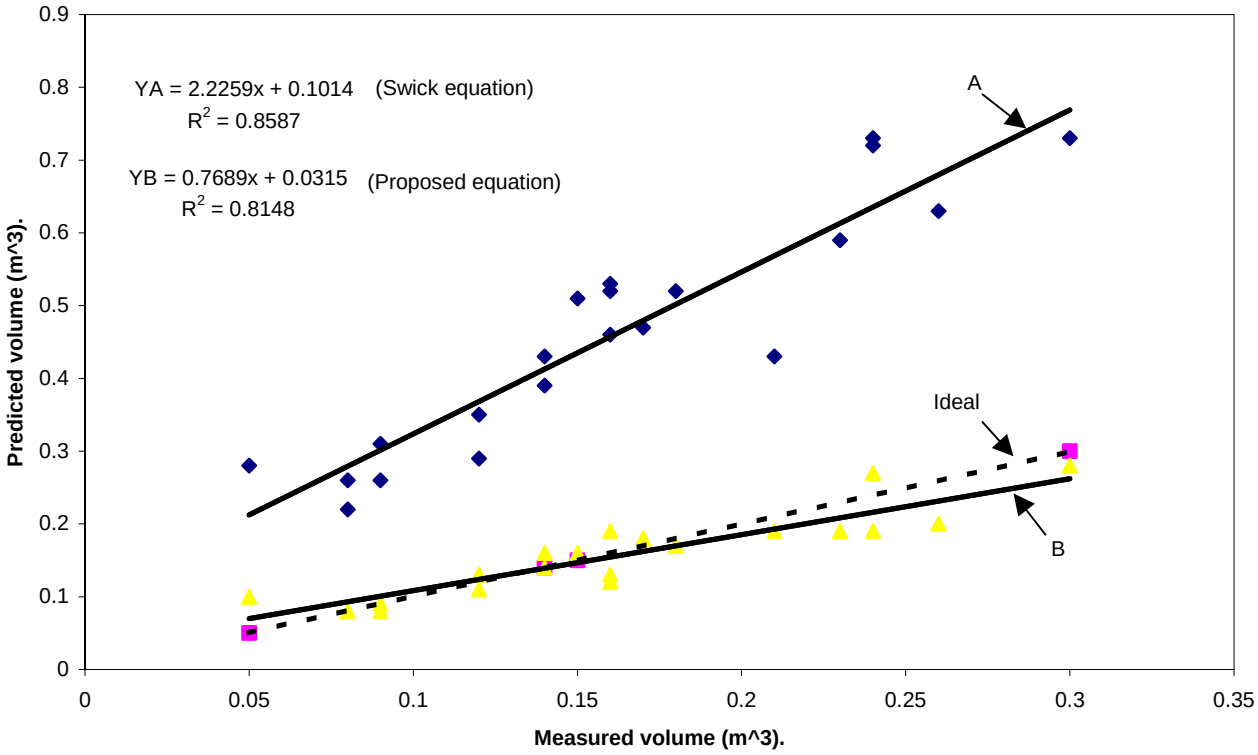

Figure 6.19: Comparison of measured and predicted volume of the failed-profiles.

The relationship, between the measured and predicted volumes of the failed soil-profiles, is presented in figure 6.19. The proposed mathematical model was used to predict the total volume of the failed-profiles. The fitted regression line A represents the failed soil-volume prediction when the maximum width of the side circular-wedge was determined by equation 6.1. While for B, it was determined by the proposed equation (equation 6.2).

Regression line A has a slope and an intercept of 2.2 and 0.1 respectively, with a coefficient of determination equal to 0.86. Both the slope and the intercept indicate that the model over predicts the amount of soil failed. While regression line B has a slope and an intercept of 0.77 and 0.03 respectively, with a coefficient of determination equal to 0.81. In this case, failed soil volumes were adequately predicted since the slope and the intercept of the regression line are not significantly different from one and zero respectively. The over prediction (case A) can therefore be attributed to the fact that equation 6.1 over predicting s and for being insensitive to soil water content. In the proposed mathematical model, the proposed equation 6.2 was used to predict s.

6.5.2 Prediction of disturbed cross-sectional area per unit draft force.

The cross-section areas of soil disturbed per unit draft force (specific area) were determined from measured and predicted cross-section areas of the failed soil-profiles. According to Godwin (1974), the volume of soil cut per unit input energy can be expressed as follows:

$$\frac{Volume-cut}{Energy-input}=\frac{AX}{HX}=\frac{A}{H} \quad \text{.....6.3.}$$

Where:

A = Maximum cross-sectional area of the failed soil-profile (m^2).

X = Distance traveled (m).

H = Exerted draft force by the tillage tool (kN).

$$A = d(w + s) \quad \text{.....6.4.}$$

Where:

d = Operating depth of the tillage tool (m).

w = Width of the tillage tool (m).

s = Maximum width of the side circular wedge of the failed soil-profile (m).

The proposed mathematical model was used to predict both the cross-section area and the soil-volume disturbed.

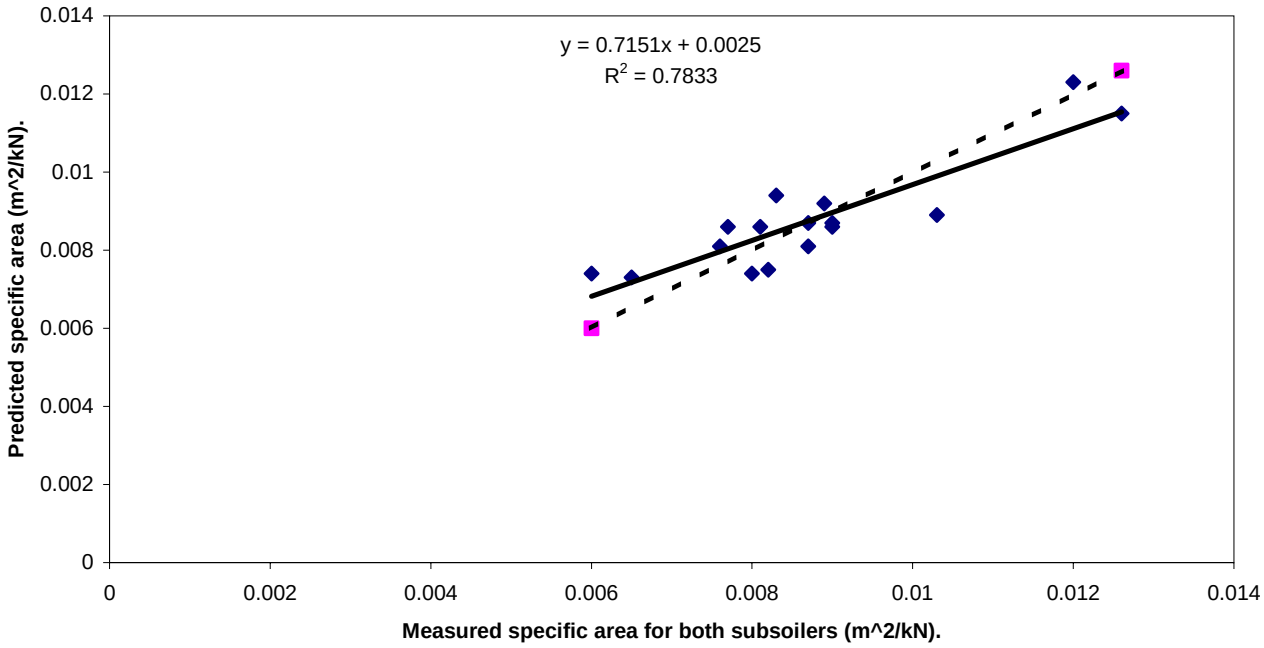

Figure 6.20: Comparison of measured and predicted specific area for both subsoilers.

Figure 6.20 presents the comparison of measured and predicted disturbed cross-section areas per unit draft force for the two subsoilers combined. The fitted regression line has a slope and an intercept of 0.72 and 0.003 with R-square equal to 0.78. The slope is not significantly different from one but the intercept is significant. The significance of this intercept is attributed to experimental random errors.

Figure 6.21 compares the measured and predicted cross-section area failed per unit draft force by the front subsoiler based on Swick's model. The regression line has a slope and an intercept of 0.81 and 0.01 respectively with R-square equal to 0.74.

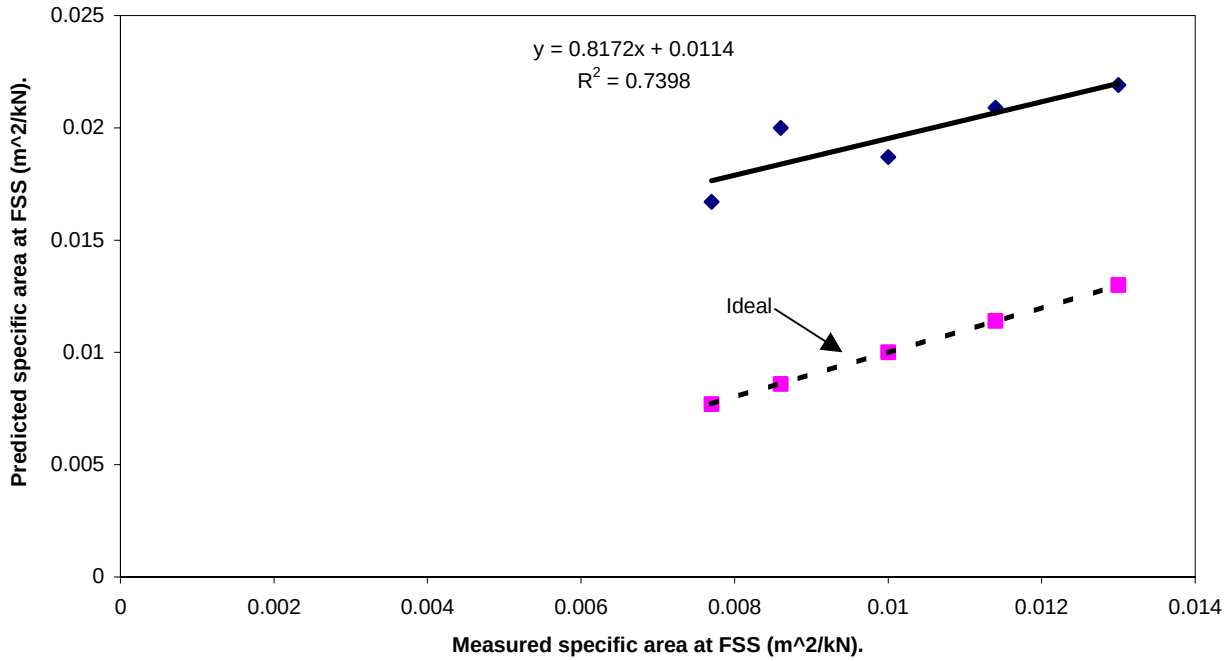

Figure 6.21: Comparing predicted and measured specific area at the front subsoiler based on the Swick-model.

Using longitudinal sections of the manually measured soil-profiles at maximum spacing, the positions of the two subsoilers were identified. The vertical cross-section areas of the failed soil-profiles at these locations were determined. By subtracting the cross-section area cut by the front subsoiler from the total maximum area, the cross-section area disturbed by the rear subsoiler was determined. Thus determining the cross-section area failed per unit draft force by the rear subsoiler.

A similar regression line in figure 6.22 for the rear subsoiler has a slope and intercept of 0.73 and 0.0013 respectively and R-square equal to 0.88. In both cases, the slope and the R-square values are reasonable. However for the front subsoiler, the intercept is significant due to over prediction of the specific area by the model. The intercept for the rear subsoiler is not significantly different from zero therefore the proposed model adequately predicted the cross-section area tilled per unit draft force.

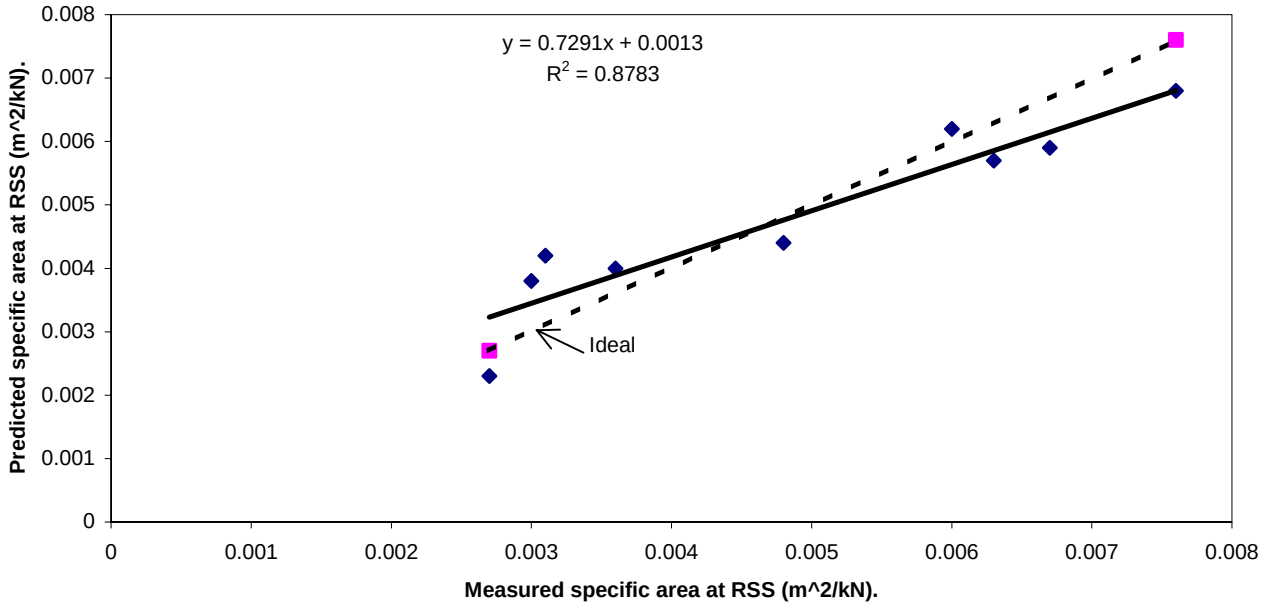

Figure 6.22 : Comparison of measured and predicted specific area at RSS based on the proposed model.

6.5.3 Prediction of forces acting on the front subsoiler.

To predict the draft and vertical force requirements of the front subsoiler, the Swick and Perumpral (1988) model was used. Appendix E presents the coded computer program to solve this model.

It should be noted that the experimental verification of the Swick-model was conducted at very shallow operating depths ranging from 52 to 152 mm. In this case, the operating depth of the front subsoiler ranged from 410 to 510 mm.

In figure 6.23, the experimentally measured draft forces at the front subsoiler, are compared with those predicted. The data presented consists of all the data collected at different spacings and operating depths of the front subsoiler. The figure therefore presents the overall performance of the Swick-model. The fitted least square regression has a reasonable slope and a coefficient of determination.

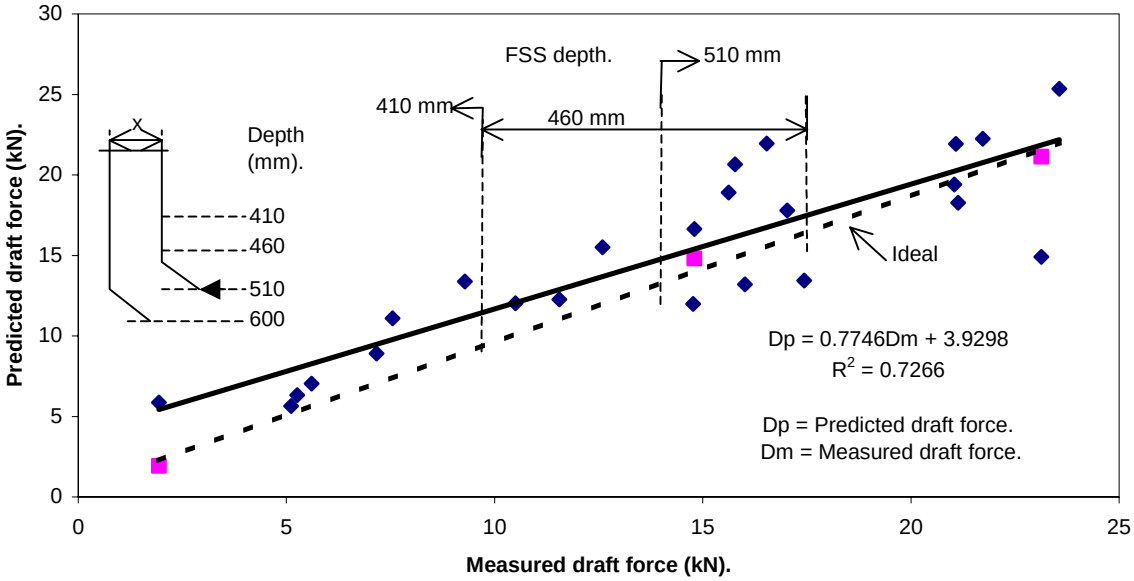

Figure 6.23: Comparison of measured and predicted draft force at the front subsoiler based on the Swick-model. (x = 300, 420, 540 & 790 mm).

The computer output of the analysis of variance, for the relationship data between measured and predicted draft force, is presented in table 6.1.

Table 6.1: Analysis of Variance for Prediction-Data of the Draft Force at the Front Shank.

The REG Procedure
Model: MODEL1
Dependent Variable: y y

Analysis of Variance

Source	DF	Sum of Squares	Mean Square	F Value	Pr > F
Model	1	534.12640	534.12640	58.46	<.0001
Error	22	201.01761	9.13716		
Corrected Total	23	735.14402			

Root MSE	3.02277	R-Square	0.7266
Dependent Mean	14.98917	Adj R-Sq	0.7141
Coeff Var	20.16639		

Parameter Estimates

Variable	Label	DF	Parameter Estimate	Standard Error	t Value	Pr > |t|
Intercept	Intercept	1	4.28709	1.52971	2.80	0.0104
x	x	1	0.73719	0.09642	7.65	<.0001

From this table 6.1, the p-values for the slope and intercept are <0.0001 and 0.0104, and R-square is 0.73. This means both the slope and the intercept are significant with a good coefficient of determination. Apart from experimental random errors, the significant

intercept can be attributed to the fact that the model over predicts the applied draft force. This is due to the model over predicting the rupture radius and the maximum width of the failed-profile thus over predicting the disturbed volume of soil. This model would have greatly over predicted the draft force had it accounted for the energy dissipated during soil pulverization.

The model was further evaluated at specific subsoiler spacing-ranges influencing soil-failure patterns of the two subsoilers. Table 6.2 presents the spacing-ranges and their limit values in each spacing range. The aim was to establish the spacing-range in which the model was most efficient. Figures 6.23a, b and c present the model performance at these spacing-ranges i.e. the data used is for spacings falling within the respective range.

Table 6.2: Possible values of R_z and t at different spacing ranges and depth of the FSS.

Spacing Range.	Spacing, x (mm).	FSS Depth (mm).	R_z (mm).	t (mm).
$x < R_z$	300	410	520	-
	300	460	390	-
	420	410	520	-
$R_z <= x < t$	300	510	250	310
	420	460	390	520
	540	410	520	640
$x > t$.	420	510	-	310
	540	460	-	480
	540	510	-	310
	790	410	-	640
	790	460	-	480
	790	510	-	310

- *The distance t is shown in figure 3.2.1 and defined by equation 3.27.*
- *The distance R_z is shown in figure 3.1 and defined in section 3.1.*

From table 6.2, it is clear that R_z and t reduced as the working depth of the front subsoiler increased. To remain within the required spacing-range, there were possible depths for the FSS as indicated in table 6.2. A dash in the table indicates that the value of R_z or t is not applicable in that particular spacing-range. The performance of the model in these ranges is as follows:

a). The spacing x less than R_z.

Figure 6.23a presents the comparison of measured and predicted forces at the front subsoiler when the spacing was less than R_z. The regression line fitted on the data has an acceptable slope with the data correlated very well. However the intercept is significant.

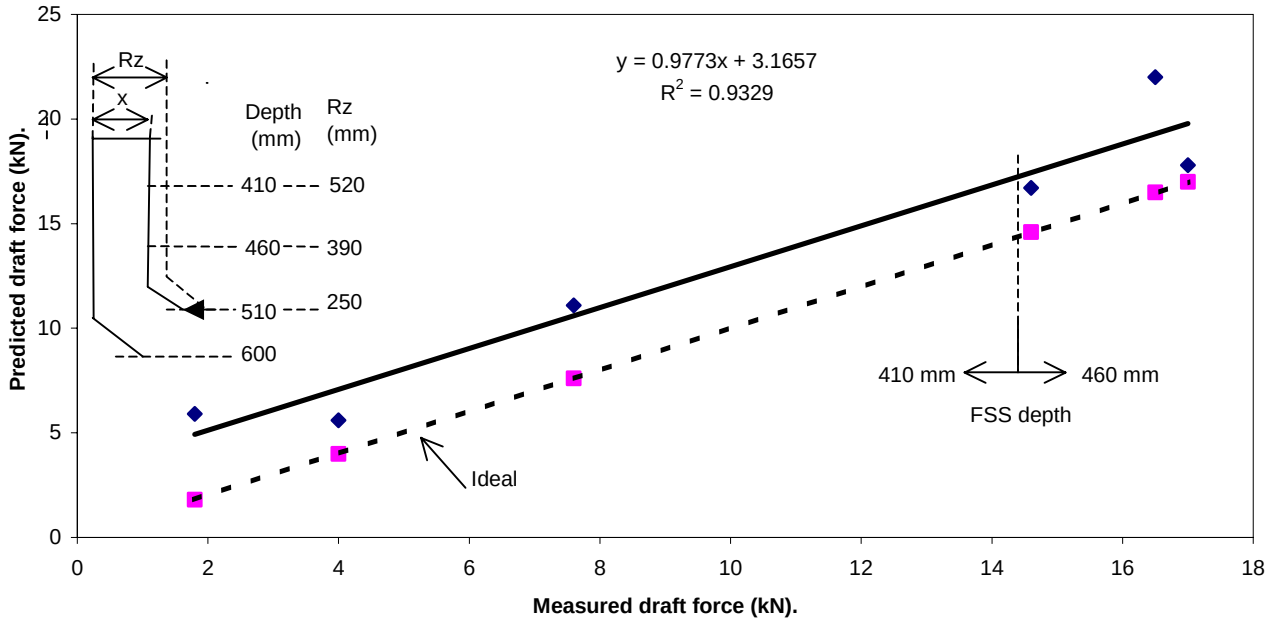

Figure 6.23a: Comparison of measured and predicted draft force at FSS when x<Rz based on the Swick-model.

The following spacing fall within this range: x =300 mm (R_z = 410 and 460 mm) and x = 420 mm (R_z = 520 mm). At all these settings, the two subsoilers are longitudinally close with adequate vertical spacing to allow the rear subsoiler to do most of the cultivation. This leads the model to over predict the draft force exerted by the front subsoiler. The model over prediction pushed the regression line up, partly accounting for the intercept in this region.

b). The spacing x ranges between R_z and t.

Figure 6.23b presents a similar relationship when the spacing ranges between R_z and t. The data correlated very well in this range and regression line has a reasonable slope with a significant intercept.

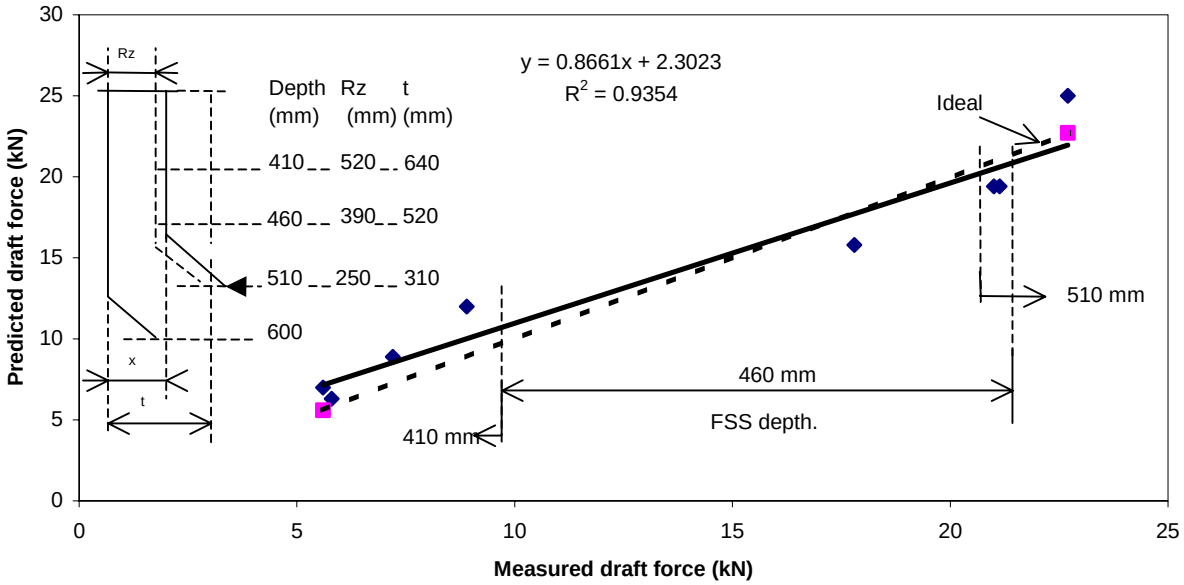

Figure 6.23b: Comparison of the measured and predicted draft force at the FSS when Rz < x < t based on the Swick-model.

In this range, the following were the possible spacings: x = 300 mm (t = 310 mm), x = 420 mm (t = 520 mm) and x = 540 mm (t = 690 mm). A spacing of 300 mm allowed FSS to be set at 510 mm deep to remain in the spacing-range therefore the two subsoilers were both horizontally and vertically close. Thus the front subsoiler did most of the tilling resulting in the model to slightly under predict the exerted draft force to the extreme right of figure 6.23b.

At 420 mm spacing, the FSS operated at 460 mm deep allowing both subsoilers to till independently. Hence the model adequately predicted the applied draft force. When the spacing was increased to 540 mm, the FSS could only be set at 410 mm deep to remain within this range. Again this setting allowed both subsoilers to operate independently leading the model to adequately predict the draft force required by the FSS.

c). The spacing x is greater than t.

The model performance in this region is presented by figure 6.23c. The regression line has both a reasonable slope and R-square value with a significant intercept.

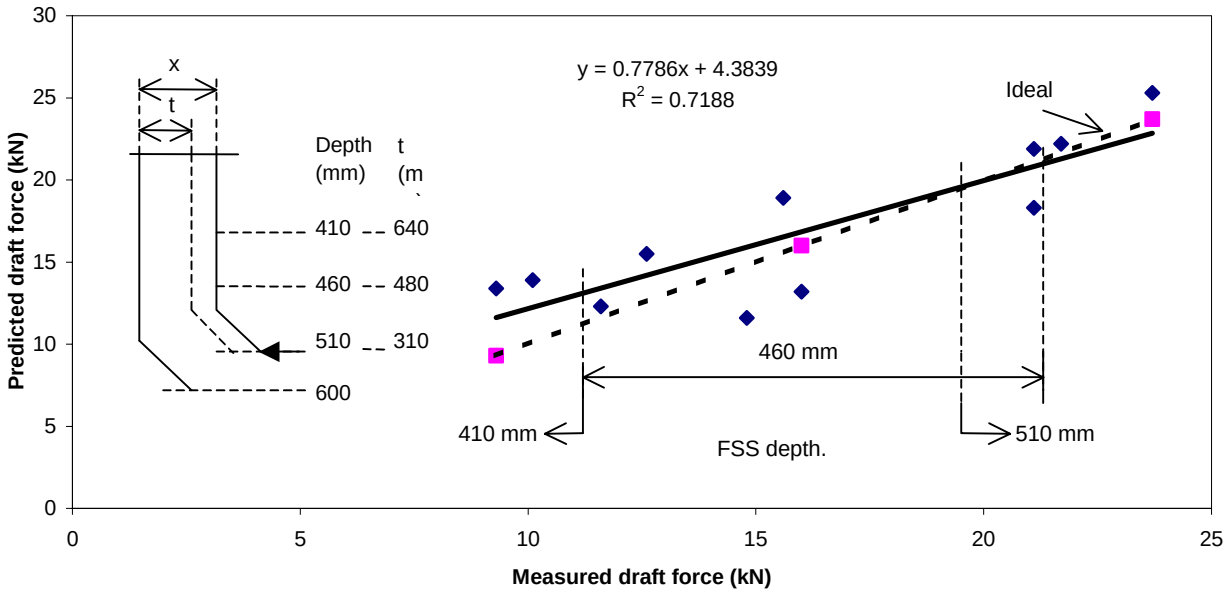

Figure 6.23c: Comparison of the measured and predicted draft force on the FSS when the spacing x > t based on the Swick-model.

In this region, the following were the possible spacings: x = 540 mm (t = 480 mm) and x = 790 mm (t = 310, 480 and 790 mm). At a spacing of 540 mm, the FSS could be set at 460 mm deep and this setting allowed each subsoiler to operate independently. Thus the model reasonably predicted the applied draft force. The FSS could be operated at all the three possible depth-positions when the spacing was increased to 790 mm. At this spacing each subsoiler operated independent of each other, however the model slightly over predicted and under predicted the draft force at the FSS-operating depth of 410 and 510 mm respectively.

Apart from a significant intercept recorded by the Swick-model at each spacing-range, the graph-slopes and R-square values were very good in all the three cases. Further more, even though the Swick-model over predicted the tilled cross-section area and volume, the measured and predicted draft force values were reasonably close.

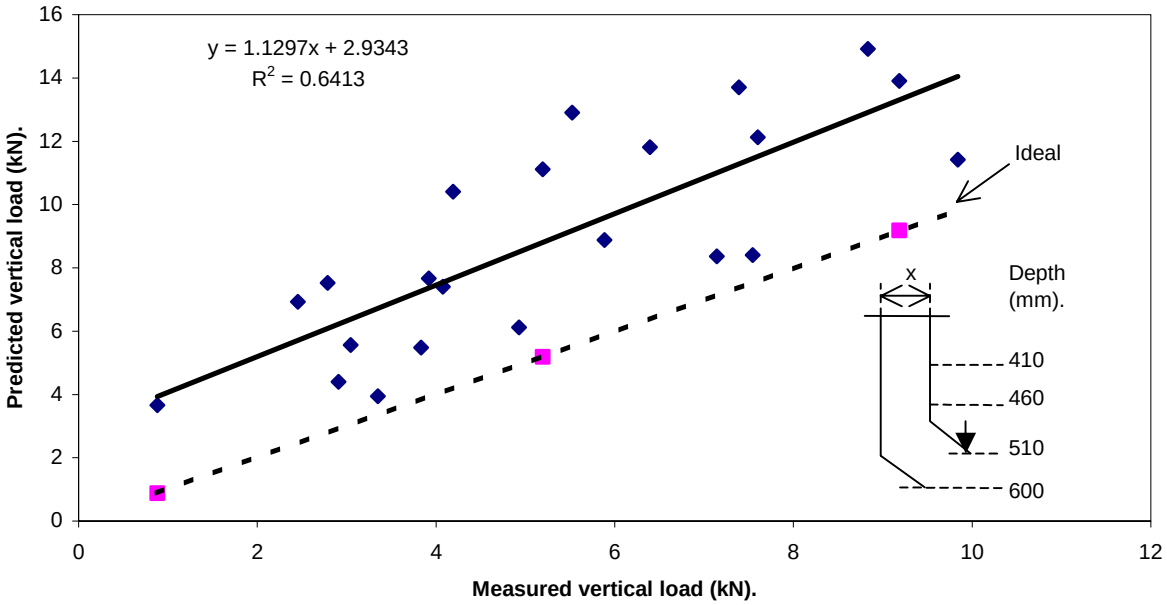

Figure 6.24: Comparison of measured and predicted vertical load at the front subsoiler based on the Swick-model.

The relationship between the measured and predicted vertical soil forces is presented by figure 6.24. This figure presents the overall model performance since the data used is for the different spacing and operating depths of the front subsoiler.

Table 6.3: Variance Analysis for Prediction-Data of the Vertical Load at the Front Shank.

The REG Procedure
Model: MODEL1
Dependent Variable: y y

Analysis of Variance

Source	DF	Sum of Squares	Mean Square	F Value	Pr > F
Model	1	157.40307	157.40307	35.76	<.0001
Error	20	88.03686	4.40184		
Corrected Total	21	245.43993			

Root MSE	2.09806	R-Square	0.6413
Dependent Mean	8.93777	Adj R-Sq	0.6234
Coeff Var	23.47405		

Parameter Estimates

Variable	Label	DF	Parameter Estimate	Standard Error	t Value	Pr > |t|
Intercept	Intercept	1	2.93431	1.09909	2.67	0.0147
x	x	1	1.12973	0.18892	5.98	<.0001

Table 6.3 presents the computer output of the analysis of variance for the measured versus the predicted vertical loading data at the front subsoiler. The p-values of the slope and the intercept is <0.0001 and 0.0147 respectively. From these p-values, both the slope and the intercept are significant.

The model was further evaluated at the following spacing-ranges, influencing the soil-failure pattern for both subsoilers:

a). The spacing x less than Rz.

The relationship between measured and predicted vertical forces is presented in figure 6.24a. The regression line has a slope and an intercept of 1.96 and 1.11 respectively with a coefficient of determination of 0.89. Like the draft force, the vertical loading in this region is also totally over predicted. Again it is attributed to the fact that the subsoilers are close to each other, thus the rear subsoiler carries some of the vertical load.

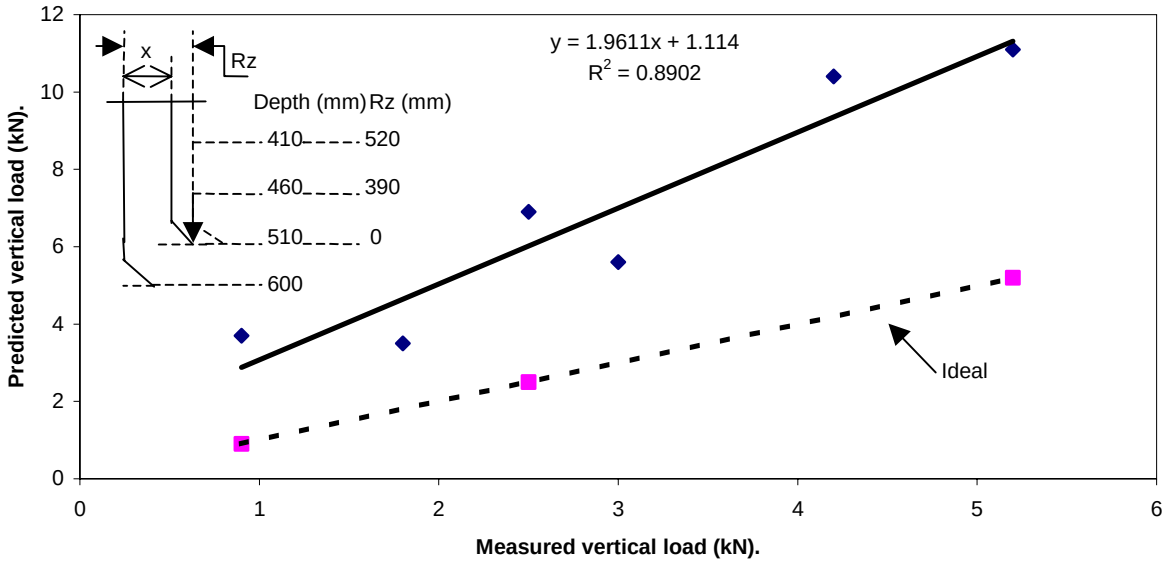

Figure 6.24a: Comparison of measured and predicted vertical load at FSS when the spacing x < Rz based on the Swick-model.

b). The spacing x ranges between R_z and t.

Figure 6.24b compares the measured and predicted vertical forces at the spacing ranging between R_z and t. The fitted regression line has a slope and an intercept of 1.28 and 1.57 respectively with R-square equal to 0.74. Again the model over predicts the vertical loading in this region. At this spacing, there is limited overlapping of the failed soil-wedges thus the rear subsoiler carries some of the vertical load.

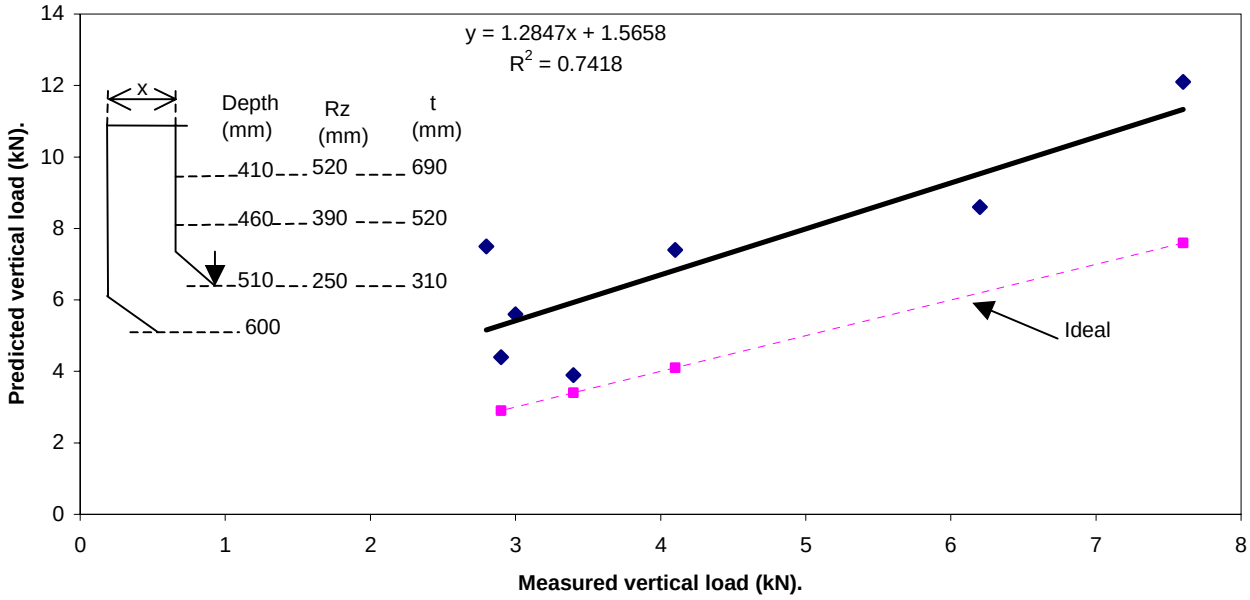

Figure 6.24b: Comparison of measured and predicted vertical load at FSS when Rz<x<t based on the Swick-model.

c) The spacing x>t.

Figure 6.24c presents the model performance when the spacing is greater than t. In this case, the regression line has a slope and an intercept of 1.12 and 2.6 respectively with a coefficient of determination equal to 0.58. At this spacing, the model over predicts the vertical force acting on the front subsoiler. Since at this spacing, the front subsoiler is not influenced by the rear subsoiler, the over prediction is probably due to general variability in the soil and the tendency of analytical models to over predict the soil volume failed.

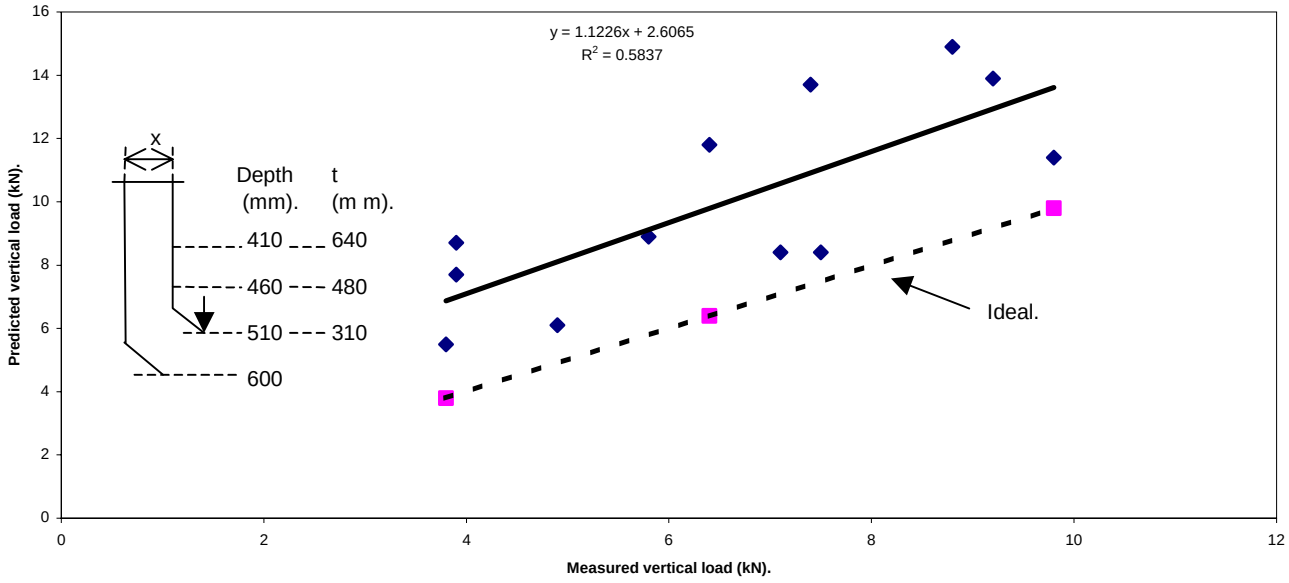

Figure 6.24c: Comparison of measured and predicted vertical load at FSS when the spacing x>t.

6.5.4 Prediction of the forces acting on the rear subsoiler.

To predict force components acting on the rear subsoiler, the proposed model was used. In this model equation 6.2 was used to determine the maximum width of the side circular wedge of the failed soil-profile. The rupture radii for both subsoilers were determined from the maximum cross-section area of the failed-profiles. This was done because as noted above, Swick and Perumpral's model was over predicting both the width and the rupture radius of a failed soil-profile. In practice the failed cross-section area and the rapture radius were much smaller. Furthermore, as mentioned earlier, 30% of the draft force required to till a unit cross-section area (m^2) by a moldboard plough was included in the proposed model to account for energy required for soil pulverization.

The comparison of the experimentally measured and predicted draft forces by the proposed mathematical model is presented in figure 6.25. This is the overall

performance of the proposed model for the rear subsoiler since the data used, is for all the different spacing and operating depths of the front subsoiler.

The presented least square regression has a reasonable slope and coefficient of determination since they both are not very significant from one.

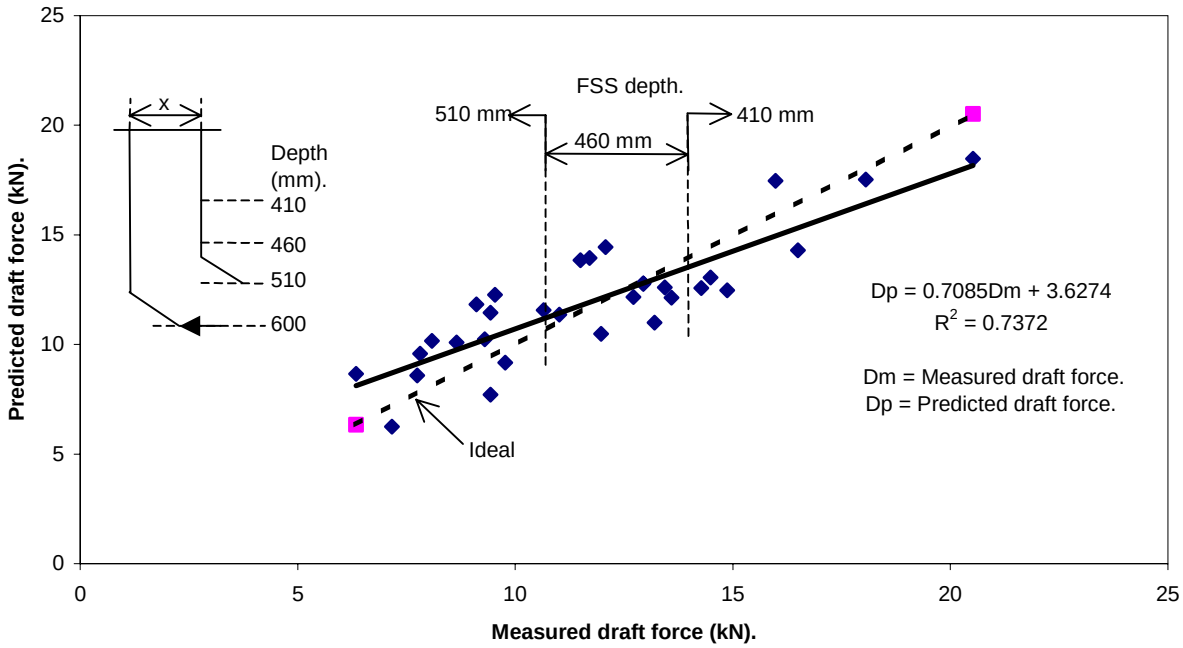

Figure 6.25: Comparison of measured and predicted draft force at the rear subsoiler (RSS) based on the proposed model.

Table 6.4: Variance Analysis for Prediction-Data of the Draft Force at the Rear Shank.

The REG Procedure
Model: MODEL1
Dependent Variable: y y

Analysis of Variance

Source	DF	Sum of Squares	Mean Square	F Value	Pr > F
Model	1	167.34283	167.34283	84.15	<.0001
Error	30	59.66176	1.98873		
Corrected Total	31	227.00459			

Root MSE	1.41022	R-Square	0.7372
Dependent Mean	11.99063	Adj R-Sq	0.7284
Coeff Var	11.76104		

Parameter Estimates

Variable	Label	DF	Parameter Estimate	Standard Error	t Value	Pr > |t|
Intercept	Intercept	1	3.62743	0.94518	3.84	0.0006
x	x	1	0.70849	0.07724	9.17	<.0001

The computer software output for this data is presented in table 6.4. The p-values for the slope and intercept are <0.0001 and 0.0006 respectively indicating that the slope is significant while the intercept is not very significant but acceptable.

The model was evaluated at the following different spacing ranges that influence the soil-failure pattern with the aim of establishing the range in which the model is most efficient.

a). The spacing x less than R_z.

The model performance within this region is presented in figure 6.25a. The regression line has a slope and an intercept of 0.82 and 1.4 respectively with a coefficient of determination equal to 0.77.

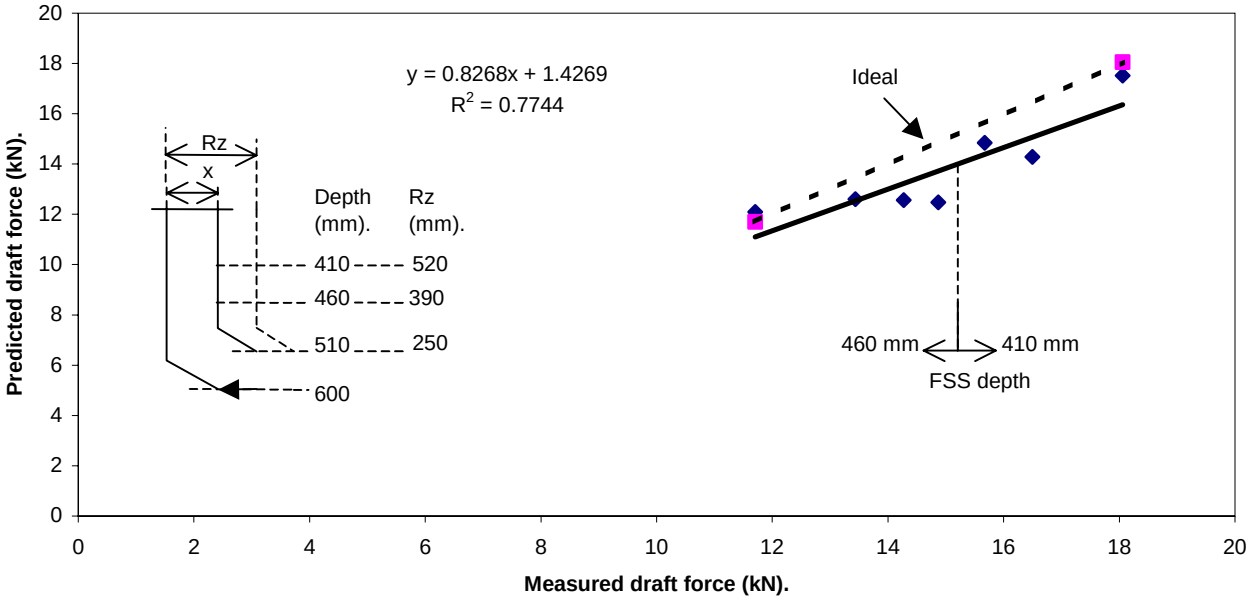

Figure 6.25a: Comparison of measured and predicted draft force at RSS when the spacing x<Rz based on the proposed model.

The spacings falling within this range are: x = 300 mm (R_z = 410 or 460 mm) and x = 420 mm (R_z = 410 mm). At such settings, the rear subsoiler did most of the tilling as the two subsoilers were longitudinally close to each other with a reasonable vertical distance between them. This resulted in the model under predicting the soil volume failed by the rear subsoiler and the failure surface hence under predicted the applied

draft force. This scenario resulted in the model to slightly under predict the applied draft force in this range (fig.6.25a).

b). The spacing x ranges between R_z and t.

The model performance in this range is presented in figure 6.25b. The slope of the regression line and an intercept of 0.7 and 3.4 respectively with R-square equal to 0.78.

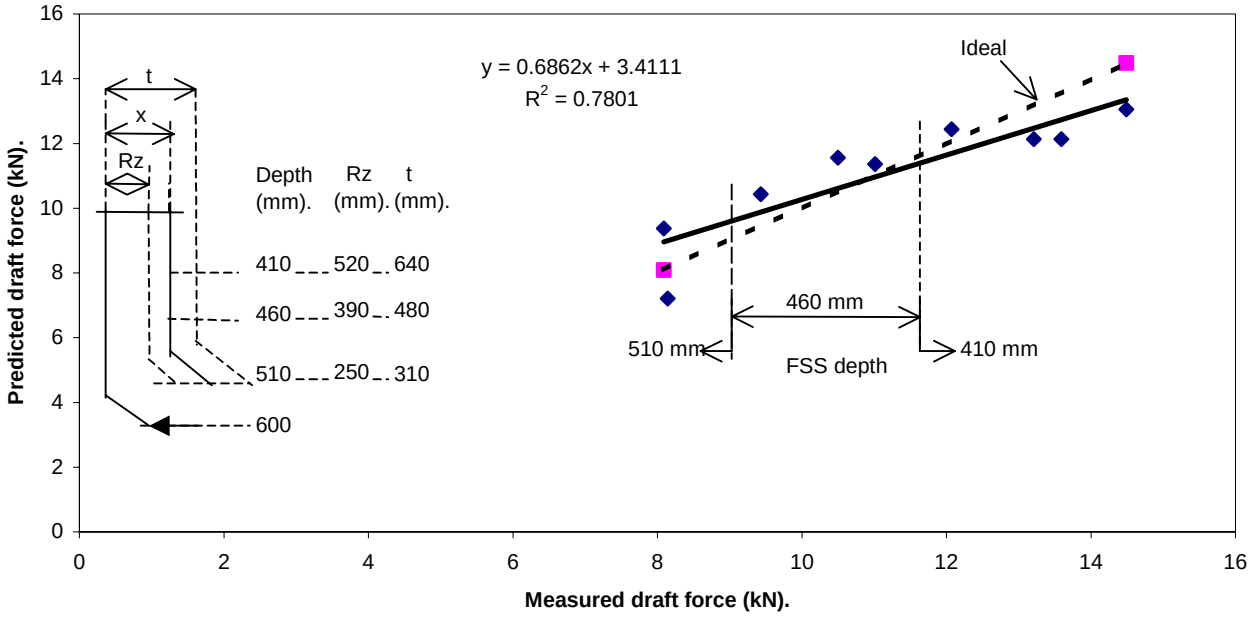

Figure 6.25b: Comparison of measured and predicted draft force at RSS when the spacing Rz<=x<t based on the proposed model.

The spacings falling within this range are: x = 300 mm (t = 310 mm), x = 420 mm (t = 480 mm) and x = 540 mm (t = 480 mm).

At the spacing of 300 mm with an operating depth of 510 mm for the FSS, the front subsoiler did most of the tilling since the vertical distance between them, was small (90 mm). Thus the model over predicted the draft force requirements of the rear subsoiler.

When the spacing was increased to 420 mm, the front subsoiler could only be set at a depth of 460 mm in this range. At this setting, its influence to the front subsoiler was reduced, thus the model correctly predicted its draft force requirements. At an increased spacing of 540 mm, the front subsoiler could be set at a depth of 460 mm. Both the

horizontal and vertical spacing between them, allowed the rear subsoiler to till without influence from the front subsoiler. The model therefore almost predicted the exerted draft force.

From the above, the overall performance of the model in this range indicates that the applied draft force was under predicted when the FSS was set at a depth of 410 mm, adequately predicted it when the FSS was set at 460 mm and over predicted when the FSS was set at 510 mm (fig.6.25b).

c). The spacing x>t.

The model performance when the spacing x is greater than t is presented in figure 6.25c. The spacings falling within this range are: x = 420 mm (t = 310 mm), x =540 mm (t = 310, 480 mm) and x = 790 mm (t = 640, 480, 310 mm). The same observations were made as above when the operating depth of the FSS was varied in the three positions. This resulting in the model to under predict the applied draft force when the FSS was set at a depth of 410 mm and it was adequately predicted when FSS was set at 460 mm and over predicted when the FSS was set at 510 mm (fig.6.25c).

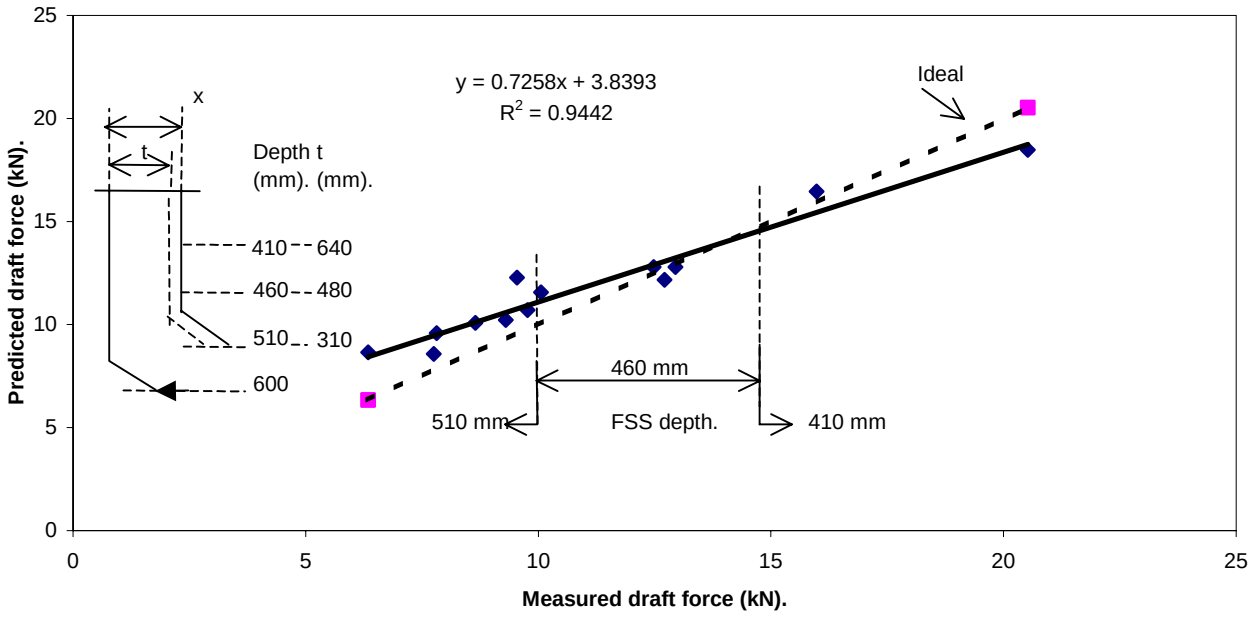

Figure 6.25c: Comparison of measured and predicted draft force at RSS when the spacing x>t based on the proposed model.

Comparing the three spacing ranges considered above, it is clear that the draft force-data correlation was acceptable but the slope was not so good when spacing ranged between R_z and t (fig. 6.25b). In all the cases, the intercept was significant therefore the model was most efficient at spacing less than R_z and greater than t.

A similar least square regression for the relationship between the measured and predicted vertical loading at the rear subsoiler is presented by figure 6.26. From the computer software output for this data presented in table 6.5, its slope and the coefficient of determination are reasonable, but the vertical intercept is significant. This significant intercept is due to over prediction of the lower vertical force values when the front subsoiler carried much of the load. The proposed model adequately predicted the vertical load on the rear subsoiler when the spacing allowed each subsoiler to till independently.

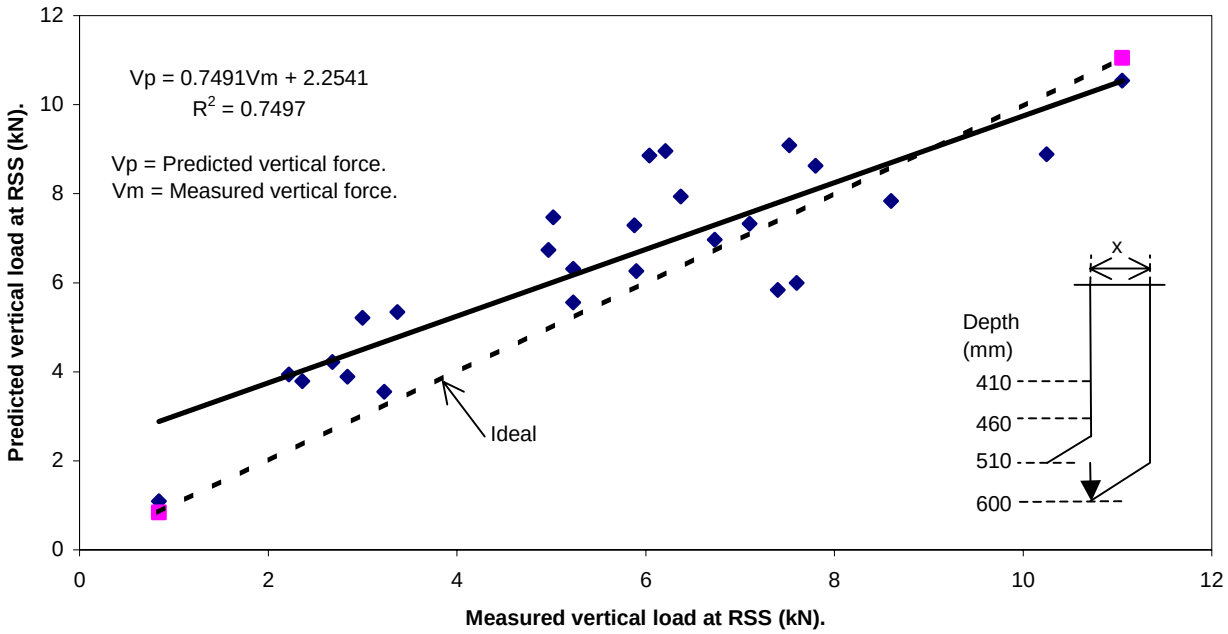

Figure 6.26: Comparison of measured and predicted vertical force at RSS based on the proposed model. (x = 300, 420, 540 & 790 mm).

Table 6.5: Variance Analysis for Prediction-Data of the Vertical Force at the Rear Shank.

Analysis of Variance

Source	DF	Sum of Squares	Mean Square	F Value	Pr > F
Model	1	67.63481	67.63481	94.81	<.0001
Error	24	17.12041	0.71335		
Corrected Total	25	84.75522			

Root MSE	0.84460	R-Square	0.7980
Dependent Mean	4.24615	Adj R-Sq	0.7896
Coeff Var	19.89096		

Parameter Estimates

Variable	Label	DF	Parameter Estimate	Standard Error	t Value	Pr > |t|
Intercept	Intercept	1	-1.08133	0.57165	-1.89	0.0707
x	x	1	0.81164	0.08335	9.74	<.0001

The model was evaluated at the following three different subsoiler spacing at which the field tests were conducted:

a). The spacing $x<R_z$.

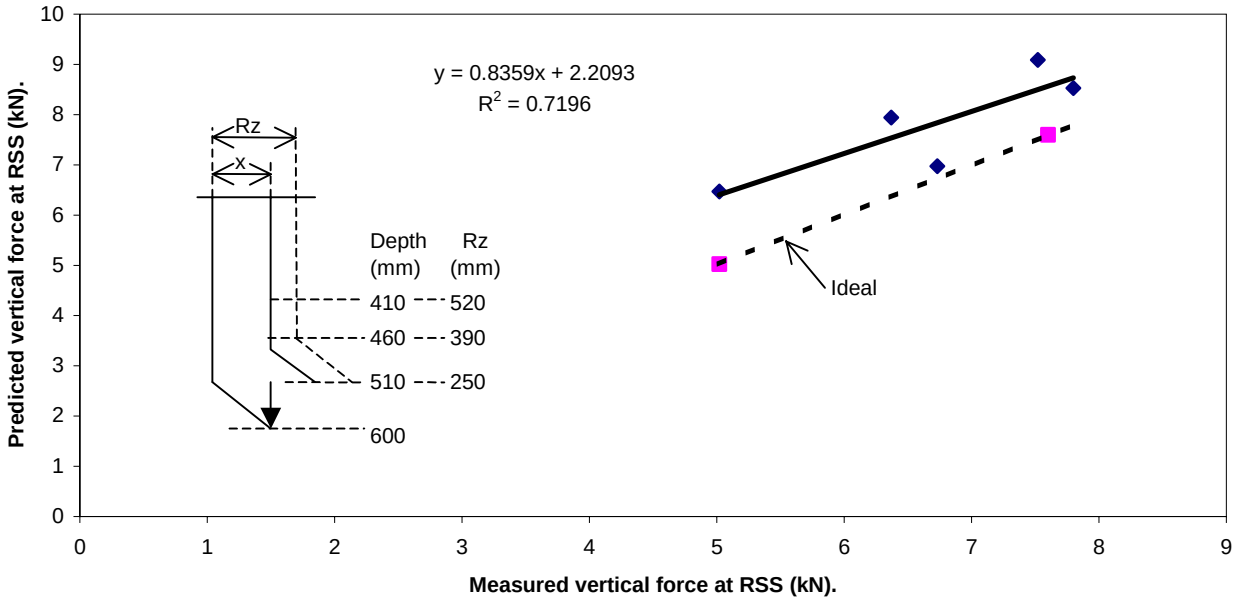

Figure 6.26a: Comparison of measured and predicted vertical force at RSS when the spacing x<Rz based on the proposed model.

The model performance within this spacing is presented by figure 6.26a. The regression line-slope is not very different from one with a reasonable R-square. However its intercept is significant due to over prediction in this range. The proposed model over predicted the vertical load on the rear because at this spacing the front subsoiler carried most of the weight.

b). The spacing x ranges between R_z and t.

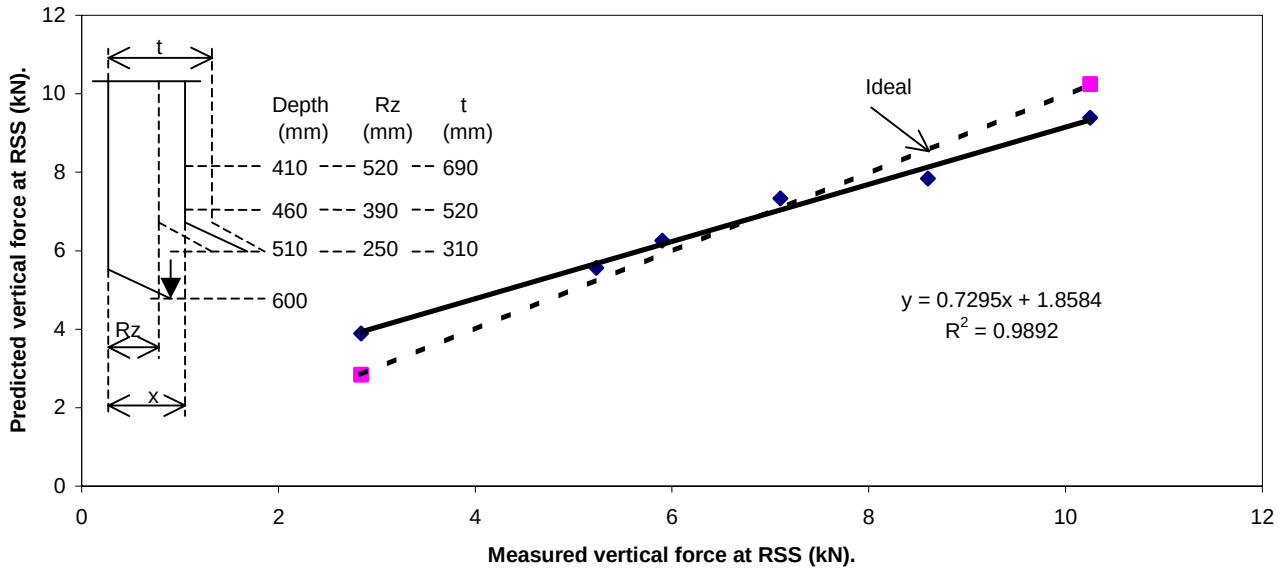

Figure 6.26b: Comparison of measured and predicted vertical force when the spacing Rz<x<=t based on the proposed model.

The model performance at this spacing is presented by figure 6.26b. The regression line-slope is reasonable and the data well correlated in this spacing range. The vertical intercept is not very significant. The proposed model adequately predicted the vertical load on the rear subsoiler.

c). The spacing x>t.

The model performance in this spacing range is presented by figure 6.26c. The slope of the regression line and R-square value are very good with an intercept not very significant. The proposed model therefore adequately predicted the vertical loading in this range.

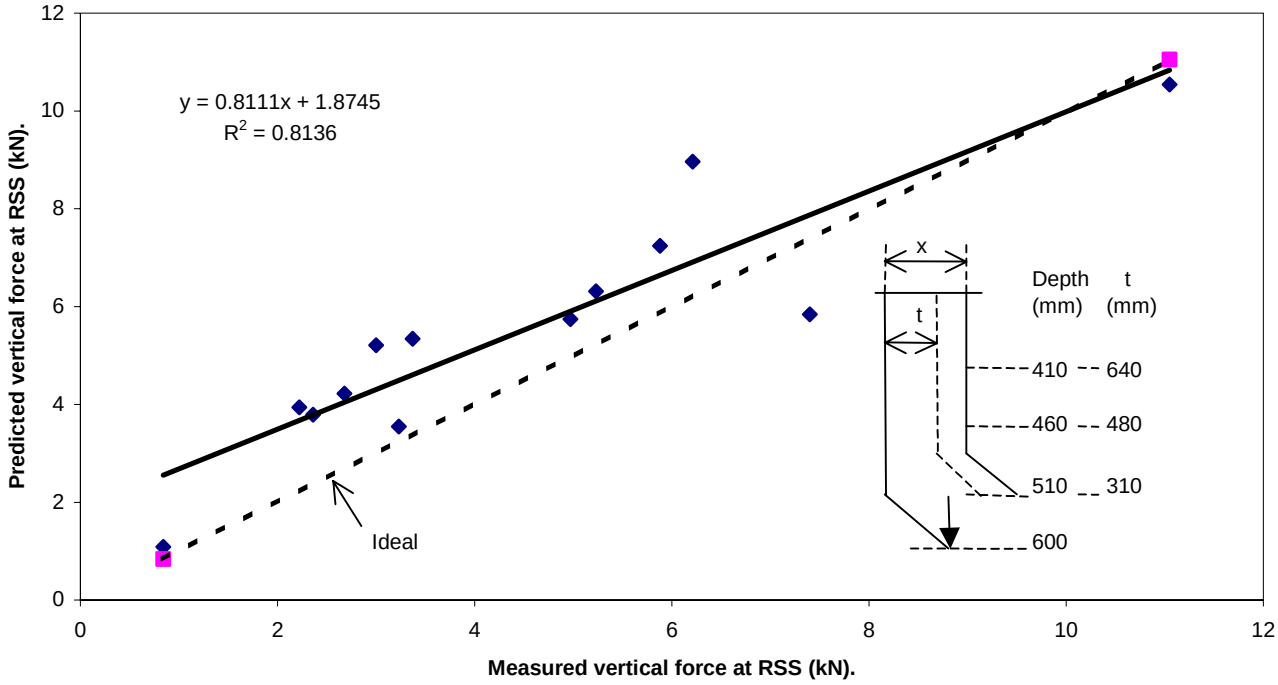

Figure 6.26c : Comparison of measured and predicted vertical force at the RSS when the spacing x>t based on the proposed model.

Comparing the three spacing-ranges considered above, the proposed model was most efficient at spacings greater than Rz.

6.5.5 Identification of factors causing the error.

The overall performance of both models had significant intercepts. In an effort to determine the cause, the residue (difference between measured and predicted values) for the relationship between measured and predicted draft force at the rear subsoiler, was plotted versus the measured draft-force values. This plot is presented in figure 6.27 and it reveals no obvious pattern, thus nothing unusual with the predicted data. The intercept therefore is attributed to both experimental random errors and the tendency for the models to over predict the draft and vertical forces at close spacing.

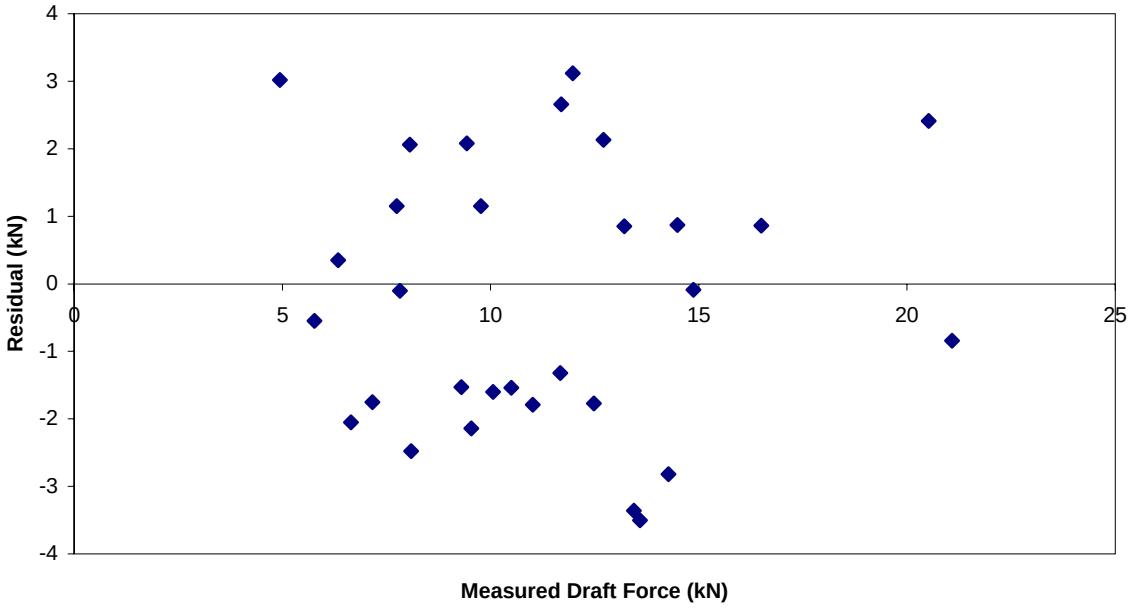

Figure 6.27: Residual versus the measured draft force at the rear subsoiler.

6.5.6 Prediction of the total draft force acting on both subsoilers.

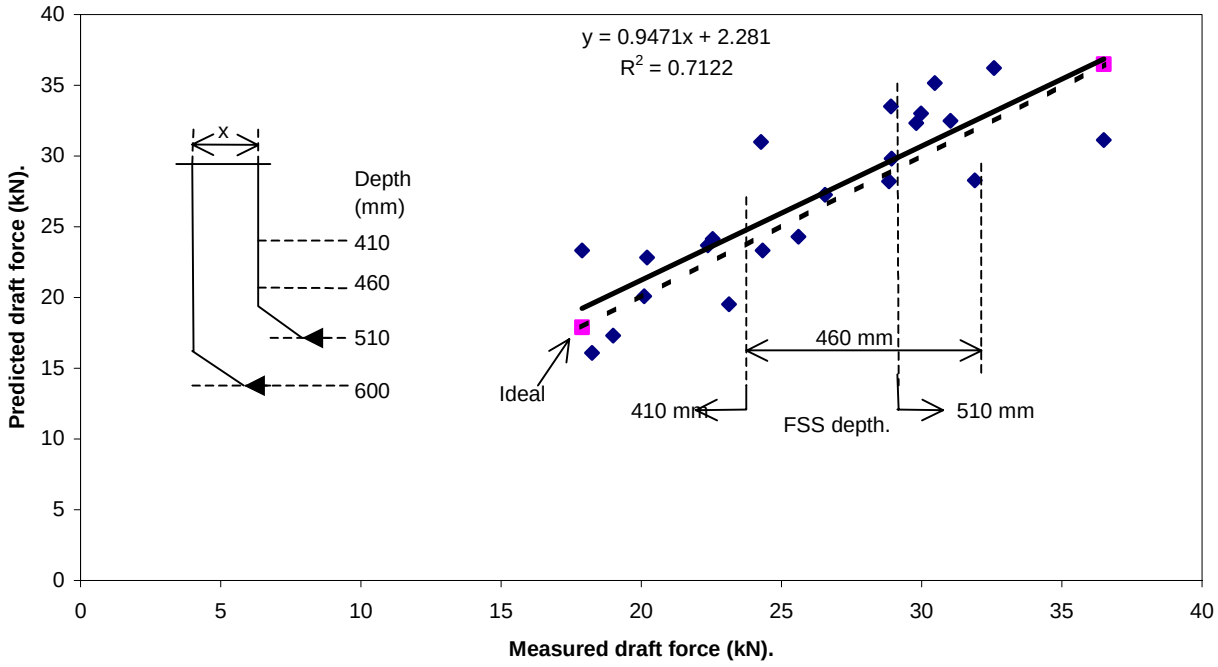

Figure 6.28 : Comparison of measured and predicted total draft force at the two subsoilers. (x = 300, 420, 540, 790mm)

The summation of the predicted draft force at the front and rear subsoilers versus the total measured draft force is presented by figure 6.28. The fitted regression line has a slope and a R-square value that are not very different from one. However its vertical intercept is significantly from zero. Since the Swick-Perumpral model over predicted the draft force at shallow operating depth of the front subsoiler and the proposed model slightly under predicted it at the RSS, their summation therefore resulted in over predicting the same values, thus causing the intercept.

6.6 Energy optimization.

6.6.1 Longitudinal spacing of the subsoilers

To establish the longitudinal spacing, at which energy utilization is optimal, the maximum cross-section area failed per unit draft force (specific area) was evaluated at different spacing at the three depth-levels of the front subsoiler. Figure 6.29 presents the relationship of the specific area with the spacing at the three depth-levels of the front subsoiler. In all the three cases, the specific area linearly improved as the spacing was increased and it also improved as the depth of front subsoiler was increased.

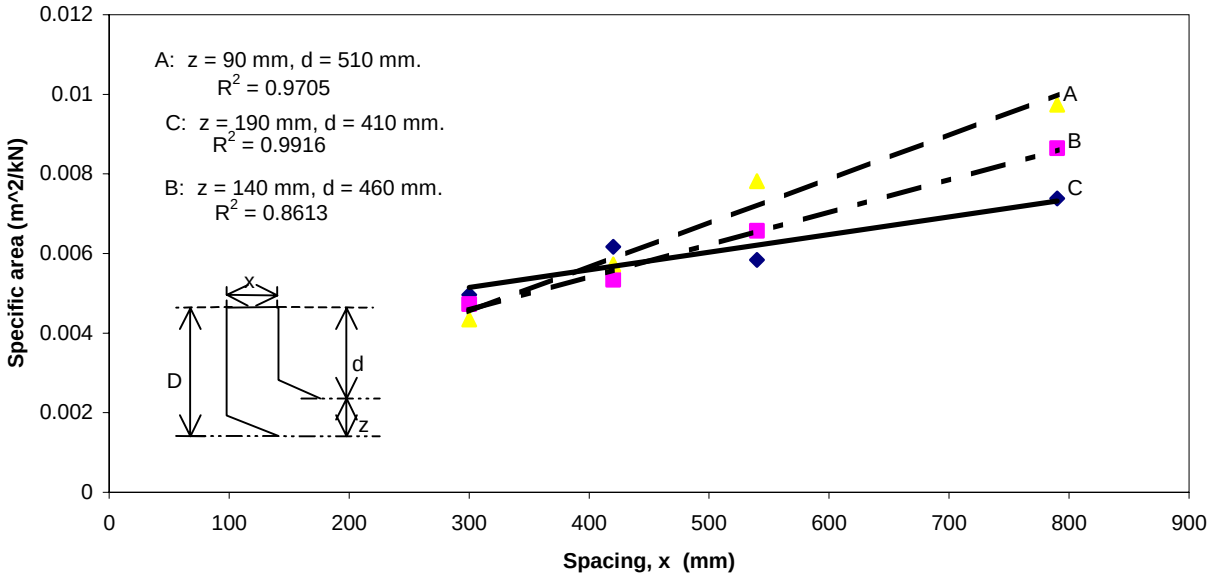

Figure 6.29: Failed cros-section area per unit draft force versus spacing at different operating depths of FSS (D = 600 mm).

6.6.2 Optimum depth of the front subsoiler.

To determine the optimum depth of the front subsoiler at which the specific area is maximized, it was plotted against the ratio of the effective depth (z) of the rear subsoiler to that of the front subsoiler (d). Since it was noted in figure 6.30 that energy utilization improves with increased spacing, it follows that subsoilers in tandem are more efficient at a spacing that allows the soil from the front subsoiler to stabilize before the rear subsoiler reaches it. Such a longitudinal spacing corresponds to x equal to or greater than t where t is defined by equation 3.27. The data used in figure 6.30, was therefore for spacing equal or greater than t.

Figure 6.30 presents this plot with the data best fitted by a polynomial of the second degree. By minimizing this polynomial, the cross-section area failed per unit draft force was found to be maximized at a ratio (z/d) of 0.26. It means therefore that the optimum depth (dop) for the front subsoiler at which energy utilization is maximized, can be expressed as follows:

$d_{op} = 0.8D$ ……6.5.

Where:

d_{op} = Optimum depth of the front subsoiler (m).

D = The operating depth of the rear subsoiler (m).

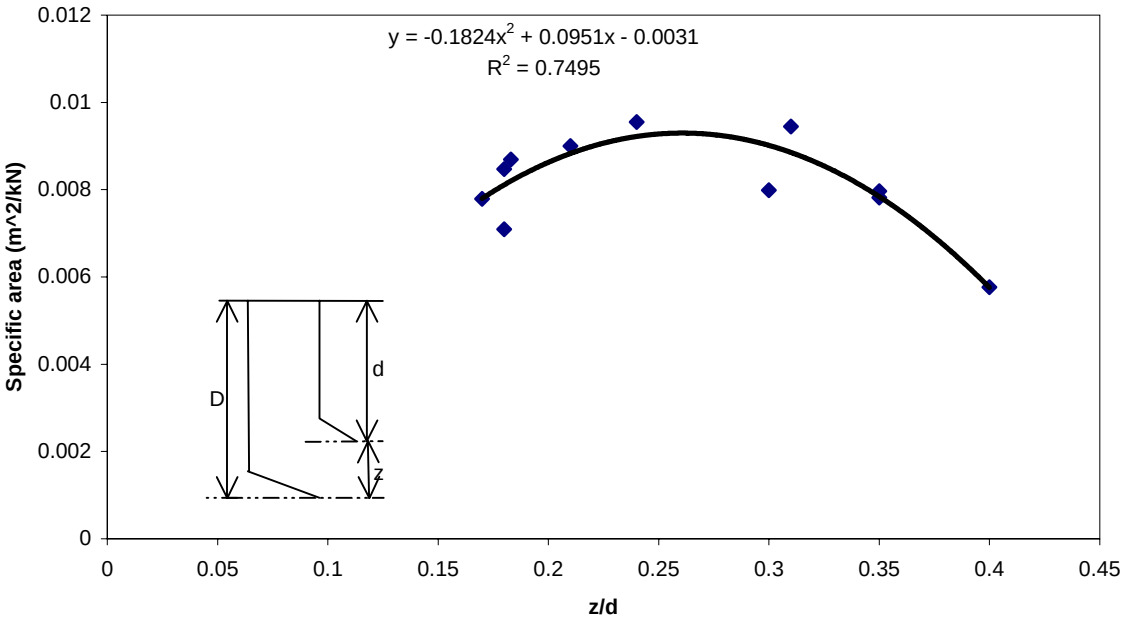

Figure 6.30: Comparison of failed cross-section are per unit draft force versus the ratio of z to d.

CHAPTER VII

7. SUMMARY, CONCLUSIONS AND RECOMMENDATIONS.

7.1 Summary.

From the literature, it was possible to use the principles of basic equilibrium-analysis to develop a mathematical model for predicting the vertical and draft force requirements of the rear subsoiler. At the same time, the proposed model was also able to predict the volumes of the three-dimensional and thus the maximum cross-sectional areas of the soil-profiles tilled.

Further more, it has been ascertained that the tested model for a single tine can predict force requirements of the front subsoiler in a tandem configuration. The relative position of the front subsoiler at which energy utilization is optimized, has also been established.

Considering soil non-uniformity and the difficulties associated with obtaining accurate measurements of soil parameters under field conditions, the performance-results of the models are promising.

7.2 Conclusions

In conclusion, it has to be pointed out that even though some soil characteristics such as bulk density vary with depth from the soil surface, the bulk density value used was the average measured up to a depth of 600 mm and it was at the soil water content of 9.15% db. The bulk density did not increase much with depth, as stated by Hartge (1988), but for certain tests it even decreased, probably due to the tillage history of the land. The last primary tillage of the land was undertaken several years ago when grass was sown for grazing by sheep and production of baled hay.

At the same time, circumstances forced the researcher to conduct the field tests in sandy clay loam soil, which may not be as prone to compaction as the fine sandy soils. Since the data was collected under field conditions, it was not possible to record them at constant specified soil water content, but a range of plus-minus ten percent variation from 9.15% db (8.25% – 10.10%) was maintained. Most of the data was recorded at a moisture content falling within the above range. Only data within this range was used for testing the force model. Data outside the range of soil water contents was used to determine the influence of soil water content on the width of the failed side crescent, for the rear subsoiler tilling up to 600 mm deep.

Based on the results from the field experiments and the performance of the analytical force models, the following conclusions were drawn:

1. The developed two-dimensional transducer system, fitted to the tillage dynamometer, adequately measured soil reacting forces on each subsoiler.

2. At close spacing, the point of soil-failure at the FSS was in phase with the commencement of soil compression at the RSS, leading to reduced total draft force requirements for both subsoilers. However, at wider longitudinal spacing, the above soil-failure pattern was out of phase, resulting in increased total draft force requirement. Further more, wider spacing recorded a larger cross-sectional area tilled per unit draft force. This was because the tilled cross-sectional areas at a wider spacing increased faster in size than the draft force. This increase was probably due to a reduction of β_r as the vertical load on the RSS reduced. At increased spacing, the pulverized soil by the FSS exerts less weight on the RSS than it would if the soil was undisturbed with the FSS close to the RSS. From equation A12 (Appendix A), it was established that as the overburden on the RSS reduced, β_r also reduced, thus increasing the size of the tilled cross-section area and the soil volume.

3. A technique using an automatic penetrometer with a computer program was developed to measure the cross-sectional areas and map the three-dimensional

failed-profiles. This technique was successful and indicated that the subsoiler failed the soil beyond its working depth and blade width. It was also in agreement with the spiral surface-failure theory, sited in the literature. This spiral failure surface originated from the tip of the rear subsoiler, extending below its working depth and reached the surface with a larger angle β than for the model with a flat failure plane. This explains why the accepted flat plane of the failed soil-profile, as quoted in the literature, was found to be quite different from the actual curved plane. However, this penetrometer technique was too time consuming and it was discontinued for the rest of the experiments.

4. In the proposed soil force model, the maximum width of the side circular-wedge was expressed as a function of soil water content. This resulted in the model adequately predicting the maximum cross-sectional areas and thus total soil-volumes of the failed-profiles. In addition, the model accounted for energy dissipated by soil pulverization and over coming the frictional forces acting on the sides of the subsoiler. This enabled the proposed model to reasonably predict the measured forces acting on the rear subsoiler.

   Subsoiler operations are practiced by farmers with the soil water content at or marginally below field capacity. The variables of the proposed model consist of soil properties, operating width and depth, subsoiler spacing and travel speed of the subsoilers. Since all these variables can be determined for various field situations, the proposed model will probably be applicable to different soil conditions and soil types prone to compaction, with soil water content at or marginally below field capacity.

5. The spacing between the subsoilers and the working depth of the front subsoiler influenced the performance of both models. When the front subsoiler was shallow working and close to the rear subsoiler, the proposed model under predicted the recorded forces at the rear subsoiler. At the same time the Swick-Perumpral-model over predicted forces recorded at the front subsoiler. This was probably caused by the fact that, at this spacing the RSS did most of the tilling.

At wider spacing, when each subsoiler was operating independent of each other, the measured and predicted data correlated reasonably well for both the front and rear subsoilers.

6. As originally hypothesized, there is an optimum depth for the front subsoiler and longitudinal spacing at which energy is optimized. The subsoilers were most efficient at such a spacing that allowed the soil failed by the front subsoiler to stabilize before the rear subsoiler reached it. The optimum depth of the front subsoiler, at which energy utilization was optimized, was about 80% of the operating depth of the rear subsoiler.

7.3 Recommendations.

1. The developed two-dimensional transducer system can be used for further studies involving the measurement of soil reacting forces acting on soil engaging tillage tools for other soil types and conditions, and depths of the rear subsoiler.

2. The soil-failure profile should be further studied to develop a better understanding, especially the soil-failure below the operating depth and wider than the tillage tool. The proposed straight-line failed profile along the centre-line is probably not correct and certainly not for the three-dimensional failed side crescent.

3. Data logging, when using an automatic-penetrometer with a computer program to measure and map a three-dimensional failed-profile, is at present too time consuming. This can be partly solved by improving its safety mechanism to allow for full automation of the prodding process. This will enable it to be used to study the failed profile along the centre-line and the three-dimensional coordinates of the failed profiles, especially in the sandy soils prone to compaction.

4. In the development of the proposed mathematical model, the centre-line failure angles at the front and rear subsoiler were assumed to be equal. The performance of the proposed model will improve when it accounts for a possible difference between the two failure angles.

5. The followed procedure to develop the proposed model, requires a preliminary assumption of the soil-failure pattern to determine β by minimizing the force-expressions. This is the major limitation of this procedure because the proposed model is greatly influenced by the assumed soil-failure pattern. With the recent improvement of the possibilities for using numerical methods in soil-failure studies, it is recommended that a similar model be developed employing finite elements methods. However, the use of finite element methods will require an acceptable constitutive relationship for unsaturated soils, which at present still seem to be a problem.

6. The successful use of the proposed model requires that the rake angles and the share widths of both subsoilers are equal. In practice, some farmers use subsoilers with shares of different operating widths for the front and rear subsoiler, therefore a soil force model catering for this scenario is required. Further more, the proposed model needs to be verified in sandy soils since they are more prone to compaction.

7. The reported relative position of the FSS, at which energy utilization is optimized, is valid for soils with characteristics similar to those under which this study was conducted and when the RSS is operating at a depth of 600 mm. This relationship is expected to remain valid, even at other operating depths of the RSS. However, it is recommended to validate this position in different soil types and at varying operating depths of the RSS.

8. The extended octagonal ring transducer was damaged before adequate data was collected to make reliable conclusions and the tests had to be repeated with the new measuring system. However, based on its calibration results and initial data

collected, it was clear that it would have accurately measured the forces applied to the front subsoiler. It was not used long enough to judge its durability. Its use in a similar study is recommended but effective precautions will have to be taken against overloading.

9. There is still need for a study of the side failure crescent to express its maximum width as a function of the operating depth, soil water content and rake angle, α. This will lead to a better prediction of β and the rupture radius.